

**Performance Characterisation**  
**of a**  
**Separated Heat-Pipe Heat-Recovery Heat-Exchanger**  
**for the food drying industry**

by  
Nathan Shane Thomas

*Thesis presented in partial fulfilment of the requirements for the degree  
of Master of Engineering (Mechanical) in the Faculty of Engineering at  
Stellenbosch University*



Supervisor: Mr Robert Thomas Dobson

March 2016

## DECLARATION

By submitting this thesis electronically, I declare that the entirety of the work contained therein is my own, original work, that I am sole author thereof (save to the extent explicitly otherwise stated), that reproduction and publication thereof by Stellenbosch University will not infringe any third party rights and that I have not previously in its entirety or in part submitted it for obtaining any qualification

Date: .....

## ABSTRACT

In light of the ever increasing demand for energy efficiency, waste heat recovery has become an important engineering design consideration. Heat-pipe-Heat-Exchangers (HPHE's) are waste-heat-recovery-units (WHRU's) that utilise heat pipes/thermosyphons that contain a working fluid as the heat transfer mechanism from the high temperature waste stream to the low temperature stream. To prevent cross contamination for the food industry, the exhaust and inlet streams are often far apart. However, performance correlations for separated-HPHE's are difficult to find.

For this reason, the thermal performance of an air-to-air separated-HPHE is investigated and characterised. The investigation involved the theoretical and numerical modelling of the separated-HPHE. The models were then compared to the experimental results for validation purposes. It is also important to use energy efficiently, hence the effect of air temperature and flow rate on the drying times of various materials were also investigated.

To develop the HPHE model, outside and inside heat transfer coefficients for the HPHE are required. The outside heat transfer coefficients were obtained by passing hot air over a HPHE filled with cold water and of similar geometry to the HPHE's used for the separated-HPHE. The inside heat transfer coefficients for the separated-HPHE were determined with R600a, R134a and R123 as working fluids. The experiments were undertaken at various temperatures and flow rates. The results showed that R600a works the most effectively in the temperature range considered and this is expected since R600a is less dense and has a higher latent heat of vaporisation than both R134a and R123. As an example, the R600a charged separated-HPHE yielded heat transfer rates in the region of 9352 W compared to the 7017 W and 4555 W yielded for R134a and R123 respectively at an air temperature difference of 27 °C and mass flow rate of 0.841 kg/s.

The predicted inside heat transfer coefficients correlate the experimentally obtained heat transfer coefficients reasonably well. However, it is found that theoretical models correlated by previous researchers do not correspond to the predicted values obtained from the correlations found from the testing of the separated-HPHE. The differences are attributed to the poor manifold design and the fact that the researchers conducted their experiments on a single thermosyphon, whereas the entire heat exchanger was used in this case.

The main objective of the thesis was because the as-tested separated-HPHE was shown to worked effectively (recovering up to 90 % of the of the dryer exhaust heat) for typical food industry drying temperatures of between 25-80 °C. Additionally, the theoretical simulation models for the HPHE was validated in as much that its energy saving performance was within  $\pm 12$  % of the as-tested experimental models; and thus it was demonstrated that substantial energy cost saving could be realised using standard heat exchanger manufacturing technology. If the heat exchanger is installed

in a plant, charged with R600a and is operated with an inlet air temperature of approximately 80 °C and mass flow rate of 0.841 kg/s, the heat recovered is 13.828 kW in an environment of 13 °C. At these conditions, the potential payback period of installing the heat exchanger specified for this study is 3.22 years.

It is recommended that notwithstanding accuracies of roughly 22 % obtained by the theoretically predicted correlations to the experimental work, the heat exchanger design should be optimised to allow better refrigerant flow and various performance parameters like liquid fill charge ratio and condenser/evaporator length dependencies should be further investigated.

## OPSOMMING

As gevolg van die stigende noodsaaklikheid van effektiewe energy gebruik raak energie behoud en herwin al hoe meer belangriker ingenieurs ontwerp oorwegings. Hittepyp-hitteruilers (HPHR's) is afval-hitte-herwinnings-eenheid (AHHE) wat hittepype vol koelmiddel bevat wat die hitteoordrag meganisme is vanaf die hoë temperatuur vloeistroom na die lae temperatuur vloeistroom. Om kruiskontaminasie te verhoed in die voedsel bedryf, is dit noodsaaklik dat die uitlaat en inlaat strome geskei is. Daar bestaan tans nie veel korrelasies vir geskeide-HPHR's

Vir hierdie rede word die termiese verrigting van 'n geskeide-hittepyp-hitteruiler (HPHR) ondersoek. Die ondersoek bevat die teoretiese en numeriese modellering van die geskeide-HPHR. Die modelle word vergelyk met die eksperimentele resultate om hulle te valideer. Dit is ook noodsaaklik dat energy sparsamig gebruik word en vir hierdie rede word die effek van lug temperatuur en vloeitempo op die droogmaak tye van verskeie materiale ondersoek.

Om die HPHR model te ontwikkel is dit nodig om die buite- en binne hitte oordragskoeffisiënte te vind. Die buite hitteoordragskoeffisiënte was bepaal deur warmte lug oor 'n HPHR te laat vloei wat geometries die selfde is as die HPHR's wat gebruik word vir die geskeide-HPHR. Die binne-hitteoordragskoeffisiënte was bepaal met R600a, R134a en R123 as koelmiddels. Die eksperimente was gedoen by verskeie temperature en lugvloeitempoes. Die resultate wys dat R600a die mees effektief werk by die temperature waarteen die eksperimente gedoen was. Dit was verwag as gevolg van die feit dat R600a 'n ligter gas en hoër latente-hitte-tydens-verdampings eienskap het as albei R134a en R123. As voorbeeld, die geskeide-HPHR vol R600a het 9352 W herwin in vergelyking met 7017 W en 4555 W vir die R134a en R123 respektief teen 'n lug temperatuur verskil van 27 °C en 'n lugvloeitempo van 0.841 kg/s.

Die voorspelde binne-hitteoordragskoeffisiënte korreleer die eksperimentele waardes redelik goed. Dit was egter gevind dat die teoretiese modelle wat gekorreleer was deur vorige navorsers nie goed ooreenstem met die voorspelde waardes vir die geskeide-HPHR nie. Die verskille word toegeskryf aan die swak spuitstuk ontwerp en die feit dat die navorsers hul eksperimente op 'n enkele hittepyp gedoen het, terwyl die hele HPHR gebruik was in hierdie geval.

Die hoof objektief van die tesis was beruik deur dat die geskeide-HPHR wel effektief (so hoog soos 90 % van die uitlaat hitte) gewerk het tussen die temperatuur limiete van 25-80 °C wat tipies in die voedsel bedryf gevind word. Dus was dit bewys dat daar groot energiebesparings verkry kan word deur die installasie van die HPHR.

Daarbenewens, die teoretiese modelle van die HPHHR het die eksperimentele waardes tot binne 12 % voorspel. As die geskeide-HPHR op 'n fabriek geïnstaleer word met inlaat lugvloei kondisies van

80 °C en 0.841 kg/s kan 13.828 kW herwin word as die omgewingstemperatuur 13 °C is. Vir hierdie toestande is die potensiaale terugverdiens tyd 3.22 jare.

Dit word beveel dat die HPHR se ontwerp geoptimeer moet word vir minder vloeistof weerstand en dat die vloeivulverhouding en die verdamer-tot-kondensator-lengteverhouding verdere ondersoek vereis, aangesien die 22 % akkuraatheid tussen die teoretiese en praktiese metings te hoog is.

## **ACKNOWLEDGEMENTS**

I would firstly like to thank the Heavenly Father for the opportunity and grace to pursue this thesis.

Secondly, I thank my supervisor Mr RT Dobson for his patience and faith, even when things seemed hopeless. The workshop personnel, especially Mr C Zietsman, J Stanfliet and C Haremse are thanked for their contributions to the experimental work. Mr B de Kooker is also thanked for his insights regarding the charging of the experiment. Thanks is also extended to Mr G Davids of ColCab for helping with the heat exchanger manufacturing.

Lastly, to all my family and close friends. The motivation, support and guidance has changed my being forever. Thanks guys!

**CONTENTS**

DECLARATION .....	i
ABSTRACT .....	ii
OPSOMMING .....	iv
ACKNOWLEDGEMENTS .....	vi
LIST OF FIGURES .....	ix
LIST OF TABLES .....	xii
NOMENCLATURE.....	xiii
1 INTRODUCTION .....	1
2 LITERATURE STUDY .....	3
2.1 Historical Development of Heat Pipes .....	3
2.2 Thermosyphons .....	4
2.2.1 Thermosyphon characteristics .....	7
2.2.2 Performance parameters of thermosyphons .....	8
2.3 Heat Pipe Heat Exchangers .....	10
2.4 Enthalpy Wheels and Plate Heat Exchangers .....	12
2.5 Air Driers.....	15
3 THEORY .....	17
3.1 Single Thermosyphon Model .....	17
3.1.1 Evaporator internal heat transfer resistance .....	18
3.1.2 Condenser internal heat transfer resistance .....	21
3.1.3 Thermal resistance across the thermosyphons walls .....	23
3.1.4 Outside heat transfer resistance .....	23
3.2 Heat Exchanger Model .....	24
3.2.1 Un-finned individual tubes.....	24
3.2.2 Plate-and-Tube configuration.....	25
3.2.3 Plain individually finned tubes.....	27
3.4 Drying Theory .....	28
3.4.1 Heat transfer mechanism .....	28
3.4.2 Mass transfer mechanism .....	29
3.4.3 Air drying process .....	31
3.4.4 Constant-rate drying period time prediction .....	34
3.4.5 Falling-rate drying period time prediction .....	36
4 ALGORITHM.....	38
5 EXPERIMENTAL WORK.....	41
5.1 Manufacture of Heat Exchanger.....	41



5.2 Experiments.....	41
5.2.1 Equipment and instrumentation used .....	41
5.2.2 Calibration techniques.....	42
5.2.3 Experimental setups .....	43
5.2.4 Experimental procedures.....	48
6 RESULTS .....	50
6.1 Thermal Performance of the Separated-HPHRHE.....	50
6.1.1 Outside heat transfer coefficients and pressure loss.....	50
6.1.2 Inside heat transfer coefficients: R600a .....	53
6.1.3 Inside heat transfer coefficients: R134a .....	58
6.1.4 Inside heat transfer coefficients: R123 .....	63
6.1.5 Inside temperature distribution and comparison with numerical predictions....	67
7 DISCUSSION AND CONCLUSIONS .....	74
8 RECOMMENDATIONS FOR FUTURE WORK .....	78
REFERENCES.....	79
Appendix A: Sample Calculations .....	83
A1 Heater power input .....	83
A.2 Drying time estimation.....	86
A.3 Calculation of outside heat transfer coefficients .....	88
A.4 Calculation of inside heat transfer coefficients .....	90
Appendix B: Material Properties.....	93
Appendix C: Drier System Characteristics and Heat exchanger experimental setup.....	95
Appendix D: HPHE manufacturing details .....	99
Appendix E: Installation Cost analysis.....	102
Appendix F: Drying Test results .....	103

**LIST OF FIGURES**

<b>Figure 1</b> Perkins boiler (taken from Lock 1992) .....	3
<b>Figure 2</b> Heat pipe and single - and two phase thermosyphon operation .....	5
<b>Figure 3</b> Separated thermosyphon loop arrangement .....	6
<b>Figure 4</b> “Wrap around” dehumidifier thermosyphon schematic .....	6
<b>Figure 5</b> An industrial HPHE (Taken from <i>china-heatpipe.net</i> ) .....	11
<b>Figure 6</b> Enthalpy wheel operation.....	13
<b>Figure 7</b> Exploded view of a plate heat exchanger (obtained from <i>http://targetequipments.com/plate_heat_exchanger_manufacturers.html</i> ).....	14
<b>Figure 8</b> A typical Air drier unit .....	15
<b>Figure 9</b> Thermal resistance model of a single thermosyphon .....	17
<b>Figure 10</b> Un-finned tube bundle configurations, a) aligned, b) staggered .....	24
<b>Figure 11</b> Plate-finned tube bundle configuration .....	26
<b>Figure 12</b> Plate-and-tube control volume, a) plan view b) cut-away view .....	26
<b>Figure 13</b> Individually finned tube a) configuration and b) control volume .....	27
<b>Figure 14</b> Mass sample .....	29
<b>Figure 15</b> Concentration Mass sample .....	30
<b>Figure 16</b> Moisture content of sample .....	31
<b>Figure 17</b> Moisture content of sample relative to position .....	33
<b>Figure 18</b> Typical drying rate curve .....	35
<b>Figure 19</b> Numerical algorithm control volume .....	38
<b>Figure 20</b> Separated-HPHRHE schematic.....	39
<b>Figure 21</b> Computer algorithm flow diagram.....	40
<b>Figure 22</b> Load cell calibration.....	43
<b>Figure 23</b> Thermocouple calibration .....	43
<b>Figure 24</b> Drying test setup .....	44
<b>Figure 25</b> Cooling and heating water tank systems .....	45
<b>Figure 26</b> Experimental setup for determining the outside heat transfer coefficient.....	46
<b>Figure 27</b> Experimental setup for determining the inside heat transfer coefficient.....	47
<b>Figure 28</b> Thermosyphon loop charging setup .....	48
<b>Figure 29</b> Energy balance of the geometrically similar heat exchanger.....	51
<b>Figure 30</b> Outside heat transfer coefficients for each row of the geometrically similar heat exchanger filled with cold water .....	52
<b>Figure 31</b> Pressure loss across the HPHE.....	53
<b>Figure 32</b> Energy balance of the separated-HPHE operating with R600a.....	54

<b>Figure 33</b> The thermal resistance of the separated-HPHE charged with R600a at different mass flow rates .....	54
<b>Figure 34</b> Inside heat transfer coefficients for the separated-HPHE operating with R600a and charged to 50 % of the evaporator length for Row 1-3 .....	56
<b>Figure 35</b> Inside heat transfer coefficients for the separated-HPHE operating with R600a and charged to 50 % of the evaporator length for Row 4-6 .....	57
<b>Figure 36</b> Energy balance of the separated-HPHE operating with R134a.....	58
<b>Figure 37</b> The effectiveness of the separated-HPHE charged with R134a at different mass flow rates	59
<b>Figure 38</b> Inside heat transfer coefficients for the separated-HPHE operating with R134a and charged to 50 % of the evaporator length for Row 1-3 .....	61
<b>Figure 39</b> Inside heat transfer coefficients for the separated-HPHE operating with R134a and charged to 50 % of the evaporator length for Row 4-6 .....	62
<b>Figure 40</b> Energy balance of the separated-HPHE operating with R123 .....	63
<b>Figure 41</b> The effectiveness of the separated-HPHE charged with R123 at different mass flow rates	64
<b>Figure 42</b> Inside heat transfer coefficients for the separated-HPHE operating with R123 and charged to 50 % of the evaporator length for Row 1-3 .....	66
<b>Figure 43</b> Inside heat transfer coefficients for the separated-HPHE operating with R123 and charged to 50 % of the evaporator length for Row 4-6 .....	67
<b>Figure 44</b> Inside temperature distribution of the separated-HPHE charged with R600a for the various rows at different mass flow rates .....	68
<b>Figure 45</b> Inside temperature distribution of the separated-HPHE charged with R134a for the various rows at different mass flow rates .....	69
<b>Figure 46</b> Inside temperature distribution of the separated-HPHE charged with R123 for the various rows at different mass flow rates .....	69
<b>Figure 47</b> Comparison between the evaporator and condenser heat transfer rates and the mathematical model of the separated-HPHE charged with R134a at an air mass flow rate of 0.841 kg/s.....	70
<b>Figure 48</b> Comparison between the evaporator and condenser heat transfer rates and the mathematical model of the separated-HPHE charged with R123 at an air mass flow rate of 0.841 kg/s.....	70
<b>Figure 49</b> Comparison between the evaporator and condenser heat transfer rates and the mathematical model of the separated-HPHE charged with R600a at an air mass flow rate of 0.841 kg/s.....	71
<b>Figure 50</b> Comparison between the theoretically determined inside evaporator coefficients for R123	72
<b>Figure 51</b> Comparison of the theoretically determined inside condenser coefficients for R123	72
<b>Figure 52</b> Comparison between the theoretically determined inside evaporator coefficients for R134a	72
<b>Figure 53</b> Comparison of the theoretically determined inside condenser coefficients for R134a	73
<b>Figure 54</b> Comparison between the theoretically determined inside evaporator coefficients for R600a	73
<b>Figure 55</b> Comparison of the theoretically determined inside condenser coefficients for R600a	73
<b>Figure 56</b> Current drier design.....	83

<b>Figure 57</b> Proposed drier design .....	85
<b>Figure 58</b> a) Sample of product, b) Process variables .....	87
<b>Figure 59</b> Air flow and Various positions of ducts and bends in the test drier.....	95
<b>Figure 60</b> Duct dimensions (as positioned in figure 60).....	96
<b>Figure 61</b> Bend dimensions .....	96
<b>Figure 62</b> Drier system characteristic curve .....	97
<b>Figure 63</b> Schematic of the wind tunnel setup for the determination of the outside heat transfer coefficients .....	98
<b>Figure 64</b> Schematic of the wind tunnel setup for the determination of inside heat transfer coefficients	99
<b>Figure 65</b> Evaporator coil and flange design .....	100
<b>Figure 66</b> Evaporator coil manifold positions and dimensions .....	101
<b>Figure 67</b> Porous material (sponge) drying test results .....	103
<b>Figure 68</b> Cellular material (potatoes) drying test results.....	104
<b>Figure 69</b> Granular material (rusks) drying test results .....	104

**LIST OF TABLES**

<b>Table 1</b> HPHE configuration (adapted from Zhang & Zhaung, 2003) .....	12
<b>Table 2</b> Dimensionless moisture ratio as per equation 3.106 (Dobson, 2001).....	34
<b>Table 3</b> Heat exchanger specifications .....	39
<b>Table 4</b> Program predictions .....	40
<b>Table 5</b> Drier parameters .....	83
<b>Table 6</b> Values of variables in Figure 65 .....	87
<b>Table 7</b> Data for calculation of outside heat transfer coefficients.....	88
<b>Table 8</b> Data values for the calculation of the inside heat transfer coefficient .....	90
<b>Table 9</b> HPHE savings potential .....	102

**NOMENCLATURE**

$A$	area, m <sup>2</sup>
$altit$	altitude, m
$C$	concentration, kg-vapour/kg-dry air
$C'$	loss coefficient
$C_n$	nozzle discharge coefficient
$c_p$	specific heat, J/kgK
$D$	mass diffusivity, m <sup>2</sup> /s
$d$	diameter, m
$d_c$	characteristic length, m
$d_h$	hydraulic diameter, m
$e$	fin height, m : error
$f$	friction factor
$G$	mass velocity, kg/m <sup>2</sup> s
$h$	heat transfer coefficient, W/m <sup>2</sup> K : enthalpy, kJ/kg
$h_{fg}$	enthalpy of vaporisation for water, kJ/kg
$j$	Colburn j-factor
$K_{Re}$	Reynolds number correction factor
$k$	diffusion coefficient, m <sup>2</sup> /s : thermal conductivity, W/Mk
$L$	length, m
$L_c$	characteristic length, m
$m$	mass, kg
$\dot{m}$	mass flowrate, kg/s
$N_p$	number of tubes per row
$N_r$	number of tube rows
$Nu$	Nusselt number, $hL_c/k$
$P$	Absolute pressure, Pa
$Pr$	Prandtl number, $c_p\mu/\rho$
$p$	dimensionless pitch : perimeter, m
$\dot{Q}$	heat transfer rate; heating element power input, W
$R$	thermal resistance, K/W
$Re_d$	Reynolds number, $\rho V d_h/\mu$
$RH$	relative humidity, kg-H <sub>2</sub> O/kg-dry air
$r$	coefficient of determination
$S$	pitch, m

$St$	Stanton number, $h/\rho c_p V$
$s$	spacing, m
$T$	temperature, °C
$t$	thickness, m: time, s
$V$	velocity, m/s ; volumetric flow rate, m <sup>3</sup> /s ; volt
$W_{fan}$	fan work, W
$X$	moisture content, kg-water/kg-solids

#### Greek symbols

$\varepsilon$	roughness, m
$\rho$	density, kg/m <sup>3</sup>
$\Phi$	relative humidity, %
$\omega$	specific humidity, kg-water/kg dry air
$\mu$	dynamic viscosity, kg/ms
$\theta$	moisture ratio
$\infty$	surroundings/ambient

#### Subscripts

$alum$	aluminium
$c$	cold, condenser, characteristic
$cface$	condenser face
$cond$	condenser
$cop$	copper
$cr$	critical
$cv$	control volume
$db$	dry bulb
$duct$	air duct
$e$	evaporator, equilibrium
$eface$	evaporator face
$evap$	evaporator, evaporate
$exp$	experimental
$f$	fin, frontal, fluid
$g$	gas
$h$	hot
$hp$	heat pipe

<i>i</i>	inside, inlet
<i>L</i>	longitudinal
<i>m</i>	mass
<i>n</i>	nozzle
<i>o</i>	outside, outlet
<i>pred</i>	predicted
<i>s</i>	saturated, free surface, solids
<i>ss</i>	stainless steel
<i>T</i>	transverse
<i>v</i>	vapour
<i>w</i>	water, wall
<i>wb</i>	wetbulb

#### Abbreviations

DAS	data acquisition system
FS	full scale
HPHE	heat pipe heat exchanger
HPHRHE	heat pipe heat recovery heat exchanger
ID	internal diameter
OD	outside diameter
TCU	temperature control unit
VSC	variable speed control
VSD	variable speed drive
WHRU	waste heat recovery unit



## 1 INTRODUCTION

As our limited non-renewable energy resources diminish and become more costly, energy conservation and waste heat utilisation become increasingly important engineering design considerations. Heating and cooling of process streams are usually the most energy intensive processes on a process plant. Many industries, like the nuclear and food processing industries, rely heavily on process heat for their operation. Once this process heat is used it is expelled from the system as waste heat. The waste air stream is usually not suitable to use in the process again (consider automobile exhaust gas as an example), but is high in heat energy which can be utilised to preheat a subsystem in the process.

WHRU's use this waste heat energy to improve the efficiency of a process. According to Pieters (2006), a WHRU has to satisfy four key criteria: firstly, it has to effectively transfer heat from one process stream to another. Secondly it must cause a low pressure drop when installed. It should also be corrosion and fouling resistant and finally its heat transfer surfaces must be relatively far apart (in case of damage/leakage that could cause cross contamination). HPHE's are one specific type of WHRU which use heat-pipes to transfer heat from the hot exhaust stream to the cold inlet stream. Heat pipes are essentially "natural heat pumps", which exchange heat between the hot and cold fluid streams by utilising the large latent heat of vaporisation of a refrigerant. Heat pipes have the distinct advantage over other WHRU's of being able to transport large amounts of heat energy across a long distance very effectively. This is especially advantageous in applications where the exhaust and inlet streams are separated, like food drying applications. A conventional HPHE has the evaporator and condenser sections adjacent to each other, but for certain applications, like food drying, contamination is undesired and the heat exchanger has to be separated. However, thermal performance correlations for separated-HPHE's are not easily found in literature. Thus, the main objective of this thesis is to evaluate the performance of a separated-HPHRHE using readily obtainable refrigerants.

Successful integration of a separated-HPHRHE into a system requires that the thermal performance characteristics of said heat exchanger is known. This is done experimentally and compared to a numerical algorithm, the results are then given in such a way that a thermal engineer wanting to incorporate a separated-HPHRHE into a process plant can easily use the correlations to select the correct sized heat exchanger.

Before recovering energy successfully, efficient energy use is a key parameter. In the food processing industry for example, biscuit manufacturers have wide estimating ranges for the drying time of their products. Drying characteristics of cellular food products (like potatoes and apples) have been investigated by other researchers, however the drying characteristics of granular food products (like rusks) are less well known. For this reason the drying characteristics of various food products are

experimentally investigated. This is however not a direct objective of the study and will be considered in Appendix F.

The objectives of this thesis can thus be summarised as follows:

- Experimentally characterise and compare the thermal performance of a separated heat pipe heat recovery heat exchanger (HPHRHE) using different refrigerants
- Write a computer program that can be used to simulate the separated-HPHRHE

The document gives a historical background and literature survey on thermosyphons, HPHEs and air driers in Section 2. This is followed by all the necessary mathematical formulations required to model a separated-HPHRHE in Section 3. Section 4 describes the algorithm for the heat exchanger. The experimental work undertaken is documented in Section 5. Section 6 documents the thermal performance results of the separated-HPHRHE. Finally the thesis ends with a discussion of the results, conclusions and recommendations for future work in Section 7 and 8. The Appendices document the calculations, drying results and the manufacturing details.

## 2 LITERATURE STUDY

Heat pipes are devices that transfer heat using the large latent heat of a working fluid. The device is used in a variety of applications from air-conditioning to electricity generation. The historical development, performance characteristics, advantages and disadvantages of using heat pipes will be discussed in this literature study, including its advantages and disadvantages and alternative heat recovery devices.

### 2.1 Historical Development of Heat Pipes

The Perkins boiler, a device that uses single or two phase processes to transfer heat, was developed by A. M. Perkins and J. Perkins in the 1800's. The device consists of a tube and an airtight space filled partially filled with working fluid. Boiling, condensation, convection heat - and mass transfer occur between the boiling and condensation sections. One end of the tube projects into a furnace which is situated at the bottom of the device, while the other end of the tube projects upward into the water of the boiler. Heat supplied by the furnace rises up the tube into the boiler section, where the heat is given to the surrounding water (Pioro, 1997). The Perkins boiler represented a technological step forward in a time when high pressure boilers were still in their experimental phase. Additionally, the Perkins tube had no fouling, scaling and leakage problems like the high pressure boilers of the time. A Perkins boiler is illustrated in Figure 1.

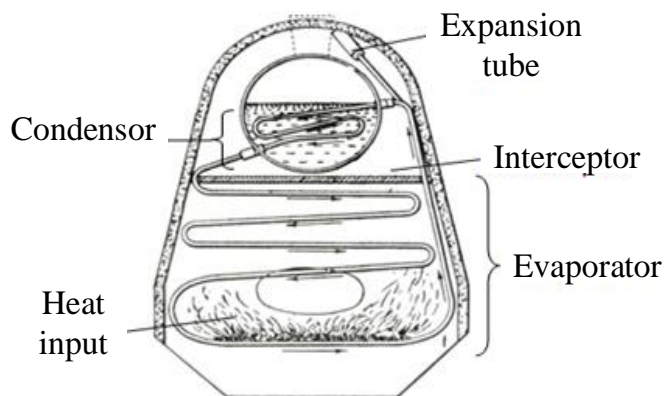


**Figure 1** Perkins boiler (taken from Lock 1992)

The Perkins boiler design neglected the use of external fins to increase the tube-to-gas heat transfer. Gay proposed this concept in 1929. He vertically aligned a number of finned Perkins tubes with the evaporator section below the condenser section (Dunn, 1994). The respective evaporator and condenser sections were then separated by a plate. Along with the introduction of capillary forces by incorporating wicking structures in the heat pipe, this is considered the birthplace of the modern heat pipe.

A modern heat pipe consists of a sealed pipe lined with an internal wicking structure and a hollow inner section, which contains a small amount of working fluid. A heat pipe consists of two sections, the evaporator and condenser. Heat supplied to the evaporator section by a hot waste fluid stream heats the working fluid till it vaporises. The pressure difference between the two sections causes the vapour to flow to the condenser section, where it gives off its latent heat of vaporisation and condenses. The capillary forces in the wicking structure “pump” the fluid back to the evaporator section and the process repeats itself. The heat pipe is very efficient due to the minimal temperature drop between the evaporator and condenser.

In 1944, R.S. Gaugler proposed using the heat pipe in refrigeration engineering applications, due to the large heat transfer rates attainable. This idea never was applied commercially due to the fact that energy was relatively cheap, thus heat recovery was not an essential part of thermal system designs. However in 1962, the heat pipe idea was suggested by Trefethen in high temperature space power systems (Ivanoskii, 1982). Grover then started developing the heat pipe in 1963 at Los Alamos National Laboratory in New Mexico. He illustrated the effectiveness of heat pipes as a high performance heat transfer device. Grover’s work, along with the theoretical results and design guidelines published by Cotter in 1965 are recognised by many as the true beginning of heat pipe research. Following these developments, in 1968 Nozu bundled together a number of finned heat pipes in an air heater. This was ultimately known as the heat pipe heat exchanger (HPHE). This could then be used in various energy recovery applications from refrigeration to air-conditioning.

## **2.2 Thermosyphons**

Thermosyphons are heat transfer devices without a wicking structure and are considered a special type of heat pipe. The fundamental difference between heat pipes and thermosyphons is that thermosyphons utilise gravity to allow condensate flow back to the evaporator, instead of the capillary forces in the wicking structure of a “normal” heat pipe. Similar to heat pipes, the working fluid is vaporised by heat addition in the evaporator section and the vapour moves into the condenser section due to the pressure difference between the two sections. The working fluid then gives off its latent heat of vaporisation to the cooler condenser section and as such condenses. The condensate runs down the tube wall under the influence of gravity and the process is repeated. Thermosyphons are preferred due to lower condensate flow resistances. The wicking structure in the heat pipe causes a condensate flow resistance which decreases the attainable heat flux in the heat pipe by 1.2 to 1.5 times below that of a thermosyphons (Pioro, 1997). Furthermore, “normal” heat pipes are more expensive to manufacture than thermosyphons because they are structurally more complicated.

Thermosyphons can be categorised as single phase and two phase flow devices. In a single phase thermosyphon, the pipe is filled with only liquid or gas while the operation is taking place instead of

the two-phase flow taking place in a two-phase device. The major disadvantage of a single phase liquid thermosyphon is the fact that one has to make provision for the fact that liquid expands as it is heated. This could cause difficulty in controlling the internal pressure of the tube. Additionally, in a two phase flow thermosyphon, the heat transfer capacity is increased because one can utilise the large latent heat transfer mechanism of the working fluid. Figure 2 illustrates the difference between a heat pipe, a single phase and two phase thermosyphon.

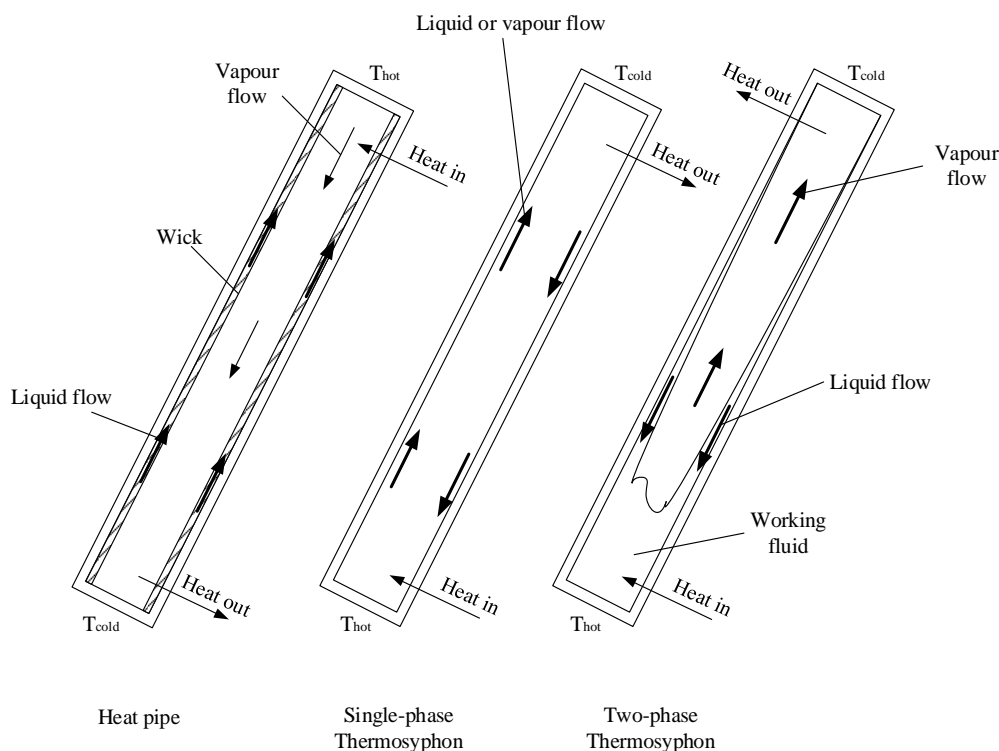


**Figure 2** Heat pipe and single - and two phase thermosyphon operation

Thermosyphons can also be categorised as opened or closed. An open thermosyphon has no condenser section and the working fluid is continuously supplied by an external source. The fluid evaporates to the environment when it is vaporised. These thermosyphons are used primarily to study boiling processes inside thermosyphons (Piro, 1997). Aerosyphons are a type of thermosyphon in which the heat flux is transferred by the forced convection of the liquid. In an aerosyphon, saturated gas is passed through the working fluid causing bubbles to be propagated in the fluid, which in essence “stirs” the liquid. However, the aerosyphon has no commercial applications and is mainly used to investigate boiling heat transfer.

Thermosyphons can also be used like conventional refrigeration systems due to the fact that the evaporator and condenser sections can be separated in what is termed a “separated loop” arrangement (Yun & Krolczek, 2002). Dobson & Jeggels (2008) successfully illustrated this in the cooling of an electronic cabinet. They found that an energy recovery of up to 500 W is possible using a single 12.7 mm OD separated thermosyphon. This arrangement is illustrated in Figure 3. The principle of

operation remains the same: the working fluid is vaporised in the evaporator section and runs in the vapour line to the condenser, where heat is removed and condensation occurs. Any vapour still present after the condenser is condensed in the liquid line. Here it is imperative that the separated condenser section be located at a relative position which is above the evaporator section. Consequently, the liquid line must have a net downward gradient toward the evaporator. To minimise flow losses, smooth walls must be employed in the riser and downcomer lines.

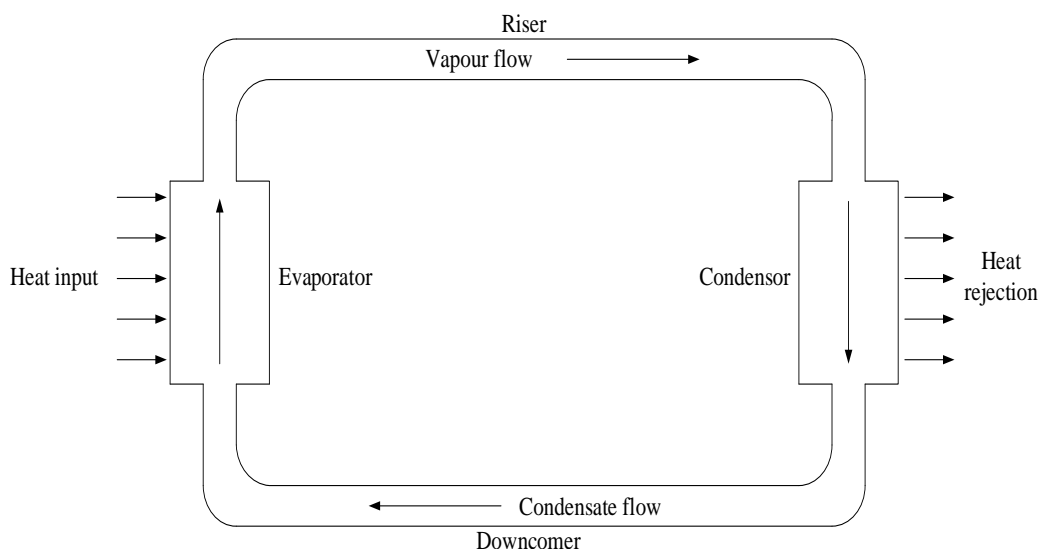


**Figure 3** Separated thermosyphon loop arrangement

An example of a practical application of separated thermosyphons are in air-conditioning applications. Wu *et al* (1997) used a separated-HPHE to control humidity in their experimental work. It is often desired to remove moisture from the incoming air. However, dehumidification and cooling are inseparable, and the air must often be reheated at high costs. In this case the condenser and evaporator sections can be separated and placed on either side of a dehumidifier as depicted in Figure 4.

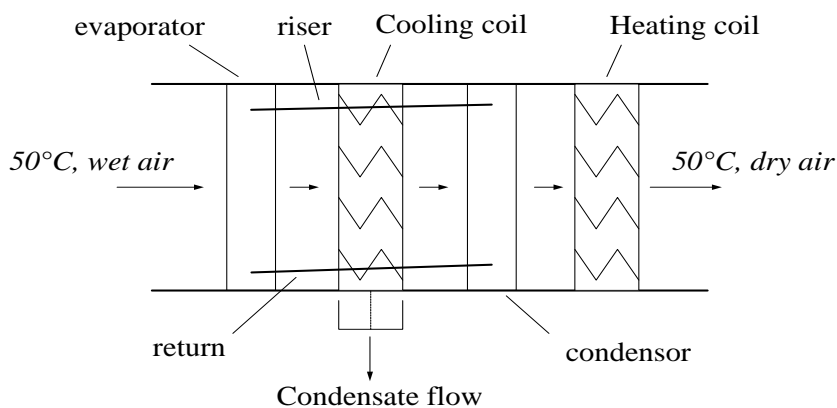


**Figure 4** “Wrap around” dehumidifier thermosyphon schematic

### 2.2.1 Thermosyphon characteristics

Thermosyphons have many favourable characteristics that make them very viable heat recovery devices. Firstly, thermosyphons can act as thermal transformers. Energy can be added at a low heat flux over a large area and removed at a high heat flux over a small area (Faghri, 1995). Thermal transformer ratios as high as 15:1 can be attained. Thus, the thermosyphons can be designed to maintain a constant temperature at the condenser section, even though the rate of the heat input to the evaporator may vary. Secondly, a thermosyphon requires very little maintenance and is a self-contained, closed system that in most cases is easy to install. Finally, thermosyphons also have a very high thermal conductance, up to a 1000 times higher than an equivalent copper pipe in similar conditions (Russwurn, Part 1, 1980).

Thermosyphon performance characteristics are often dependant on the air-to-wall heat transfer characteristics, the wall conductance of the tube walls and the internal heat transfer coefficients of the condenser and evaporator. The latter characteristics are very important and complex to calculate, and these will be discussed in turn.

#### *Inside condenser heat transfer coefficient*

The vapour that condenses in the condenser section can condense in two ways, either filmwise condensation – which forms a continuous liquid film and runs down the tube wall – or dropwise condensation, which forms droplets that run down the tube wall. Dropwise condensation is highly unlikely and thus filmwise condensation is usually modelled in the condenser section. Whalley (1987), states that Nusselt theory can be used to find the heat transfer coefficient.

#### *Inside evaporator heat transfer coefficient*

The falling film of working fluid propagated in the condenser section continues into the evaporator section. The sub-cooled fluid film is heated as it flows down the evaporator section. If the saturation temperature is reached before it reaches the liquid pool, some of the liquid from the film will evaporate. In total, three boiling mechanisms may occur: nucleate, convective and film boiling. Nucleate boiling - in which vapour bubbles form from nucleation sites in the liquid pool - is generally accepted as the dominant form of boiling. However, the actual boiling process is very difficult to model and the heat transfer correlations are usually experimentally determined.

Many sources document different correlations for determining heat transfer coefficients. Correlations are found in Whalley (1987) and Pioro (1997). Care should be exercised in using them as the results are sometimes very different. Dobson & Kroger (1999) document correlations for ammonia charged thermosyphons, which give results within 10 % of the experimental results. They also evaluated existing correlations for the pool boiling heat transfer coefficients and found that these estimations were 57 % under the experimental values for ammonia.

Dobson & Pakkies (2002) investigated the heat transfer correlations for an R134a charged two-phase thermosyphon. Liquid charge fill ratios of 50 % were used and the experiments were conducted for vertical and inclined cases. They established that the maximum heat transfer rate is at an inclination angle of 45° and is approximately 40 % higher than the vertical inclination. Meyer (2003) investigated heat transfer correlations for R134a and butane. Again, liquid charge fill ratios of 50 % were used and the experimental errors of 5 – 15 % were found for both butane and R134a.

### **2.2.2 Performance parameters of thermosyphons**

Thermosyphons are subject to various limitations and factors which influence their performance; these include flooding, entrainment, dryout and boiling limitations as well as other miscellaneous factors. These factors are discussed below.

#### ***Flooding and entrainment limits***

As the vapour moves from the evaporator to the condenser and the liquid film moves in the opposite direction, viscous forces arise that decelerate the liquid film. The vapour velocity is dependent on the heat input to the evaporator, while in turn the viscous shear force on the surface of the liquid film is dependent on the vapour velocity. Thus if the heat input becomes large enough, the viscous shear forces may eventually become so large that the liquid film is entirely prevented from moving back from the condenser to the evaporator. When this occurs, the thermosyphon is said to be flooded. If additional heat is added, the vapour velocity becomes even larger and the thermal-fluid condition becomes unstable. This instability causes liquid droplets at the surface of the liquid film to be sheared from the film completely, becoming entrained in the vapour. When this occurs the entrainment limit is reached. The flooding limit can be predicted by using the Wallis (1969) and Kutateladze (1972) correlations.

The liquid fill charge ratio also plays a vital role in the flooding limit. This parameter is defined as the ratio of the volume of the liquid phase of the working fluid to the thermosyphon's volume or the evaporator volume. It is imperative to define whether the fill ratio is relative to the thermosyphon or the evaporator volume. The role the fill ratio plays on the flooding limit is summarised as follows by Lock (1992): for small charge fill ratios, the heat transfer limit increases as a power of the filling ratio. For large charge ratios, the heat transfer limit stays approximately constant. Piro (1997) suggests that the actual quantity of working fluid should be between 30-33 % of the thermosyphons volume and if the condenser length is longer than the evaporator, the fill ratio should be up to 50 % of the evaporator. The effects of charge fill ratios were investigated by Park et. al (2002). Their results showed that the effect of the fill charge ratio on the heat transfer coefficient were negligible when using a copper container and FC-72 as working fluid. The experiments were conducted in the range



of 50 – 650 W and 10 – 70 % charge fill ratios. However, the condenser heat transfer coefficients were not influenced by the fill ratio.

### ***Dry-out limitation***

The dry out limitation refers to a condition in which the bottom of the evaporator is completely dry. This usually occurs when the liquid charge fill volume is very small and the radial heat flux around the evaporator is very large. The liquid film flowing down the tube wall approaches zero thickness as it reaches the bottom of the evaporator. This causes that the entire amount of working fluid is circulated as vapour or as a falling film. If the heat flux increases, the net result is that the film length in the evaporator becomes shorter and thus approaches zero thickness higher in the evaporator, leaving the lower section of the evaporator completely dry and shortening the effective evaporator area. The evaporator wall temperature thus increases but the heat transfer stays constant.

### ***Boiling limitation***

This phenomenon occurs when the liquid charge fill ratio is high and the heat flux in the evaporator area is very large. If the heat flux increases, nucleate boiling occurs. At a critical heat flux, vapour bubbles coalesce close to the wall, preventing liquid from touching the tube wall. The tube wall temperature increases rapidly, to compensate for the loss of heat flux because the vapour has a higher thermal resistance, not allowing heat flow into the liquid. This is analogous to the effect of air between two walls in a housing structure.

### ***Miscellaneous factors***

Geometric properties play an important role in the performance of a thermosyphons. Varying the diameter can have a profound effect on liquid and vapour interactions in the condenser (Pioro, 1997). The evaporator and condenser lengths also determine the amount of heat transferred from each section, effectively increasing or decreasing the heat transfer surface area. Pioro (1997) also states that experiments have been conducted to determine if the adiabatic section between the condenser and the evaporator has an effect on heat transfer and this effect was found to be negligible in comparison to other geometric parameters. However, Abou-Ziyan et al. (2001) investigated the effect of adiabatic length on the performance of thermosyphons. The tests were conducted using water and R134a as working fluids. Their results indicated that as the adiabatic length increases, so does the heat transfer capabilities. They also found that optimum heat transfer takes place at fill charge ratios of 50 % of the evaporator volume.

The next miscellaneous consideration is the working fluid. Depending on the temperature – which determines the pressure of the vapour – one selects a working fluid. The temperature is important to ensure that the working fluid remains in a stable condition and does not break down into its separate chemical components. Low pressures naturally ensure that the thermosyphon does not leak or burst.

Pirotto (1997) states that a working fluid should have a high latent heat of vaporisation so that large amounts of heat can be transferred at low vapour flow rates. Most importantly, the critical parameters of the working fluid should be above the operating temperature. For the reasons stated above, water is the best working fluid. It transmits more heat than other working fluids, it is cheap, readily available and fire and explosion resistant. However, the high pressures encountered in operation (20 bar @ 180 °C) and difficulty of charging the HPHE without specialised machinery deems it too dangerous for the scope of this project.

Another factor to be considered is the thermosyphons inclination angle. Payakaruk *et al.* (2000), investigated the effect of inclination angles from 0 -70° with copper thermosyphons with ID's of 7.5, 11.1 and 25.3 mm and working fluids R22, R134a, R123 and water. Their results showed that the heat transfer rate is increased at inclination angles of 30 – 70° and that working fluids with high latent heats of vaporisation conduct larger amounts of heat.

### **2.3 Heat Pipe Heat Exchangers**

For any thermal process in which heat is generated, heat has to be removed. This heat that is removed often is waste heat and is usually of sufficient thermal quality to be employed into the thermal system as a preheater or heat source for another subsystem. General industry guidelines divide waste heat categories according to temperature ranges: low ( $T < 230$  °C), medium (230° - 650 °C) and high ( $T > 650$  °C). Heat exchangers transfer heat or recover heat from waste heat streams.

Heat exchangers can be split into various categories according to their flow configurations and their functions. Flow configurations include single stream, parallel-flow two stream, counterflow two stream and cross flow two stream. In single stream heat exchangers, the temperature of only one fluid changes and the direction of fluid flow is irrelevant. Examples include boilers and condensers. Parallel-flow two stream heat exchangers have the fluid streams flowing parallel to each other in the same direction (McQuay, 2001). Examples include shell and tube heat exchangers. In counterflow heat exchangers, fluids flow parallel but in opposite directions to each other, this increases the effectiveness above that of a parallel flow two stream heat exchanger. Cross flow two stream heat exchangers have the fluid streams flowing at right angles to each other.

Heat exchangers may also be classified as recuperative or regenerative. In recuperative heat exchangers the hot and cold fluid streams do not mix and heat transfer takes place from the hot stream to a barrier by convection, through the wall by conduction and from the wall to the cold fluid stream by convection. In regenerators, heat is removed from the hot fluid stream and transferred to the cold fluid stream by a temperature source.

Heat-pipe-heat-exchangers (HPHE) can be classified as liquid-coupled indirect heat transfer type heat exchangers that use thermosyphons or heat pipes as the main heat transfer mechanism (Meyer, 2003). An industrial HPHE is illustrated in Figure 5. HPHE's can be used for liquid-to-liquid, gas-to-liquid and gas-to-gas heat exchange. The evaporator section of the HPHE must be in the hot or waste fluid stream and the condenser section in the cold fluid stream. One can also enhance the rate of heat transfer by adding fins to the thermosyphons.



**Figure 5** An industrial HPHE (Taken from *china-heatpipe.net*)

HPHE's have numerous advantages over conventional heat exchangers, these can be summarised as follows (McQuay (2001)):

- Thermosyphons, and thus HPHE's, have no moving parts like gears or belts
- No auxiliary fluid power requirements for lubrication for example
- Heat transfer rate can be adjusted by inclining the HPHE.
- HPHE's are redundant in their very design, if a thermosyphon fails, the HPHE is still operational
- Cross contamination of fluids is prevented
- HPHE's can be used as thermal transformers

HPHE's are also relatively simple to incorporate into a variety of thermal systems because of their design simplicity. This is proven by the various industrial applications in which HPHE's are employed. Various researchers have also proven the viability of HPHE's as heat recovery devices. Yang et al. (2003) used a HPHE to recover heat from the exhaust gas of an automobile, using the recovered heat to warm incoming air to provide thermal comfort for the passengers and recovered up to 6.5 kW.

Zhang & Zhaung (2003) investigated the use of HPHE's as air preheaters and heat exchangers; their findings are given by way of Table 1. They used 20 different structure types of 25 – 32 mm in diameter and 1.2 – 2 m in length in over 300 different operating conditions. For a case of using the HPHE as

an air preheater, a heat recovery of close to 12000 kW was obtained. This illustrates the possible savings attainable from such a heat exchanger in larger plant applications.

Adding fins to the thermosyphons further enhances the heat transfer capabilities of the HPHE. Furthermore, thermosyphon material also has a large influence on heat transfer capabilities. Lukitobudi *et al.* (1995) studied the design and testing of a HPHE for a medium temperature application. Water as the working fluid was charged in copper pipes of OD 15.88 mm and thermosyphon, evaporator and adiabatic lengths were 300, 300 and 150 mm respectively. The results showed that effectiveness values using copper instead of steel thermosyphons were increased from 6.2 – 49 % to 17.5 – 63 %.

**Table 1** HPHE configuration (adapted from Zhang & Zhaung, 2003)

Pipe size [mm]	OD 51, t = 4.5, L = 6000, 1914 pieces	
Heat Exchanger size [m]	Height 6.4, Length 2.4, Inlet width 13.7, Outlet width 10.37	
	<i>Flue gas</i>	<i>Air</i>
Flow rate [Nm <sup>3</sup> /h]	238000	195860
Inlet temp [°C]	297.7	54.8
Outlet Temp [°C]	171.2	228.7
Pressure Drop [Pa]	580	280
Heat Recovery [kW]	11970	

## 2.4 Enthalpy Wheels and Plate Heat Exchangers

Enthalpy wheels are air-to-air rotating heat recovery devices coated in a desiccant material. These devices recover sensible and latent heat. Sensible heat is the heat that can be felt or measured in terms of a temperature scale while latent heat refers to the moisture content of the air. The fact that they are able to recover sensible and latent heat means that relatively high thermal efficiencies can be attained (Hovac, 2002). The rotor, which has smooth axial channels, serves as the storage mass: half of which is in the hot air stream and the other half of which is in the cold air stream. The storage mass is heated or cooled as it rotates, thus the heat transfer and storage mass temperature vary in the axial direction as well as the angle of orientation of the rotor. From this fact one can conclude that the heat transfer can be influenced by the speed of rotation and the storage mass' dimensions. The process is explained referring to Figure 6 below.

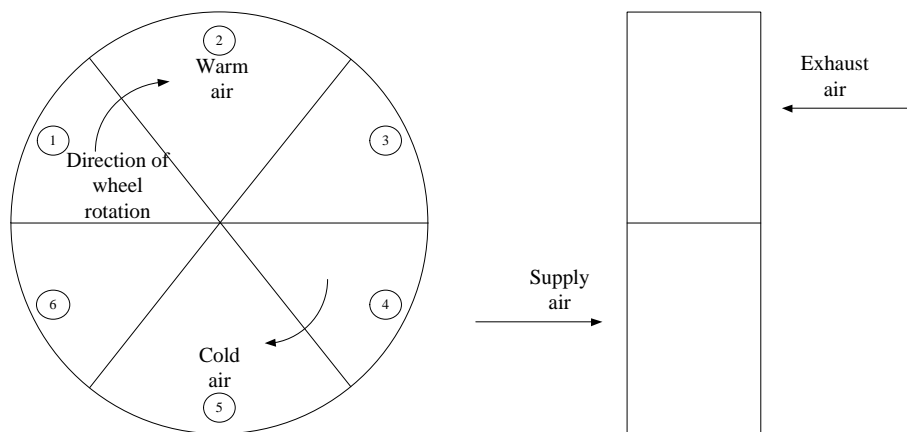


**Figure 6** Enthalpy wheel operation

At point 1 the air channel in question is practically at the cold air temperature, very dry and has just entered into the hot air stream. This is especially true on the cold air inlet side/warm air outlet side. Warm air now flows through the channel and severe cooling of the air takes place. This in turn heats the storage mass. At this point the heat recovery efficiency is very high and condensation can possibly occur.

By the time the storage mass reaches point 2, it has been heated and moisturised substantially and thus the heat transfer rate decreases. The air is no longer cooled as much due to this fact. The channels' axial temperature profile is essentially uniform. Condensation can only occur at this stage if the humidity difference is very large.

As the storage mass reaches point 3, the warm inlet side has virtually reached the warm air stream temperature and is highly moisturised. The heat transfer rate is now very low. As the storage mass moves towards point 4, it moves into the cold air stream. Heat and mass transfer is again severe due to the large temperature and moisture differences between the storage mass and the air stream. The cold air is thus heated and moisturised. Most of the condensate on the storage mass is taken up by the cold air stream. There is also a distinct temperature gradient in the axial direction of the storage mass.

At point 5, the storage mass has been cooled substantially and lost even more moisture. Again, as with point 2, the temperature profile in the axial direction of the storage mass is relatively uniform. By the time point 6 is reached, the storage mass has been severely cooled and little heat transfer takes place. The storage mass then passes again into the warm air section and the cycle is repeated.

The distinct advantage of employing an enthalpy wheel as a heat recovery device is that, due to the total (sensible and latent) heat transfer properties, higher recovery efficiencies can be obtained. Furthermore, the air streams can be orientated in any position, side by side or top and bottom (McQuay, 2001). The enthalpy wheel can also accommodate high face velocities, which implies that

the equipment can be relatively compact. Additionally, the storage masses provide a low pressure drop.

However, McQuay (2001) also highlights the various disadvantages of enthalpy wheels, the main disadvantage being the fact that it has moving parts. Furthermore, Staton (1998) explains that the specialised materials used in some enthalpy wheels are very expensive and tough to manufacture. One also has to consider the fact that the wheels' mechanical parts (belts, motor etc.) will require timeous maintenance. Additionally, cross contamination is very likely to occur, this makes enthalpy wheels highly unsuitable for applications that require a bacteria free supply air, like hospitals, pharmacies and food processing plants. The manufacturing of the wheel itself, with its very small air channels, is also costly.

Plate heat exchangers are heat exchangers that use metal plates to transfer heat between two fluids. The heat exchanger consists of a pack of corrugated metal plates which have portholes for the fluids to flow through. The corrugations promote fluid turbulence, which enhances heat transfer. The plates are packed between a fixed and movable end plate and have gaskets to prevent leakage. The channels are arranged as such that the two fluids flow through alternate channels. An example of a plate heat exchanger is depicted in Figure 7.

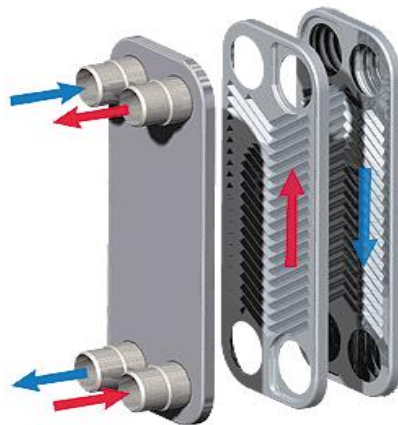


**Figure 7** Exploded view of a plate heat exchanger (obtained from [http://targetequipments.com/plate\\_heat\\_exchanger\\_manufacturers.html](http://targetequipments.com/plate_heat_exchanger_manufacturers.html))

DeWatwal (2009) lists the advantages and disadvantages of plate heat exchangers as follows:

#### Advantages

- High thermal efficiency and a close temperature approach
- Large heat transfer surface area per unit volume
- Small mass
- Multi-fluid stream operation (up to ten streams can exchange heat in one heat exchanger)

- No cross contamination

#### Disadvantages

- Limited range of temperature and pressure
- Difficulty of cleaning passages
- Difficulty of repair in case of failure or leakage between passages

From the information presented in this section one can observe that HPHRHE's are easier to manufacture, install and maintain throughout its life cycle and thus for the purpose of this study the other heat recovery options will not be considered further.

## 2.5 Air Driers

Drying is a process in which moisture is removed from a product by various modes of heat transfer such as radiation, convection and conduction. Mujumdar (1995) explains that radiation drying is a mode of drying that uses purely radiative energy, similar to microwave technology. Conduction drying is when a hot surface is at a distance from the material and the surrounding air is heated by conduction (no air movement), which decreases its relative humidity and thus allows moisture from the material to diffuse into the air. The heating surface never makes contact with the material. In convection drying the heating medium, usually air comes into direct contact with the material, causing diffusion of the moisture in the material into the air. Various types of driers exist, including spray, tunnel, freeze and tray driers. In this study a tray drier is used. A typical tray air drier unit is illustrated in Figure 8 below.

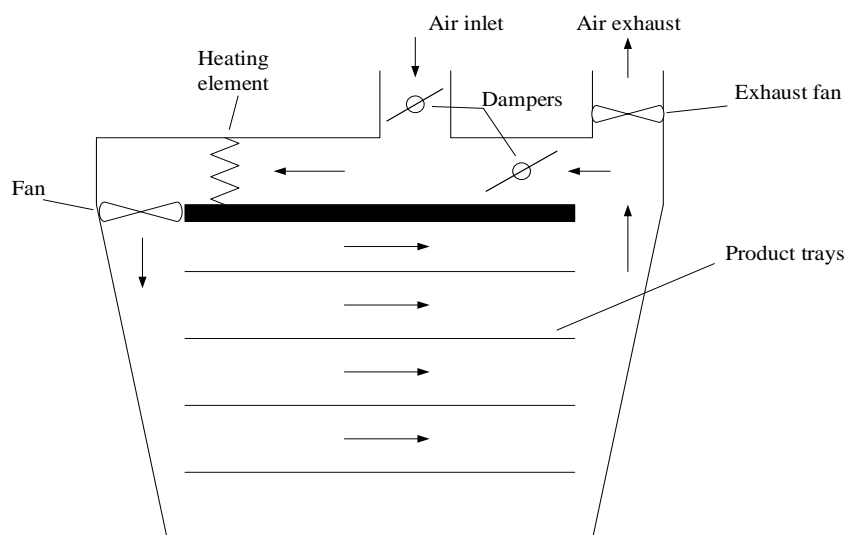


**Figure 8** A typical Air drier unit

Many materials must not be dried too fast otherwise cracking and case hardening will occur. The equilibrium moisture content (the point at which the material has been dried for a long time and the product has the desired moisture content) is also an important parameter to prevent bacterial activity.

The drying rate is dependent on the initial moisture content relative to the equilibrium moisture content of the material and other material properties such as bulk density. Drying rate can be classified as constant rate drying or falling rate drying and the mode of drying depends on the moisture content of the material relative to the equilibrium content at a specific point in time. Another factor that influences the drying time of a material is its composition. While materials have an infinite amount of compositions, for the purposes of this study three different compositions are considered. A porous material is a material consisting of a “matrix” like skeleton and many voids. These materials are usually characterised by their porosity. Due to the large amount of voids, the flow of moisture through these materials is relatively easy. Cellular materials consist of large amounts of cells, joined by their membranes to neighbouring cells. The cells have a very high moisture content and thus initially will allow easy moisture flow, however, as the cells on the outside of the material dry out, the moisture flow is resisted by the irregular shapes of the cells. Granular materials consist of separate solid entities and the grains are typically irregular shaped. This should cause the highest moisture flow resistance.

In constant rate drying, the drying surface is supplied in excess with liquid due to capillary action (Dobson, 2001). A layer of saturated liquid can be observed on the surface of the drying material. The liquid then vaporises due to the heat transfer between the air and the material and it then diffuses into the air stream. The evaporated liquid is soon replenished by the next layer of liquid. The rate at which this layer of liquid can be replenished usually controls the drying rate.

Falling rate drying occurs after the constant rate drying period. This period is characterised by a reduction of liquid area on the surface of the material and progressively slower drying times. The drying rate now only depends on the air temperature and the geometric properties of the material and is not influenced as much by the properties of the air (Sharma *et al*, 2001). Drying in this case is controlled by the ability of the water to diffuse to the surface of the material.



### 3 THEORY

Section 3 describes the thermal modelling of a single thermosyphon, HPHE and drying theory and lists the equations used in the various models.

#### 3.1 Single Thermosyphon Model

Consider a single thermosyphon and its inputs and outputs as illustrated in Figure 9. Heat is transferred (in the case of the evaporator) from the hot fluid stream, through the pipe wall and into the refrigerant inside the thermosyphon. The heat transfer occurs in the opposite direction for the condenser section.

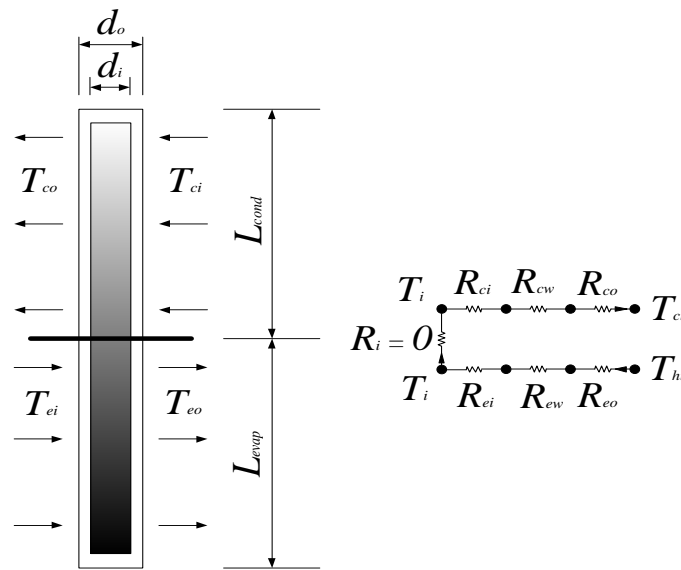


**Figure 9** Thermal resistance model of a single thermosyphon

The thermal resistance diagram shown in Figure 9 indicates all the relevant parameters when evaluating the thermal performance of a thermosyphon. These parameters include all the thermal resistances and the temperature differences across these resistances that cause energy/heat to flow in the direction of the negative temperature gradient. The heat transfer rates of the condenser and evaporator sections can be expressed as

$$\dot{Q}_{cond} = \frac{T_i - \bar{T}_c}{\Sigma R_{cond}} \quad (3.1)$$

$$\dot{Q}_{evap} = \frac{\bar{T}_h - T_i}{\Sigma R_{evap}} \quad (3.2)$$

Assuming no losses in the thermosyphon along its length and radial directions of the pipe, the evaporator and condenser heat transfer rates must be equal, thus

$$\frac{T_i - \bar{T}_c}{\Sigma R_{cond}} = \frac{\bar{T}_h - T_i}{\Sigma R_{evap}} \quad (3.3)$$

Equation 3.3 can be rearranged and the inside temperature,  $T_i$ , eliminated to yield the overall heat transfer for the heat pipe as

$$\dot{Q}_{hp} = \frac{\bar{T}_h - \bar{T}_c}{\Sigma R} \quad (3.4)$$

where

$$\bar{T}_h = \frac{T_{hi} + T_{ho}}{2} \quad (3.5)$$

$$\bar{T}_c = \frac{T_{co} + T_{ci}}{2} \quad (3.6)$$

$$\Sigma R = \Sigma R_{evap} + \Sigma R_{cond} \quad (3.7)$$

The evaporator and condenser thermal resistances represented in the above equations is a combination of the outside, wall and internal resistance of the thermosyphon and are given below

$$\Sigma R_{evap} = R_{ei} + R_{ewall} + R_{eo} \quad (3.8)$$

$$\Sigma R_{cond} = R_{ci} + R_{cwall} + R_{co} \quad (3.9)$$

These resistances will be described individually in the following section.

### 3.1.1 Evaporator internal heat transfer resistance

The liquid which condenses in the condenser forms a falling film down the wall of the heat pipe as discussed in Section 2.2.1. In normal operating conditions, this film persists into the liquid pool at the bottom of the evaporator. For this reason, nucleate and evaporative boiling may occur in the evaporator depending on the heat transfer rate. Of the three possible boiling mechanisms that can occur – nucleate, convection and film boiling – it is established practice to assume nucleate boiling occurs in thermosyphons.

The liquid pool can be divided into three heat transfer sections: natural convection, nucleate boiling and combined convection. In the latter, the former modes combine and contribute to heat transfer. El-Genk and Saber (1997) investigated the liquid pool and liquid film regions in the evaporator. When natural convection is assumed, the heat transfer coefficient can be given as

$$h_{NC} = 0.475 Ra^{0.35} \left( \frac{\frac{\sigma}{\sqrt{g(\rho_l - \rho_v)}}}{d_i} \right)^{0.58} \frac{k_l}{d_i} \quad (3.10)$$

where the Raleigh number can be written as,

$$Ra = \frac{g\beta d_i^4 \dot{q}_e}{k_l \alpha_l \nu_l} \quad (3.11)$$

the nucleate boiling heat transfer coefficient can be given as

$$h_{NB} = (1 + 4.95\psi) h_{KU} \quad (3.12)$$

and the Kutateladze heat transfer coefficient can be written as

$$h_{KU} = 6.95 \times 10^{-4} Pr_l^{0.35} \left( \frac{\dot{q}_e \sqrt{\sigma/g(\rho_l - \rho_v)}}{\rho_v v_l h_{fg}} \right)^{0.7} y^{0.7} \left( \frac{k_l}{d_i} \right) \quad (3.13)$$

where

$$y = \left( \frac{P \sqrt{\sigma/g(\rho_l - \rho_v)}}{\sigma} \right) \quad (3.14)$$

The mixing pool coefficient indicates the contribution by mixing, sliding, and slushing of bubbles as they rise to the nucleate boiling heat transfer and is given as

$$\psi = \left( \frac{\rho_v}{\rho_l} \right)^{0.4} \left( \left( \frac{P v_l}{\sigma} \right) \left( \frac{\rho_l^2}{\sigma g(\rho_l - \rho_v)} \right)^{0.25} \right)^{0.25} \quad (3.15)$$

thus the combined convection coefficient can be expressed as

$$h_{CC} = (h_{NC}^4 + h_{NB}^4)^{0.25} \quad (3.16)$$

To easily identify the different heat transfer regimes, El-Genk and Saber (1997) also introduced a dimensionless pool parameter  $X$ , which is defined as

$$X = \psi Ra^{0.35} Pr_l^{0.35} \left( \frac{P \sqrt{\sigma/g(\rho_l - \rho_v)}}{\sigma} \right)^{0.7} R_{ev}^{0.7} \quad (3.17)$$

with

$$R_{ev} = \frac{\dot{q}_e L_m}{\rho_v v_l h_{fg}} \quad (3.18)$$

and the bubbly length scale as

$$L_m = \sqrt{\sigma/g(\rho_l - \rho_v)} \quad (3.19)$$

For Natural Convection  $X < 10^6$

For Nucleate boiling  $X > 2.1 \times 10^7$

For combined convection  $10^6 \leq X \leq 2.1 \times 10^7$

Similarly, the film region can also be divided into three heat transfer sections: laminar convection, nucleate boiling and combined convection. The wall heat flux exponent,  $n$ , is used to classify the regimes

The laminar convection heat transfer coefficient is given by the equation

$$h_x = \left( \frac{4}{3} \right)^n R_{ev}^{-n} \frac{k_l}{\left( \frac{v_l^2}{g} \left( \frac{\rho_l}{\rho_l - \rho_v} \right) \right)^n} \quad (3.20)$$

Where  $n = 1/3$

When the wall heat flux exponent is between  $0.6 < n < 0.7$ , the nucleate boiling assumption is valid and is given as

$$h_{NB} = 1.155 \times 10^{-3} y N_{\mu f}^{0.333} Pr_l^{0.35} Re_{ev}^{0.7} \left( \frac{P \sqrt{\sigma/g(\rho_l - \rho_v)}}{\sigma} \right)^{0.7} \quad (3.21)$$

Where  $N_{\mu f}$  is the viscosity number and is given by the equation

$$N_{\mu f} = \frac{\mu_l}{(\sigma g \sqrt{\sigma/\rho_l - \rho_v})^{0.5}} \quad (3.22)$$

and

$$y = \frac{k_l}{\left( \frac{v_l^2}{g} \left( \frac{\rho_l}{\rho_l - \rho_v} \right) \right)^{0.333}} \quad (3.23)$$

Using a similar formulation to equation 3.16, the combined convection coefficient can be obtained as

$$h_{CC} = (h_{NC}^3 + h_{NB}^3)^{0.33} \quad (3.24)$$

The liquid film is evaluated by introducing the dimensionless film parameter to differentiate between the different heat transfer regimes and is defined as

$$\eta = Re_{ev}^2 \left( \frac{P \sqrt{\sigma/g(\rho_l - \rho_v)}}{\sigma} \right)^2 \frac{Re_{ev}}{Pr_l} \quad (3.25)$$

Where for

Laminar convection  $\eta \leq 10^9$

Nucleate boiling  $\eta \geq 2.7 \times 10^{10}$

Combined convection  $10^9 < \eta < 2.7 \times 10^{10}$

The boiling mechanisms and equations described above provide a relatively easy analytical analysis of the inside heat transfer coefficient. However, the fluid flow inside the thermosyphons is often a mixture of two phase flow regimes resulting in a very complex flow pattern. For this reason experimental correlations often have to suffice to provide the inside heat transfer coefficients. Imura suggested the following inside heat transfer coefficient (Piro & Piro, 1997)

$$h_{ei} = 0.32 \left( \frac{\rho_l^{0.65} k_l^{0.3} cp_l^{0.7} g^{0.2} \dot{q}_{evap}^{0.4}}{\rho_v^{0.25} h_{fg}^{0.4} \mu_l^{0.1}} \right) \left( \frac{P_{sat}}{P_{amb}} \right)^{0.3} \quad (3.26)$$

Shiraishi used the same equation to correlate his data, but changed the exponent 0.3 to 0.23

$$h_{ei} = 0.32 \left( \frac{\rho_l^{0.65} k_l^{0.3} cp_l^{0.7} g^{0.2} \dot{q}_{evap}^{0.4}}{\rho_v^{0.25} h_{fg}^{0.4} \mu_l^{0.1}} \right) \left( \frac{P_{sat}}{P_{amb}} \right)^{0.23} \quad (3.27)$$

For these equations to be valid, the following conditions were adhered to:  $\dot{q}_e = 1000 - 35000 \text{ W/m}^2$ ,  $T_{sat} = 32 - 60 \text{ }^\circ\text{C}$  and  $V^+ = 50 - 100 \%$

Semena proposed the following relation (Piro & Piro, 1997)

$$h_{ei} = 0.0123 \left( \frac{k_l}{L_m} \right) x^{0.5} \left( \frac{\mu_l c p_l}{k_l} \right)^{0.35} y^{0.54} \left( \frac{d_i}{L_m} \right)^{0.17} \quad (3.28)$$

where

$$y = \frac{P_i}{\sqrt{\sigma g (\rho_l - \rho_v)}} \quad (3.29)$$

$$x = \frac{\dot{q}_{evap} L_m}{h_{fg} \mu_l (\rho_l - \rho_v)} \quad (3.30)$$

with their data set comprising of:  $\dot{q}_e = 6000 - 1100000 \text{ W/m}^2$ ,  $V^+ = 20 - 50 \%$ ,  $d_i = 6 - 24 \text{ mm}$  and  $L_{evap} = 0.25 - 0.7 \text{ m}$ .

The inside heat transfer coefficient can also be predicted by Nusselt theory according to Whalley (1987) as

$$h_{ei} = \frac{\sqrt{8}}{3} \left[ \frac{\rho_l (\rho_l - \rho_v) g h_{fg} k_l^3}{L_{evap} \mu_l (T_{wall} - T_{sat})} \right]^{0.25} \quad (3.31)$$

With the heat transfer coefficient and internal area known, the thermal resistance can be obtained as

$$R_{ei} = \frac{1}{h_{ei} A_{ei}} \quad (3.32)$$

with

$$A_{ei} = \pi d_i L_{evap} \quad (3.33)$$

### 3.1.2 Condenser internal heat transfer resistance

The vapour formed in the evaporator rises and cools again in the condenser. This condensate can return to the evaporator either by filmwise or dropwise condensation. The latter is difficult to model and thus filmwise condensation is always used to model the condensation process in the tube. The assumptions are that the difference in temperature between the tube wall and the vapour are constant and that there are negligible shear stresses between the vapour and liquid phases. Faghri (1995) gives the local heat transfer coefficient as

$$h_z = \frac{k_l}{\delta_z} \left[ \frac{\rho_l (\rho_l - \rho_v) g h_{fg} k_l^3 (h_{fg} + 0.68 c p_l \Delta T_{sat})}{4 \mu_l (\Delta T_{sat}) z} \right]^{0.25} \quad (3.34)$$

the Nusselt number relation locally is thus

$$Nu_z^* = \frac{h_z}{k_l} \left( \frac{g}{v_l^2} \left( \frac{\rho_l - \rho_v}{\rho_l} \right) \right)^{-0.333} \quad (3.35)$$

the local Nusselt number can also be given as

$$Nu_z^* = 0.693 R_{el}^{-0.333} \quad (3.36)$$

where

$$R_{el} = \frac{\dot{Q}_z}{\pi d_i \mu_z (h_{fg@z})} \quad (3.37)$$

The average heat transfer coefficient for the condenser can be obtained by finding the integral of the local heat transfer coefficient for the entire length of the condenser

$$\bar{h} = \frac{1}{L_{cond}} \int_0^{L_c} h_z dz = \frac{\sqrt{8}}{3} \left[ \frac{\rho_l (\rho_l - \rho_v) g k_l^3 (h_{fg} + 0.68 c_{pl} (T_{sat} - T_w))}{\mu_l (T_{sat} - T_w) L_{cond}} \right]^{0.25} \quad (3.38)$$

and the average Nusselt number again obtained similarly to equation 3.36

$$\overline{Nu}^* = \frac{\bar{h}}{k_l} \left( \frac{g}{v_l^2} \left( \frac{\rho_l - \rho_v}{\rho_l} \right) \right)^{-0.333} = 0.925 R_{el,max}^{-0.333} \quad (3.39)$$

where

$$R_{el,max} = \frac{\bar{Q}_{cond}}{\pi d_i \mu_l h_{fg}} \quad (3.40)$$

Faghri (1995) also gives relations for the heat transfer coefficients over different flow regions for the following conditions

For  $R_{el,max} < 325$

$$h_{ci} = 0.925 R_{el,max}^{-0.333} \frac{k_l}{\left( \frac{v_l^2}{g} \left( \frac{\rho_l}{\rho_l - \rho_v} \right) \right)^{0.333}} \quad (3.41)$$

For  $R_{el,max} \geq 325$

$$h_{ci} = 0.0134 R_{el,max}^{0.4} \frac{k_l}{\left( \frac{v_l^2}{g} \left( \frac{\rho_l}{\rho_l - \rho_v} \right) \right)^{0.333}} \quad (3.42)$$

Uehara et al. (1983) however propose the following correlations (Faghri, 1995)

For  $0.5 < R_{el,max} f_\phi < 325 Pr_l^{0.96}$

$$h_{ci} = 0.884 (R_{el,max} f_\phi)^{-1/4} \frac{k_l}{\left[ \frac{v_l^2}{g} \left( \frac{\rho_l}{\rho_l - \rho_v} \right) \right]^{1/3}} \quad (3.43)$$

For  $R_{el,max} f_\phi \geq 325 Pr_l^{0.96}$

$$h_{ci} = 0.044 (R_{el,max} f_\phi)^{1/6} Pr_l^{2/5} \frac{k_l}{\left[ \frac{v_l^2}{g} \left( \frac{\rho_l}{\rho_l - \rho_v} \right) \right]^{1/3}} \quad (3.44)$$

The following equation is attributable to Wang and Ma (1991) and is presented as (Faghri, 1995)

$$h_{ci} = h_z \left[ P_{sat}^{0.37} \left( \frac{2L_{cond}}{d_i} \right)^{-1/4} (0.41 - 0.72V^+ + xy) \right] \quad (3.45)$$

where

$$x = -62.7V^{+2} + 14.5V^+ + 7.1 \quad (3.46)$$

$$y = \left(\frac{\pi}{2} - \phi\right) / 1000 \quad (3.47)$$

and  $V^+ = V_l/V_{tot} \geq 0.1$  for their experiments,  $h_z$  is the Nusselt heat transfer coefficient and  $\phi$  is measured from the vertical. Once the heat transfer coefficient is calculated, the thermal resistance is calculated as follows

$$R_{ci} = \frac{1}{h_{ci}A_{ci}} \quad (3.48)$$

where

$$A_{ci} = \pi d_i L_{cond} \quad (3.49)$$

### 3.1.3 Thermal resistance across the thermosyphons walls

To obtain the thermal resistance across the walls, Fourier's law of conduction through a cylindrical layer may be used (Cengel, 2004)

$$\dot{Q}_{pipe} = 2\pi k_{pipe} L_{pipe} \frac{T_i - T_o}{\ln(d_o/d_i)} \quad (3.50)$$

and

$$R_{cw,ew} = \frac{\ln(d_o/d_i)}{2\pi k_{pipe} L_{pipe}} \quad (3.51)$$

### 3.1.4 Outside heat transfer resistance

Forced and natural convection analysis is utilised to find the heat transfer coefficient for a thermosyphon. Natural convection is used to analyse the single thermosyphon, while forced convection is used to find the heat transfer coefficient for a tube bundle as presented in Section 3.2. Churchill proposed the following relations

$$\begin{aligned} \text{For laminar flow, } R_{aL} &\leq 10^9 \\ \overline{Nu}_L &= 0.68 + 0.67(R_{aL}\Psi)^{0.25} \end{aligned} \quad (3.52)$$

$$\begin{aligned} \text{For turbulent flow, } 10^9 &\leq R_{aL} \leq 10^{12} \\ \overline{Nu}_L &= 0.68 + 0.67(R_{aL}\Psi)^{0.25} (1 + 1.6 \times 10^{-8} R_{aL}\Psi)^{0.0833} \end{aligned} \quad (3.53)$$

where

$$\Psi = \left(1 + \left(\frac{0.492}{Pr}\right)^{0.5625}\right)^{-1.778} \quad (3.54)$$

having these relations, the outside heat transfer coefficient can be calculated as

$$h_{co,eo} = \left(\frac{k_{air}}{L_{cond,evap}}\right) \overline{Nu}_L. \quad (3.55)$$

The thermal resistance can then be determined in similar fashion to equation 3.48.

### 3.2 Heat Exchanger Model

A HPHE consists of a collection of tubes that are orientated in a staggered or aligned sequence relative to the flow direction and can be finned or un-finned. The common tube bank configurations used in industry consist of un-finned individual tubes, plate-and-tube and individually finned tubes. These configurations are analysed to establish an outside thermal resistance and added to the wall and internal resistances to yield an overall thermal resistance value. The internal and wall resistances are simply modelled as described in Section 3.1, while the outside thermal resistances are calculated by the theory discussed in this section.

#### 3.2.1 Un-finned individual tubes

This tube bank configuration consists of tubes that have no fins and can be arranged in an aligned or staggered manner. The arrangements are indicated in Figure 10

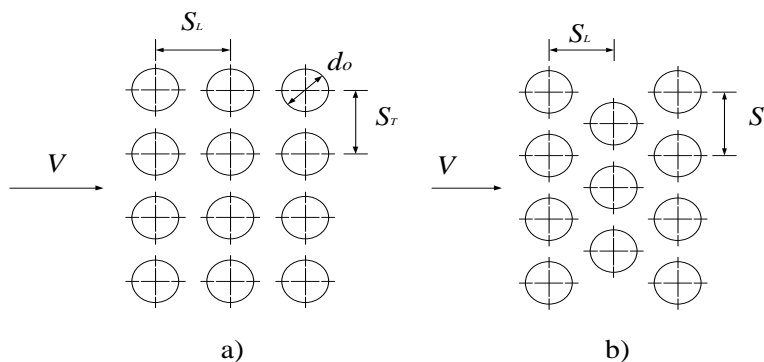


**Figure 10** Un-finned tube bundle configurations, a) aligned, b) staggered

To find the Reynolds number the velocities between the tubes need to be calculated. Due to the fact that the flow area decreases when the fluid is in-line with the specific tube row and the air has no other route to discharge, the velocity needs to be adjusted to maintain the mass balance. This can be expressed as

$$\bar{V} = V \left( \frac{S_T}{S_T - (\pi/4)d_o} \right) \quad (3.56)$$

the Reynolds number can then be found using standard fluid flow relations

$$Re_d = \frac{\rho \bar{V} d}{\mu} \quad (3.57)$$

the Churchill relations can then be used to find the average Nusselt number between two adjacent tubes in the same row

For  $Re_d < 10^4$

$$\overline{Nu}_d^1 = 0.3 + \frac{0.62 Re_d^{0.5} Pr^{0.333}}{\left(1 + (0.4/Pr)^{0.666}\right)^{0.25}} \quad (3.58)$$

For  $2 \times 10^4 < Re_d < 4 \times 10^5$



$$\overline{Nu}_d^1 = 0.3 + \frac{0.62Re_d^{0.5}Pr^{0.333}}{(1+(0.4/Pr)^{0.666})^{0.25}} \left[ 1 + \left( \frac{Re_d}{282000} \right)^{0.5} \right] \quad (3.59)$$

For  $4 \times 10^5 < Re_d < 5 \times 10^6$

$$\overline{Nu}_d^1 = 0.3 + \frac{0.62Re_d^{0.5}Pr^{0.333}}{(1+(0.4/Pr)^{0.666})^{0.25}} \left[ 1 + \left( \frac{Re_d}{282000} \right)^{0.625} \right]^{0.8} \quad (3.60)$$

If the tube bank has fewer than 10 rows, the average Nusselt number is given as

$$\overline{Nu}_d^{-10} = \frac{1+(N_r-1)\phi}{N_r} \overline{Nu}_d^1 \quad (3.61)$$

for tube banks of more than ten rows the average Nusselt number is calculated as

$$\overline{Nu}_d^{+10} = \phi \overline{Nu}_d^1 \quad (3.62)$$

the arrangement factor  $\phi$  can be expressed as

$$\phi_{aligned} = 1 + \frac{0.7}{\psi^{1.5}} \frac{S_L/S_T^{-0.3}}{(S_L/S_T+0.7)^2} \quad (3.63)$$

$$\phi_{staggered} = 1 + \frac{2}{3} P_L \quad (3.64)$$

The dimensionless transverse and longitudinal pitches used in the factor  $\Psi$  are

$$\psi = 1 - \pi/4P_T \quad \text{if } P_L \geq 1 \quad (3.65)$$

$$\psi = 1 - \pi/4P_T P_L \quad \text{if } P_L < 1 \quad (3.66)$$

and the pitches are

$$P_T = S_T/d_o \quad \text{and} \quad P_L = S_L/d_o \quad (3.67)$$

Once the Nusselt number is obtained the heat transfer coefficient can be calculated as in equation 3.55. The thermal resistance is calculated by using equation 3.68 below, and factoring in the fact that the total thermal resistance takes into account all the tubes in the tube row

$$R_{co,eo} = \frac{1}{h_{co,eo} A_{cf,ef}} \quad (3.68)$$

where

$$A_{cf,ef} = \pi d_o L_{cond,evap} N_p \quad (3.69)$$

### 3.2.2 Plate-and-Tube configuration

This configuration consists of circular tubes connected by continuous plates at set spaces from each other along the length of the tubes. Figure 11 illustrates this.

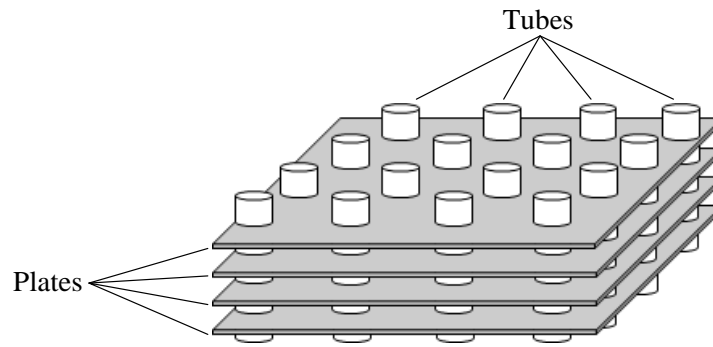


**Figure 11** Plate-finned tube bundle configuration

The arrangement of the tubes can be staggered or aligned, but general practice is to have a staggered tube layout. Meyer (2003) presents a method described by Kroger (1998) to analyse the control volume, and this method is utilised. The control volume used in the analysis is illustrated in Figure 12

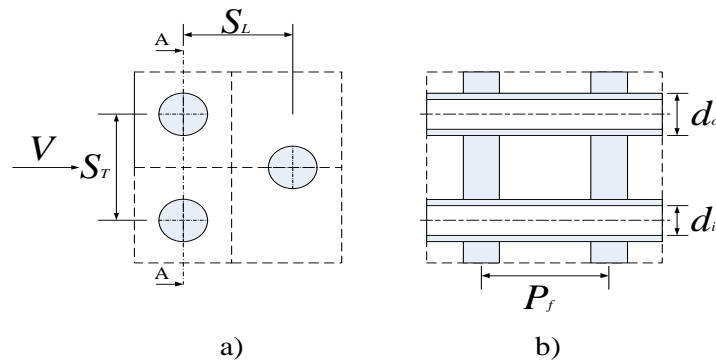


**Figure 12** Plate-and-tube control volume, a) plan view b) cut-away view

The frontal flow area is given as

$$A_{cvfr} = S_T P_f \quad (3.70)$$

the flow area is then decreased when the fluid moves past the tubes, this minimum free flow area is given as

$$A_{cvc} = (S_T - d_o)(P_f - t_f) \quad (3.71)$$

an area ratio can then be defined as

$$\sigma = A_{cvc} / A_{cvfr} \quad (3.72)$$

the area of the plate/fin in contact with the air stream is the longitudinal and transverse pitches, minus the total area of the tubes in the control volume area for the upper and lower plate, thus

$$A_{cvf} = 2 \left( S_L S_T - \pi d_o^2 / 4 \right) \quad (3.73)$$

hence, the total area of the control volume exposed to the air stream is

$$A_{cvair} = A_{cvf} + (P_f - t_f)(\pi d_o) \quad (3.74)$$

the mass velocity through the minimum free flow area is

$$G_{cvc} = \dot{m}/A_{cvc} \quad (3.75)$$

and the hydraulic diameter can be calculated as

$$d_h = 4A_{cvc}S_L/A_{cva} \quad (3.76)$$

from this the Reynolds number can be calculated as

$$Re_d = G_{cvc}d_h/\mu_{air} \quad (3.77)$$

Pirotto (1997) suggests the method used by Colburn to calculate the heat transfer coefficient by obtaining the Colburn j-factor.

$$j = StPr^{0.67} = \frac{Nu_dPr^{0.67}}{PrRe_d} = \frac{hPr^{0.67}}{G_{cvc}c_p} \quad (3.78)$$

For tube banks with 4 or more rows, Nuntaphan et. al (2002) proposed the adjustment expressed below

$$j_{N_r \geq 4} = 0.14Re_d^{-0.328} \left(\frac{S_T}{S_L}\right)^{-0.502} \left(\frac{P_f - t_f}{d_o}\right)^{0.031} \quad (3.79)$$

and Webb (1992) proposed the following for tube banks of less than 4 rows

$$j_{N_r < 4} = 0.991j_{N_r \geq 4} \left(2.24Re_d^{-0.092} \left(\frac{N_r}{4}\right)^{-0.031}\right)^{0.607(4-N_r)} \quad (3.80)$$

once the Colburn j-factor is found, the heat transfer coefficient can be obtained using equation 3.78, the thermal resistance is then given as

$$R_{co, eo} = \frac{1}{(h_{co, eo}A_{cvc}L_{cond, evap}N_p/P_f)} \quad (3.81)$$

### 3.2.3 Plain individually finned tubes

This configuration consists of individual circular tubes which have circular finned tubes along their length at set distances. The configuration is illustrated in Figure 13

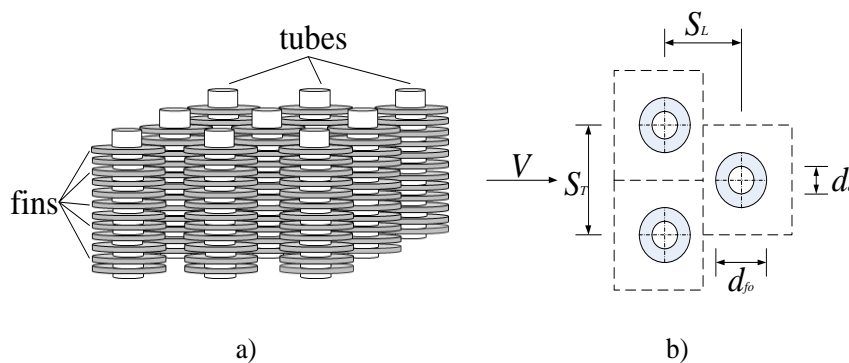


**Figure 13** Individually finned tube a) configuration and b) control volume

The method of analysis is the same as in Section 3.2.2, however, the Colburn j-factors differ and are given by Webb (1992) for more than 4 tube rows as

$$j_{N_r \geq 4} = 0.134 Re_d^{-0.319} (s/e)^{0.2} (s/t_f)^{0.11} \quad (3.82)$$

and for less than 6 rows

$$j_{N_r < 6} = j_4 \left( 1 + \frac{G_{cvc}}{\rho N_f^2} \right)^{-0.14} \quad (3.83)$$

where  $s$  is the spacing between two fins and  $e$  is the fin height given by

$$s = (P_f - t_f) \quad \text{and} \quad e = (d_{fo} - d_o)/2 \quad (3.84)$$

The heat transfer coefficient and the thermal resistance is calculated similar to Section 3.2.2

### 3.4 Drying Theory

Drying is a very energy intensive process. Mujumdar (2001) states that drying consumes up to 10 % of the total energy required in the food industry. Compounding this is the fact that drier selection is often driven by desired product quality and not by energy considerations. Thus it is important that an energy minimization mechanism be incorporated into the drying system.

Drying can be stated as any process which involves moisture removal from a product by a heat and mass transfer process. Heat transfer causes liquid on the surface of the product, which is exposed to the air stream, to evaporate and forces the vapour pressure of the moisture to be higher than the surrounding air. Mass transfer is driven by the concentration differences between the inside and surface of the product and likewise by the difference between the surface and the surrounding air. These mechanisms will be discussed in the following sections for the material and the air drying process. Unless otherwise stated, all information is obtained from Dobson (2001) and Mafokeng (2011).

#### 3.4.1 Heat transfer mechanism

Consider a flat sample, as depicted in Figure 14, of a material that is to be dried. Heat is transferred by conduction, convection and radiation (Cengel, 2006). Radiation is assumed to be incorporated in the convective heat transfer mechanism and is not considered exclusively in this document.

Conduction occurs when energy is transferred from particles at a higher state of energy to particles with a lower state of energy within a body. In drying it plays an important role because it allows heat transfer within the material being dried.

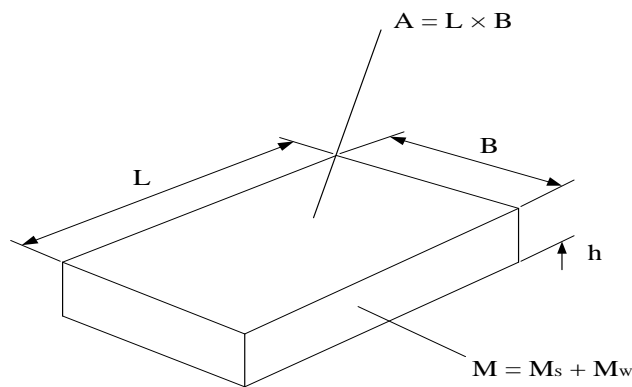


**Figure 14** Mass sample

Conduction can be determined from Fourier's law

$$\dot{Q}_{cond} = kA \frac{T_1 - T_2}{\Delta x} = -kA \frac{dT}{dx} \quad (3.85)$$

Convection occurs when energy is transferred between a solid/fluid surface and an adjacent gas/fluid in motion. The convection heat transfer rate can be determined using Newton's law of cooling

$$\dot{Q}_{conv} = hA(T_s - T_f) \quad (3.86)$$

The change in temperature in the medium can be given by the conservation of energy equation

$$\frac{\Delta E}{\Delta t} = \sum \dot{E}_{in} - \sum \dot{E}_{out} \quad (3.87)$$

if the effects of kinetic and potential energy are ignored, equation 3.87 becomes

$$\frac{\Delta U}{\Delta t} = \dot{Q}_1 - \dot{Q}_2 \quad (3.88)$$

defining

$$U = mc_p T \quad (3.89)$$

equation 3.88 can be written, after taking the limit, as

$$mc \frac{dT}{dt} = -\frac{d\dot{Q}}{dx} \quad (3.90)$$

and substituting equation 3.85 into equation 3.90 yields the following

$$mc \frac{dT}{dt} = kA \frac{d^2 T}{dx^2} \quad (3.91)$$

thus the average temperature within the sample can be determined by

$$\frac{dT}{dt} = \frac{kA}{mc} \frac{d^2 T}{dx^2} \quad (3.92)$$

### 3.4.2 Mass transfer mechanism

Mass transfer takes place when a component moves from one position to another within a medium or out of the medium. Component concentration difference drives mass transfer, analogous to temperature difference for heat transfer. Consider a flat plate as displayed in Figure 15

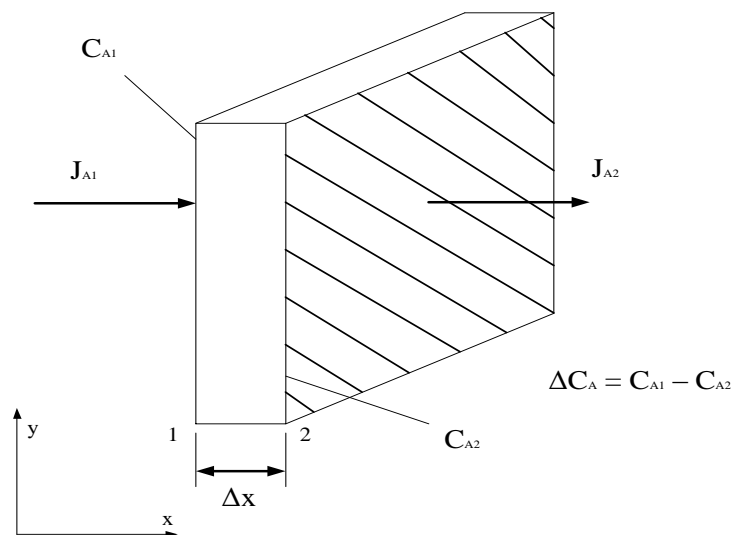


**Figure 15** Concentration Mass sample

The flat plate contains two components (A and B). The concentration of A in B varies along the x-axis. The conservation of mass for the plate can be written as

$$\frac{\Delta m}{\Delta t} = \sum \dot{m}_1 - \sum \dot{m}_2 \quad (3.93)$$

Fick's first law - which states that the molar flux of a component due to diffusion is directly proportional to the concentration gradient and inversely proportional to the distance of diffusion - can be used to determine the mass flow rate of component A from position 1 to 2. This is expressed as

$$J_{A(1 \rightarrow 2)} = -D_{AB} \frac{dC_A}{dx} \quad (3.94)$$

and

$$\dot{m}_{AB} = -D_{AB} A \frac{dC_A}{dx} \quad (3.95)$$

where  $J_{A(1 \rightarrow 2)}$  is the rate of diffusion of component A and  $D_{AB}$  the diffusivity of component A in component B. Also, the mass of component A in component B can be written a

$$m = \Delta x A C_A \quad (3.96)$$

therefore,

$$\frac{\Delta(\Delta x A C_A)}{\Delta t} = \left( -D_{AB} A \frac{\Delta C_{A1}}{\Delta x} \right) - D_{AB} \frac{\Delta C_{A2}}{\Delta x} \quad (3.97)$$

rearranging yields

$$\frac{\Delta C_A}{\Delta t} = D_{AB} \frac{1}{\Delta x} \left( \frac{\Delta C_{A2}}{\Delta x} - \frac{\Delta C_{A1}}{\Delta x} \right) = D_{AB} \frac{1}{\Delta x} \Delta \left( \frac{\Delta C_A}{\Delta x} \right) \quad (3.98)$$

And taking the limit yields Fick's second law

$$\frac{dC_A}{dt} = D_{AB} \frac{d^2 C_A}{dx^2} \quad (3.99)$$

which characterises liquid diffusion in a product being dried.

### 3.4.3 Air drying process

The onset of drying occurs when the vapour pressure of the moisture on the surface of the drying product is higher than the vapour pressure of the air. Thus the moisture has to move from the inside of the sample to the surface from where it can evaporate. Moisture content determines the “dryness” of a product. This can be determined by measuring the mass of a sample and calculating the bone dry mass of the solids. The moisture content can be defined in two ways. The first defines the moisture content on a dry basis as

$$X_{db} = \frac{m_w}{m_s} \text{ [kg - water/kg - solids]} \quad (3.100)$$

or on a wet basis as

$$X_{wb} = \frac{m_w}{m_w m_s} \text{ [kg - water/kg - (water + solids)]} \quad (3.101)$$

The equations above can be solved simultaneously to obtain the relationship between the two moisture content definitions as

$$X_{db} = \frac{X_{wb}}{1 - X_{wb}} \quad \text{or} \quad X_{wb} = \frac{X_{db}}{1 + X_{db}} \quad (3.102)$$

The rate of change of the moisture content indicates the drying rate. As mentioned in Section 2.5, two distinct drying periods exist which are discussed below.

#### *Constant-rate drying*

Constant-rate drying occurs due to evaporation of the moisture from the surface of the product. The surface is supplied with an excessive amount of liquid by capillary action.

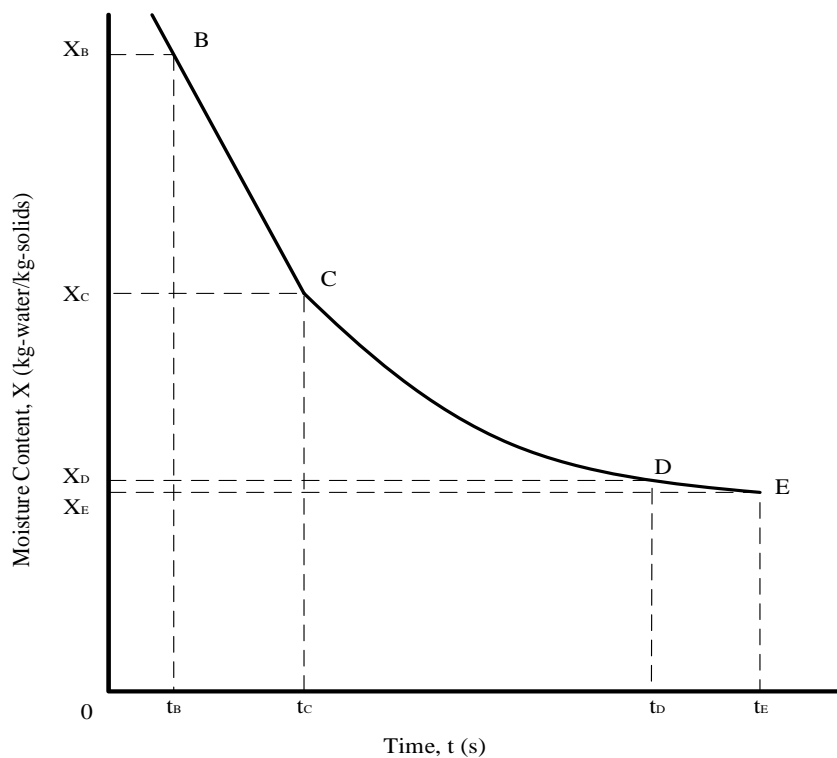


**Figure 16** Moisture content of sample

The rate of drying is determined by how much moisture can evaporate from the surface. Using Figure 16, the moisture content of the sample, as a function of time, between points B and C can be given as

$$X = a + bt \quad (3.103)$$

where the constants  $a$  and  $b$  can be expressed as

$$a = X_B - \frac{X_B - X_C}{t_B - t_C} t_B \quad \text{and} \quad b = \frac{X_B - X_C}{t_B - t_C} \quad (3.104)$$

### ***Falling-rate drying***

The falling rate drying period is controlled by the ability of the water to diffuse to the surface of the material. This is dependent on the material geometry, composition and the moisture content which is not uniform throughout the material. The local moisture content of the material is often not of practical importance and is difficult to measure, thus the average moisture content,  $\bar{X}$ , is of interest. The normalised moisture content can then be given, as a function of time, by the general solution to a second order differential equation

$$\theta = \frac{\bar{X} - X_E}{X_0 - X_E} = a_0 e^{-b_0 \frac{Dt}{L^2}} + a_1 e^{-b_1 \frac{Dt}{L^2}} + a_2 e^{-b_2 \frac{Dt}{L^2}} + \dots \quad (3.105)$$

For small values of  $Dt/L^2$ , in the region C to D of the drying curve, the first term of equation 3.105 is significant, and the normalised moisture content can be approximated by the equation

$$\theta = \frac{\bar{X} - X_D}{X_0 - X_D} = a_0 e^{-b_0 \frac{Dt}{L^2}} = a_{CD} e^{-b_{CD} t} \quad (3.106)$$

where

$$b_{CD} = \frac{\ln(X_C/X_D)}{t_D - t_C} \quad \text{and} \quad a_{CD} = X_D e^{\frac{\ln(X_C/X_D)}{t_D - t_C} t_D} \quad (3.107)$$

A more involved solution requires evaluating the moisture content of the sample over its dimensions. Consider the moisture content of a sample over its length as depicted in Figure 17.



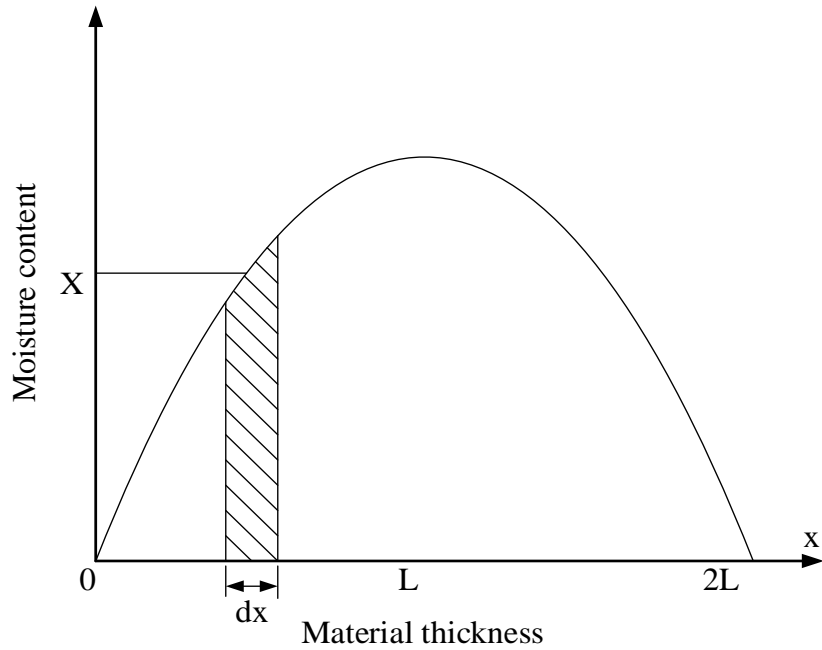


**Figure 17** Moisture content of sample relative to position

The average moisture content is defined by the area under the curve,

$$Area = \int_0^{2L} X dx = \frac{1}{L} \int_0^L X dx \quad (3.108)$$

where  $X$  is the solution of the Ficks second law and is given by

$$X = X_E + 2(X_0 - X_E) \sum_{n=0}^{\infty} \left[ \frac{(-1)^n}{(n+0.5)\pi} e^{-\frac{(n+0.5)^2 \pi^2 Dt}{L^2}} \cos \frac{(n+0.5)\pi x}{L} \right] \quad (3.109)$$

Substituting and integrating yields the average moisture ratio and thus equation 3.106 can be written as

$$\theta = \frac{\bar{X} - X_E}{X_0 - X_E} = 2 \sum_{n=0}^{\infty} \left[ \frac{(-1)^n}{(n+0.5)^2 \pi^2} \sin(n + 0.5) e^{-\frac{(n+0.5)^2 \pi^2 Dt}{L^2}} \right] \quad (3.110)$$

Table 2 indicates the values of the average moisture ratio as a function of  $Dt/L^2$  calculated from equation 3.106. For three dimensional diffusion, the average moisture ratios of  $Dt/L_1^2$ ,  $Dt/L_2^2$ ,  $Dt/L_3^2$  and their product will be the solution for a finite material, much like transient heat transfer is treated.

**Table 2** Dimensionless moisture ratio as per equation 3.106 (Dobson, 2001)

$\frac{Dt}{L^2}$	$\theta = \frac{\bar{X} - X_E}{X_0 - X_E}$	$\frac{Dt}{L^2}$	$\theta = \frac{\bar{X} - X_E}{X_0 - X_E}$	$\frac{Dt}{L^2}$	$\theta = \frac{\bar{X} - X_E}{X_0 - X_E}$
0.00	1	0.1	0.6432	1.1	0.0537
0.01	0.8871	0.2	0.4959	1.2	0.0411
0.02	0.8404	0.3	0.3868	1.3	0.0328
0.03	0.8045	0.4	0.3021	1.4	0.0256
0.04	0.7743	0.5	0.2360	1.5	0.02
0.05	0.7477	0.6	0.1844	1.6	0.0156
0.06	0.7236	0.7	0.1441	1.7	0.0122
0.07	0.7014	0.8	0.1126	1.8	0.0095
0.08	0.6808	0.9	0.0879	1.9	0.0074
0.09	0.6615	1	0.0687	2	0.005

In most cases the rate of change of the average moisture content is desired, for rectangular samples the drying rate can be obtained by simplifying and differentiating equation 3. 106 and solving for the drying rate yields

$$\frac{d\bar{X}}{dt} = (\bar{X} - X_E) \left( \frac{1}{L_1^2} + \frac{1}{L_2^2} + \frac{1}{L_3^2} \right) D \quad (3.111)$$

if the diffusion coefficient, D, of a material in another material is known, the drying rate can then be determined using equation 3.111.

#### 3.4.4 Constant-rate drying period time prediction

In the constant rate drying period, the surface of the drying material in contact with the air flow remains completely wetted, essentially acting as if the solid was not present. Thus the rate of evaporation is the same as for evaporation from a free liquid surface under the same conditions. Drying occurs by mass transfer from the surface to the environment. Thus, the rate of heat transfer to the free liquid surface plays an important part in this drying period. At steady conditions, the mass transfer from the surface to the environment, which is the rate of energy change from liquid to vapour, equals the rate of heat transfer into the material to be dried. A drying rate curve is shown in Figure 18.

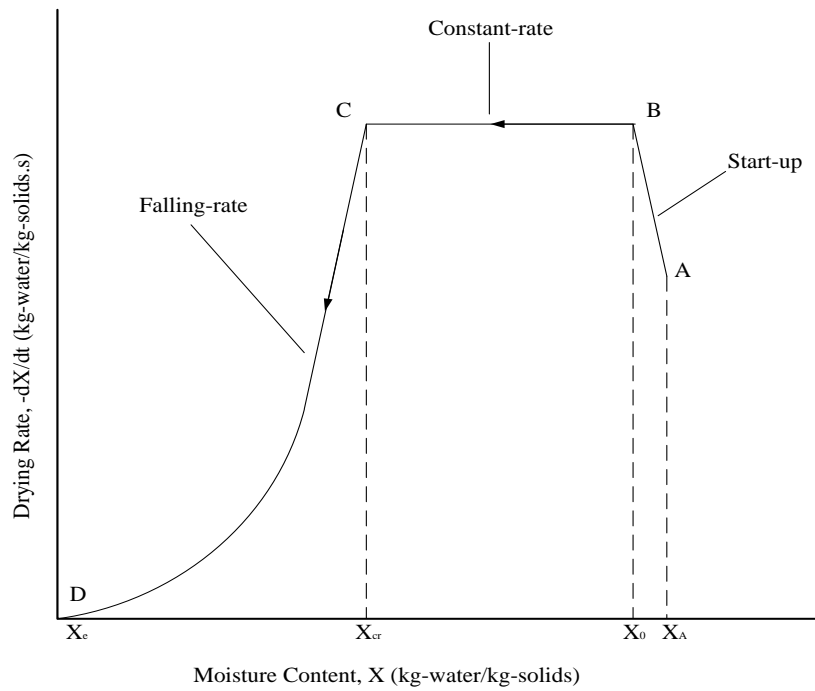


**Figure 18** Typical drying rate curve

It is assumed that the initial difference between the moisture content at the very beginning ( $X_A$ ) and the moisture content at the start of the constant-rate drying period ( $X_0$ ) is negligible. Neglecting effects of radiation and assuming the drying trays are metal matrices which store a negligible amount of heat energy, the drying equation can be written as

$$\dot{Q}_s = hA(T_\infty - T_s) \quad (3.112)$$

where the subscript “s” indicates the free liquid surface, which is at the wet bulb temperature of the air. The heat energy required to vaporise the water from the liquid surface is

$$\dot{Q}_{evap} = \dot{m}_{evap} h_{fg} \quad (3.113)$$

where, in this case,  $\dot{m}_{evap}$  is the mass flowrate of water from the liquid surface. These two equations can be equated and the following equation obtained

$$\dot{Q} = hA(T_\infty - T_s) = \dot{m}_{evap} h_{fg} \quad (3.114)$$

and rearranging gives

$$\dot{m}_{evap} = \frac{hA(T_\infty - T_s)}{h_{fg}} \quad (3.115)$$

Alternatively, the mass flowrate from the surface could be obtained using Fick’s law

$$\frac{\dot{m}_{evap}}{A} = k_1 \frac{(C_w - C)}{(x_w - x)} = k_2 (C_w - C) = k_3 (X_w - X) = k(P_{sat}@T_w - P_v) \quad (3.116)$$

rearranging equation 3.115 would yield the mass flowrate due to pressure differences. The heat transfer coefficient can be predicted using the following correlations

For air flows parallel to the surface and velocities between 0.5 and 7.6 m/s

$$h = 14.3\rho V^2 \quad (3.117)$$

and for air flows perpendicular to the surface and velocities between 0.9 and 4.6 m/s

$$h = 24.2\rho V^2 \quad (3.118)$$

### **Mass transfer**

As the air flows over the wet surface of the product, water is transferred to the air due to a moisture concentration difference. Analogous to heat transfer, the mass transferred from the surface to the air can be given as

$$\frac{\dot{m}_{evap}}{A} = k_m(\phi_s - \phi_{air}) \quad (3.119)$$

The mass transfer coefficient can be determined in a similar way to the heat transfer coefficient. The Sherwood number, which is equivalent to the Nusselt number, is calculated by the relation

$$Sh = \frac{\left(\frac{k_m}{M_w}\right)d}{\left(\frac{\rho D_m}{M_{air}}\right)} \quad (3.120)$$

The Schmidt number, which is the equivalent of the Prandtl number for heat transfer, can be defined as

$$Sc = \frac{\mu}{\rho D_m} \quad (3.121)$$

The Reynolds number of the air is also required. It is expressed as

$$Re = \frac{\rho V d}{\mu} \quad (3.122)$$

Where  $d$  is a characteristic length calculated from the material geometry. The velocity,  $V$  of the air is calculated using the conservation of mass. Correlations between the dimensionless numbers exist for different drying applications and can be used in these respective situations.

The drying time prediction for the constant rate drying period can be written as

$$\dot{m}_{evap} = \frac{X_0 - X_{cr}}{t_{0 \rightarrow cr}} \quad (3.123)$$

Combining equations 3.123 and 3.115 the drying time can be given as

$$t_{0 \rightarrow cr} = \frac{h_{fg}(X_0 - X_{cr})}{hA(T_\infty - T_s)} \quad (3.124)$$

### **3.4.5 Falling-rate drying period time prediction**

The falling rate drying period occurs from the critical moisture content ( $X_{cr}$ ) to the equilibrium moisture content ( $X_e$ ). The product temperature increases in magnitude above the wet bulb temperature and the moisture removal is controlled by the internal structure of the product. Thus,

geometry also plays a role in this drying period. For an infinite plate geometry, for example a flat cake or rusks, the moisture content can be predicted by

$$\frac{\bar{X}-X_e}{X_{cr}-X_e} = \frac{8}{\pi^2} \exp\left(\frac{-\pi^2 D t_{cr \rightarrow e}}{4d_c^2}\right) \quad (3.125)$$

Solving equation 3.125 the drying time for an infinite plate during the falling rate period can be written as

$$t_{cr \rightarrow e} = \frac{4d_c^2}{\pi^2 D} \ln \left[ \frac{8}{\pi^2} \left( \frac{X_{cr}-X_e}{\bar{X}-X_e} \right) \right] \quad (3.126)$$

for an infinite cylinder the drying time can be predicted by

$$t_{cr \rightarrow e} = \frac{d_c^2}{\beta^2 D} \ln \left[ \frac{4}{\beta^2} \left( \frac{X_{cr}-X_e}{\bar{X}-X_e} \right) \right] \quad (3.127)$$

where  $\beta$  is the solution to the first-order Bessel function which equals 2.4028. For a sphere,

$$t_{cr \rightarrow e} = \frac{d_c^2}{\pi^2 D} \ln \left[ \frac{6}{\pi^2} \left( \frac{X_{cr}-X_e}{\bar{X}-X_e} \right) \right] \quad (3.128)$$

Using equations 3.126-128 and the constant rate drying time given in equation 3.124, the total drying time can be determined as

$$t = t_{cr \rightarrow e} + t_{0 \rightarrow cr} \quad (3.129)$$

#### 4 ALGORITHM

A simple iterative numerical solution is used to solve the heat transfer equations for each control volume shown in Figure 19. The energy balance equation is solved at each row of pipes and the obtained values used as the input values for the next row. Figure 19 illustrates that the air streams are adjacent, but the same reasoning applies for a separated-HPHE. The procedure is as follows:

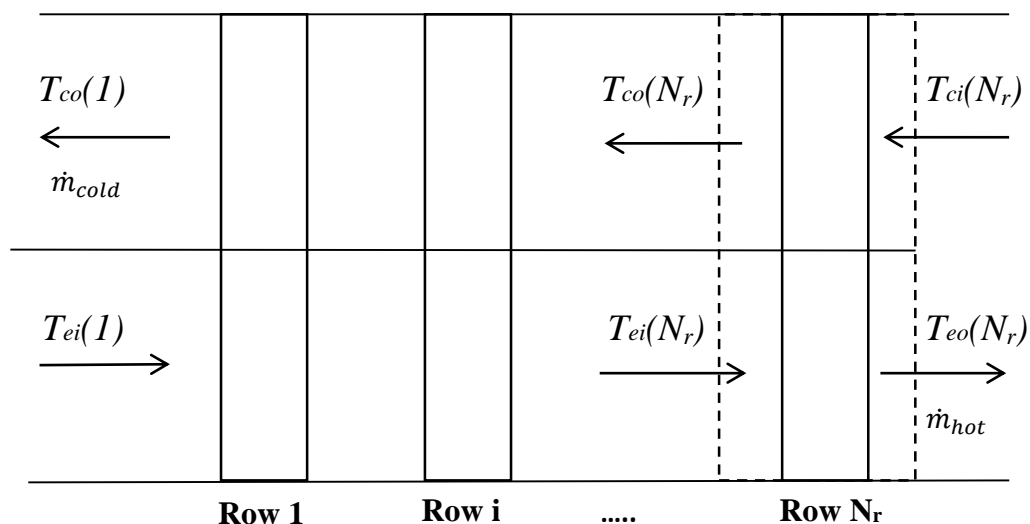


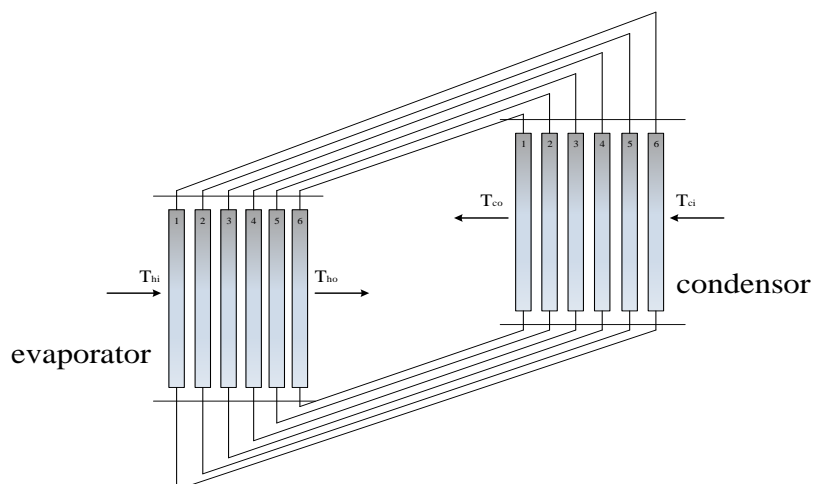
**Figure 19** Numerical algorithm control volume

The heat exchanger was originally specified for the installation at a local biscuit manufacturing plant, NibbliBits (Pty) Ltd. The geometric properties of the separated-HPHE were limited by the factory design specifications, and hence had the following specifications shown in Table 3:

**Table 3** Heat exchanger specifications

Working Fluid	R134a	
Tube material	Copper	
Plate material	Aluminium	
Inlet hot temperature	72	°C
Inlet cold temperature	15	°C
Evaporator and condenser air mass flow rate	0.7	kg/s
Tube bank configuration	Plate-and-tube	
Evaporator and condenser length	0.35	m
Number of tube rows	6	
Number of tubes per row	11	
Longitudinal and transverse pitch	0.0381	m
Fin pitch	10	Fins/in
Fin thickness	0.0002	m
Outside diameter of tubes	0.01588	m
Inside diameter of tubes	0.01490	m

A schematic of the heat exchanger is shown in Figure 20.

**Figure 20** Separated-HPHRHE schematic

A flow diagram of the computer program operation is shown in Figure 21

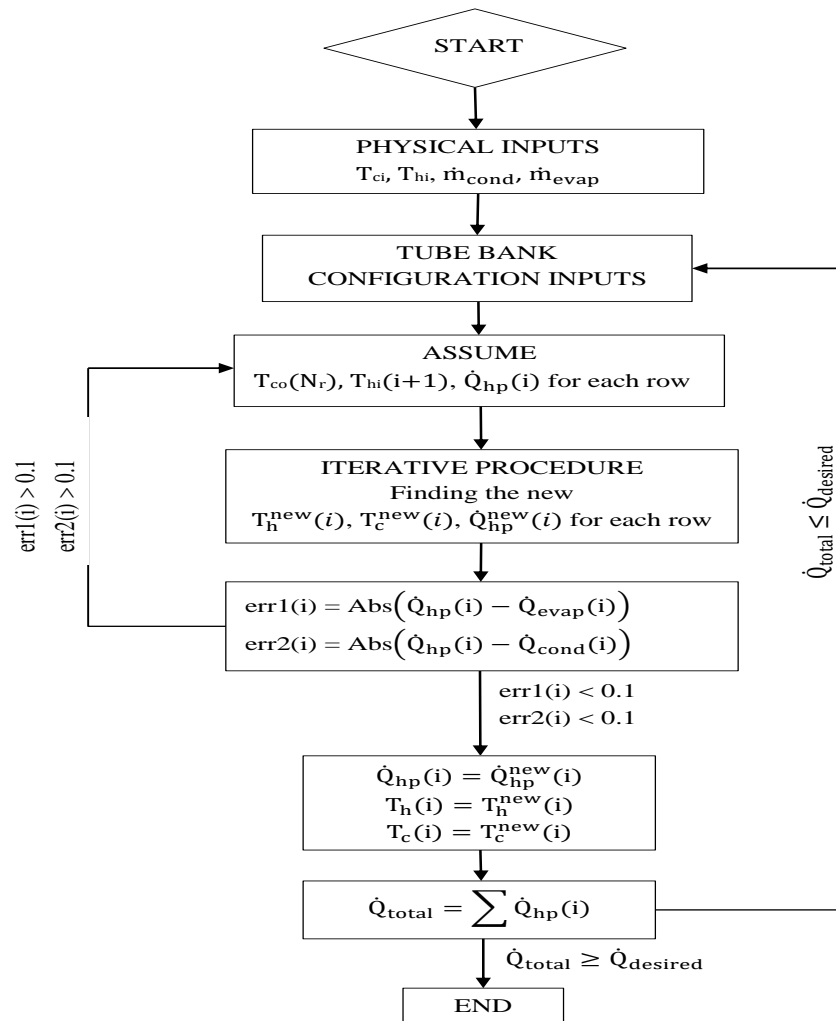


**Figure 21** Computer algorithm flow diagram

Table 4 illustrates the program output for the specified inputs

**Table 4** Program predictions

	Inlet, Outlet	Row 1-2	Row 2-3	Row 3-4	Row 4-5	Row 5-6	Outlet, Inlet
Hot Temperature [°C]	71.98	69.55	67.12	64.69	62.26	59.83	57.46
Cold Temperature [°C]	28.73	26.56	24.12	21.84	19.56	17.28	15
Total Pressure Drop [Pa]	296.33						
Total heat load [W]	12001.3						



## 5 EXPERIMENTAL WORK

This section describes the various experiments undertaken. The manufacturing, equipment and instrumentation used, calibration techniques, experimental setups and experimental procedures are all documented.

### 5.1 Manufacture of Heat Exchanger

The heat exchangers were manufactured by ColCab (Pty) Ltd and Mr G. Davids (ColCab) assisted in the design. The heat exchanger had the same specifications as given in Table 3, Section 4. The detailed heat exchanger design is shown in Appendix D.

### 5.2 Experiments

#### 5.2.1 Equipment and instrumentation used

The following equipment was used for the drying tests:

- Load cells

The *EST-2 single point compression* load cells were obtained from Technopark Control and Automation. The load cells had a capacity of 20 kg, a sensitivity of  $2 \pm 0.05$  mV/V and a hysteresis of  $\pm 0.02$  %FS

- Data acquisition system

The data was processed using the *Spider 8-600 Hz* acquisition system and the Catman Professional Suite from HBM.

- Temperature calibrator

All thermocouples were calibrated using the Fluke 9142 Field Metrology Well. The serial number is B29291.

- Temperature sensors

Type “J” temperature sensors were used to obtain the temperature at various points in the drying tests. The sensors were originally supplied by Unitemp and their part number is USAA1S-JS4UX

- Hygrometers/anemometers

*RS 327-0640* hot wire anemometers were used to measure the air flow velocity in the drier. The anemometers have a measurement range of 0.2 – 20 m/s, 0 – 50 °C, a resolution of 0.1 m/s and an accuracy of  $\pm 1$  % of the full scale. The part number is Q842567.

- Fans

The fans were supplied by *AMS and are 220-240 V, 50-60 Hz single phase, A-Series external rotor shaded pole type*. Their serial numbers are A15055.

- Temperature control box

The *Hotrunner UNIC600-01 control box* was supplied by Unitemp and the individual controllers are *Gefran 600* controllers with an accuracy of 0.2 %FS at an ambient temperature of 25 °C.

- Heating elements

The heating elements are *Incoloy Heating elements* and were also supplied by Unitemp. Their serial number is UHR-100-08080-500

The heat exchanger pressure drop, inside and outside heat transfer coefficients were experimentally determined and the following equipment was used for this.

- Wind tunnel fan

The air is drawn through the wind tunnel by a *Donkin Manufacturing Co. (Pty) Ltd.* Fan. The serial number is C1194.

- Variable Speed Drive

A *Yaskawa Varispeed E7* variable speed drive was used to vary the air velocity through the wind tunnel. Its serial number is E7C4022.

- Hot water supply tank

The 1800 L supply tank was heated by the *Hall Thermotank* boiler. The serial number is 1000022.

- Manometer

The pressure transducers were calibrated using the Van Essen BETZ Micromanometer. The range of the micrometer is 500 mm water and it has a 220 VAC power supply. Its serial number is 12563.

- Data logger

The *Agilent 34970A* DAS was used to scan the data. The part number is 380114.

- Radiator

A *Toyota Smiths* radiator was used to heat the incoming air. Its serial number is 16400-OD450-2133-3204-01.

- Pressure transducers

The pressure transducers were used to measure the pressure loss across the heat exchanger and the nozzle located in the wind tunnel. The serial numbers are USAA6S-JS4HX

### 5.2.2 Calibration techniques

The load cells were calibrated by placing known masses onto them in increasing and decreasing order. Three separate calibrations were conducted on separate days. These are displayed in Figure 22.

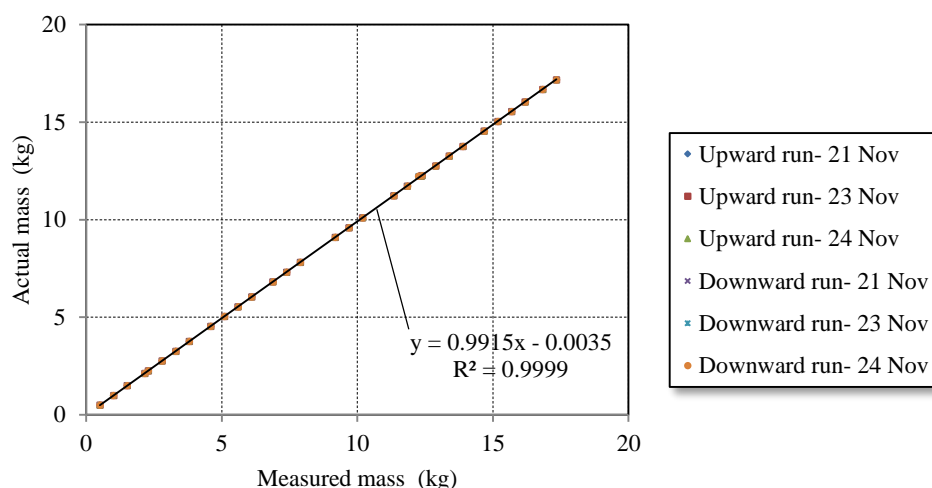


**Figure 22** Load cell calibration

All measured data was then adjusted by the calibration equation

$$m_{actual} = 0.9915m_{measured} - 0.0035 \quad (5.1)$$

The thermocouples used in the experiments were calibrated by inserting them into the metrology well and measuring their temperature using the Agilent Data Logger. The temperatures were then changed by an incremental value and from this a calibration curve for each thermocouple was created. An example is shown below.

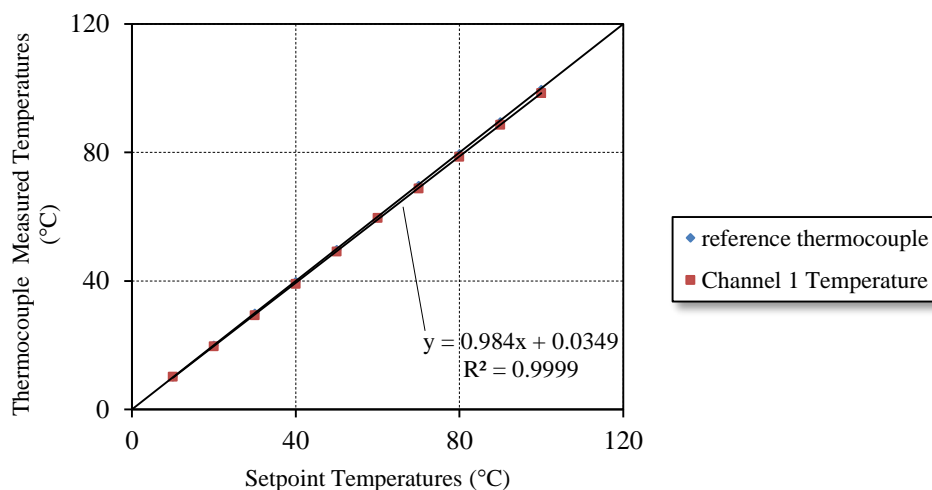


**Figure 23** Thermocouple calibration

Each thermocouple measurement was adjusted according to the equation obtained from the calibration similar to the load cell calibration.

### 5.2.3 Experimental setups

#### *Drying tests*

The drying tests were conducted in a 1.5 m long, 1 m high custom built drier that has a drying chamber size of 0.5 m × 0.43 m × 0.25 m. The drying chamber has three trays at separate heights. Only a single tray was used for the measurement of the material mass. The trays mounting was redesigned so that it would rest on a platform attached to the 20 kg load cells. Access to the trays is obtained by a small door in the front of the drier. The drier setup is shown in Figure 24.

The TCU measures temperatures at the positions illustrated by the  $T_i$  markers in Figure 24. This is then used to control the heating input to the cold airstream and as such maintain the drying chamber temperature. The VSC allows air to flow at different velocities. The mass of the product was measured via the load cells by the Spider DAS at a sampling rate of 1 Hz and the data saved to the data logger.

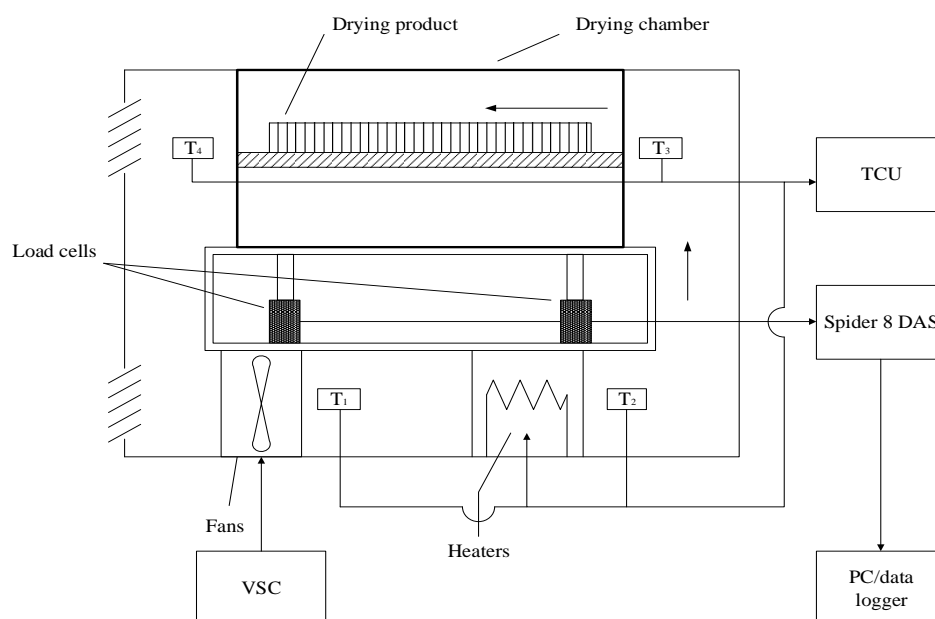


**Figure 24** Drying test setup

### ***Outside heat transfer coefficients***

To determine the outside heat transfer coefficients, a heat exchanger of similar geometry to the separated-HPHE was filled with water from the 2400 L cold water supply tank. The cold water inlet temperature was kept constant by passing it through a chiller in the supply line which cooled the water to 5 °C. To supply a suitable heat input, the radiator was supplied with hot water from the 1800 L supply tank. The hot water supply was limited to 80 °C, which limited the correlations to the temperature range of 10 °C – 80 °C. Figure 25 illustrates the water supply line to the experiment setup.

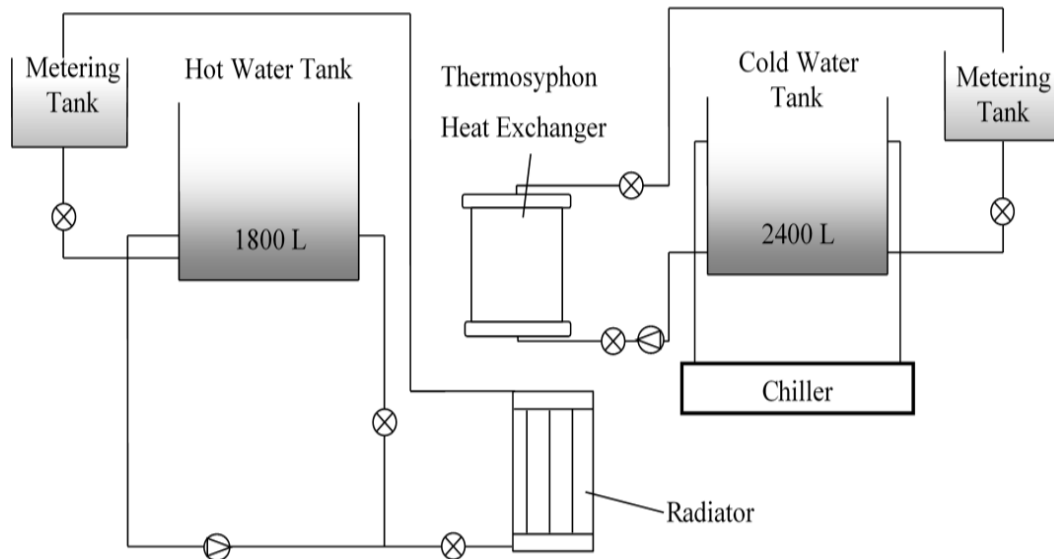


**Figure 25** Cooling and heating water tank systems

The temperature measurements points for the determination of the outside  $h$ -values are illustrated in Figure 63. The figure also illustrates the wooden duct that the heat exchanger is installed in and the wind tunnel it is attached to. The measurements are as follows:

$T_{wi}$  Hot water inlet temperature to the radiator

$T_{wo}$  Hot water outlet temperature from radiator

$T_{hpwi}$  Cold water inlet to thermosyphon-HE

$T_{hpwo}$  Cold water outlet from thermosyphon-HE

$T_{ri}$  Air inlet temperature to radiator

$T_{hei}$  Air inlet temperature to heat exchanger

$T_{heo}$  Air outlet temperature from heat exchanger

$P_{heo}$  Air pressure after heat exchanger

$P_{hei}$  Air pressure before heat exchanger

$P_{a1}$  Air pressure before nozzle

$P_{a2}$  Air pressure after nozzle

To minimise inlet losses and to ensure the air flow in the duct is of a uniform profile, the inlet is a shaped bellmouth. The air flow is determined by measuring the pressure drop across the elliptical nozzles between the perforated plates in the wind tunnel. The corresponding mass flow rate is given by

$$\dot{m}_{air} = C_n \phi_g Y A_n (2p_{up} \Delta p_n)^{0.5} \quad (5.2)$$

For very low Reynolds numbers the nozzle discharge coefficient is at least 0.97, which is close to unity and for simplification can be assumed to be unity. The gas expansion factor and the approach velocity factor can be given as follows:

$$\phi_g = 1 - 3\Delta p_n / (4p_{up}c_p/c_v) \quad (5.3)$$

$$Y = 1 + 0.5(A_n/A_{tun})^2 + 2(A_n/A_{tun})^2\Delta p_n / (p_{up}c_p/c_v) \quad (5.4)$$

where for air  $c_p/c_v = 1.4$ , the diameter of the nozzle = 0.23 m, the upstream pressure is known and the area of the tunnel,  $A_{tun} = 1.43 \text{ m} \times 1.28 \text{ m} = 1.83 \text{ m}^2$ . The outside heat transfer coefficient setup is shown Figures 25 and 65.

### *Inside heat transfer coefficients and thermal performance*

The separated-HPHE was installed into the modified wooden tunnel duct and wind tunnel system as shown in Figures 27 and 64. As depicted in the figures, the evaporator was placed below the condenser section and the sections were connected by the vapour riser and liquid down comer tubes. To obtain the heat input to the evaporator, the condenser preheats the inlet air and the radiator heats the air to the desired evaporator inlet temperature. Thus the setup represents two different fluid streams. The cold water supply was not used for this set of experiments. The thermosyphon loops were filled to 50 % of the evaporator length. To measure the inside temperatures of the individual rows, thermocouples were attached to the walls of the riser and the down comer tubes. The thermal resistance of the copper walls are negligible, thus the inside temperature can be estimated by measuring the wall temperature.

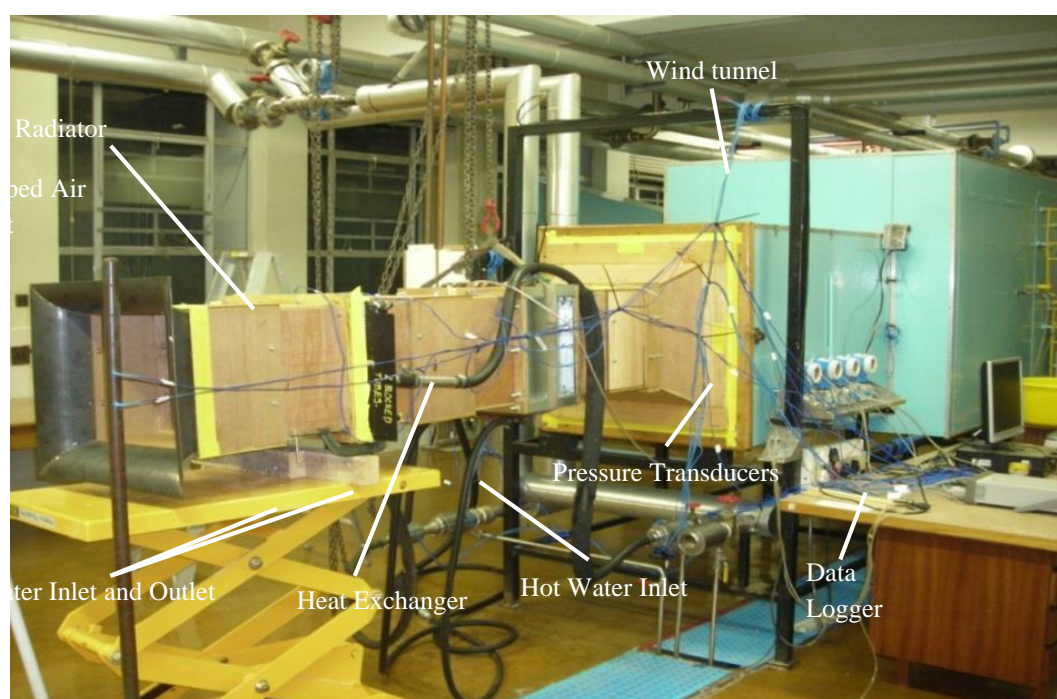


**Figure 26** Experimental setup for determining the outside heat transfer coefficient

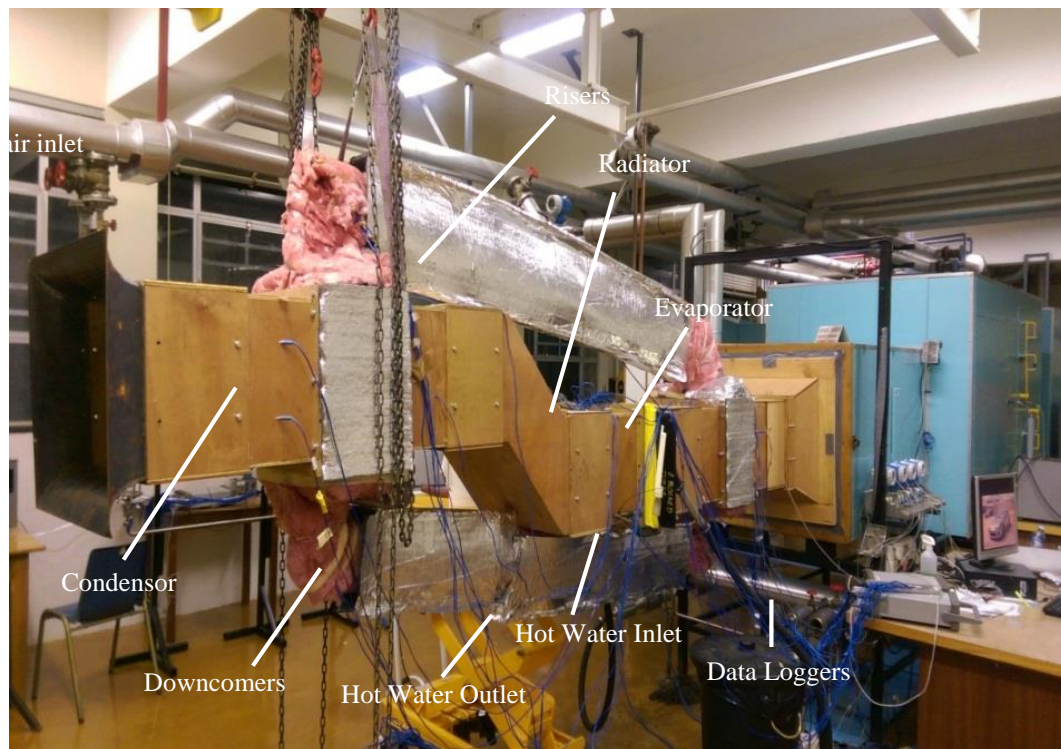


**Figure 27** Experimental setup for determining the inside heat transfer coefficient

For the separated-HPHE to operate effectively and to prevent refrigerant leakage, each thermosyphon loop needs to be vacuum tight. The thermosyphon loops were charged by using a single stage vacuum pump and a scale. The charging procedure is as follows:

- The thermosyphons loops respective volumes were calculated and from this an exact amount of refrigerant was calculated in kilograms
- The air in the thermosyphon loop is pumped out and the loop is checked for being vacuum tight.
- The loop is checked that it holds a vacuum for at least 5 mins.
- The pressurized bottle holding the refrigerant is heated by inserting it in a hot water bath to cause a higher pressure in the bottle than in the loop and allow the refrigerant to flow into the loop through the Schrader valve
- The mass of the pressurized bottle is measured by the scale as the refrigerant flows into the loop
- When the appropriate amount of refrigerant has flowed into the loop, the bottle is closed off. The loop is then “burped” to allow trace amounts of air to escape
- The bottle and vacuum pump are disconnected and the process is repeated for the next loop

The charging setup is illustrated in Figure 28.

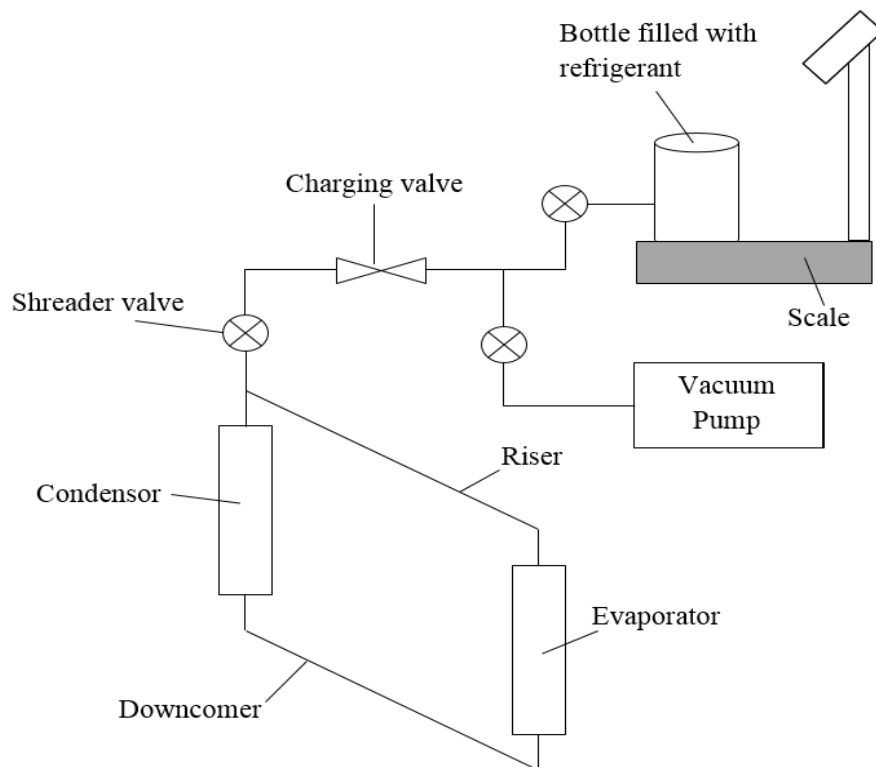


**Figure 28** Thermosyphon loop charging setup

#### 5.2.4 Experimental procedures

The typical experimental procedures were as follows:

##### *Drying tests*

- i) Set the drying element temperature to the desired drying temperature and allow drier to warm-up
- ii) Load the drying tray and set the load cell measured values to zero
- iii) Set the VSC to the lowest flowrate position to turn on the fans
- iv) Measure the mass of the tray as the product loses moisture
- v) Measure the air mass flow rate and temperature to ensure drying conditions stay constant
- vi) Once the material is dried, remove the material, adjust the air flow rate and allow drying conditions to stabilise
- vii) Reload drying tray and repeat steps iv) to vii)

The drying temperature can then be adjusted and the experiment repeated.

##### *Outside heat transfer coefficients and pressure loss*

- i) Set the hot water inlet temperature and cold water inlet temperature to the desired values
- ii) Set the VSD of the fan at 20 Hz
- iii) Measure the hot and cold water inlet and outlet temperatures
- iv) Measure the atmospheric and heat exchanger outlet temperatures
- v) Measure the pressure loss across the heat exchanger and the wind tunnel nozzle



vi) Adjust the VSD to a higher frequency and repeat steps iii) to vi)

A test run at the specific hot water temperature is then complete. A new hot water temperature can be selected and allowed to stabilise at the new selected value. The procedure can then be repeated.

***Inside heat transfer coefficients and thermal performance***

- Set the hot water inlet temperature to the desired value
- Set the VSD of the fan to 20 Hz
- Measure the air temperatures at the inlet and outlet of the condenser, radiator and evaporator
- Measure the temperatures of the refrigerant of all the rows at the top and bottom of the condenser and evaporator
- Adjust the VSD to a higher frequency and repeat steps iii) to v)

The procedure can then be repeated at a different hot water temperature similar to the outside heat transfer coefficients.

## 6 RESULTS

This section documents the results of all the experimental work done. Where needed, the results are compared to theoretical results for validation purposes. The results obtained are split into

- Thermal performance of a separated-HPHRHE – pressure loss, outside heat transfer characteristics and multi-linear regression
- Thermal performance of a separated-HPHRHE – energy balances, inside heat transfer characteristics and multi-linear regression
- Inside temperature distribution of the separated-HPHRHE
- Comparison of the heat exchanger performance with numerical program predictions and theoretical correlations

For ease of reading the multi-linear equations are lumped together before or after the applicable figures.

### 6.1 Thermal Performance of the Separated-HPHRHE

A large number of data points was generated by each experiment. These data points were reduced to a data set of 90 points. To illustrate that the heat exchanger is working properly and that the thermocouples are indeed measuring the correct temperatures, the energy balance between the evaporator and condenser sections must lie within a small percentage of each other.

This subsection describes the predicted results obtained from applying multi-linear regression techniques on the generated data sets. While it is theoretically possible to use a large amount of variables to accurately predict the desired property, for practical applications this can be time consuming and complex. Thus, only a maximum of two variables with the largest influence were chosen to model the desired properties. Sample calculations are given in Appendices A4 and A5.

#### 6.1.1 Outside heat transfer coefficients and pressure loss

Figure 29 illustrates the energy balance obtained while testing a heat exchanger that was geometrically the same as the units used for the separated-HPHE setup. The conservation of energy is deemed satisfactory and thus the obtained results can be used with confidence.

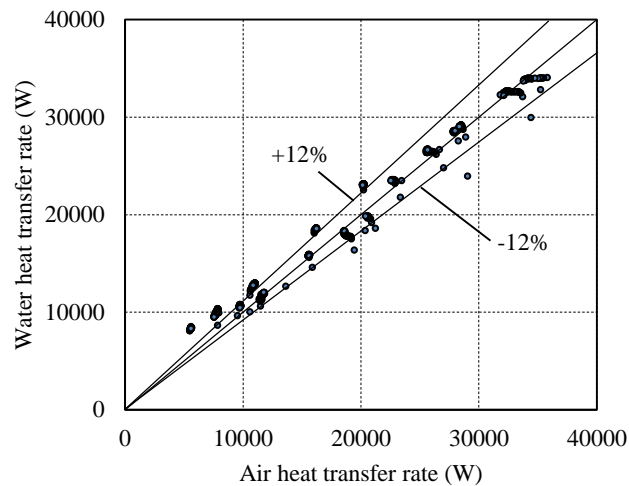


**Figure 29** Energy balance of the geometrically similar heat exchanger

For these experiments the heat fluxes typically ranged from  $7000 \text{ W/m}^2$  –  $30000 \text{ W/m}^2$ , the air mass flow rates ranged from  $0.36 \text{ kg/s}$  –  $1.2 \text{ kg/s}$  and the maximum heat transfer rate reached a value of  $34802 \text{ W}$  with an average temperature difference of  $27.2 \text{ }^\circ\text{C}$  across the entire heat exchanger. When calculating the outside heat transfer coefficients for each row, it was assumed that the temperature profile of both the water and the air across the heat exchanger vary linearly. Sample calculations are shown in Appendix A4

Figure 30 a) through f) illustrates the predicted outside heat transfer coefficients compared to the experimentally obtained outside heat transfer coefficients for each individual row. Figure 30 a) and b) show that all of the predicted values fall within 5 % of the experimental values for the first two rows. Figure 30 c) and d) show that for rows three and four 98 % of the predicted values fall within 8 % and 10 % respectively. The final two rows, as indicated by Figure 30 e) and f), are slightly less reliable. For the fifth row 89 % of the values lie within 11 % of the experimental values, while for the sixth row, 80 % of the values lie within 15 % of the experimental values.

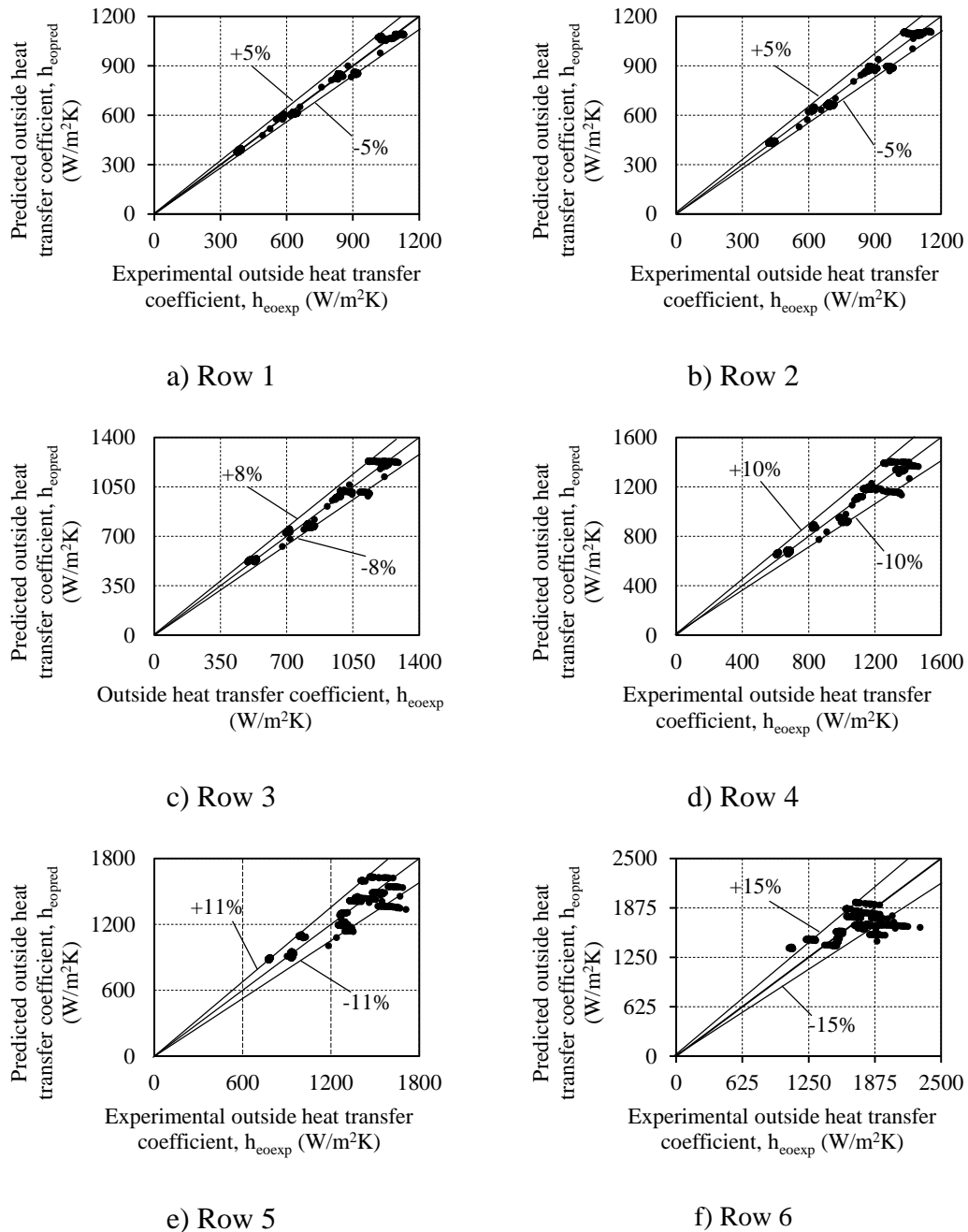


**Figure 30** Outside heat transfer coefficients for each row of the geometrically similar heat exchanger filled with cold water

To do a regression analysis, all the possible variables were considered and refined as needed. These are listed below:

$$h_{eo} = f(Re_{air}, Pr_{air}, d_o, S_T, S_L, \dots) \quad (6.1)$$

Only dimensionless number should be used in the correlations. The Reynolds number documents the air mass flowrate and geometric properties of the heat exchanger while the Prandtl number encompasses the air temperature and thus these two variables were used in the multi-linear regression. It was also noted that even the addition of several more variables provided a very small improvement

in accuracy. Thus only these two variables were considered. The outside heat transfer coefficients for each row were determined by as follows:

$$\text{Row 1: } h_{eo} = 0.00112 Re_{air}^{0.9355} Pr_{air}^{-7.5615} \quad R^2 = 0.9947 \quad (6.2)$$

$$\text{Row 2: } h_{eo} = 0.00254 Re_{air}^{0.8391} Pr_{air}^{-8.5795} \quad R^2 = 0.9884 \quad (6.3)$$

$$\text{Row 3: } h_{eo} = 0.00469 Re_{air}^{0.7580} Pr_{air}^{-9.9140} \quad R^2 = 0.9773 \quad (6.4)$$

$$\text{Row 4: } h_{eo} = 0.00896 Re_{air}^{0.6424} Pr_{air}^{-12.4014} \quad R^2 = 0.9491 \quad (6.5)$$

$$\text{Row 5: } h_{eo} = 0.0168 Re_{air}^{0.4627} Pr_{air}^{-17.2343} \quad R^2 = 0.9947 \quad (6.6)$$

$$\text{Row 6: } h_{eo} = 0.0364 Re_{air}^{0.1443} Pr_{air}^{-26.603} \quad R^2 = 0.3882 \quad (6.7)$$

Figure 30 shows that 92 % of the predicted pressure loss values fall within 8 % of their experimental counterparts.

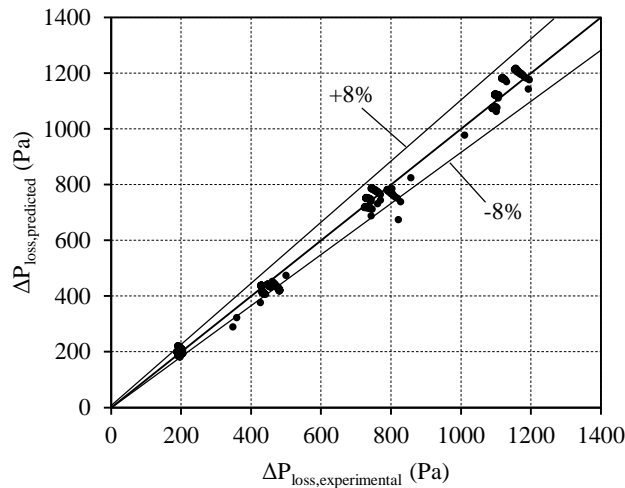


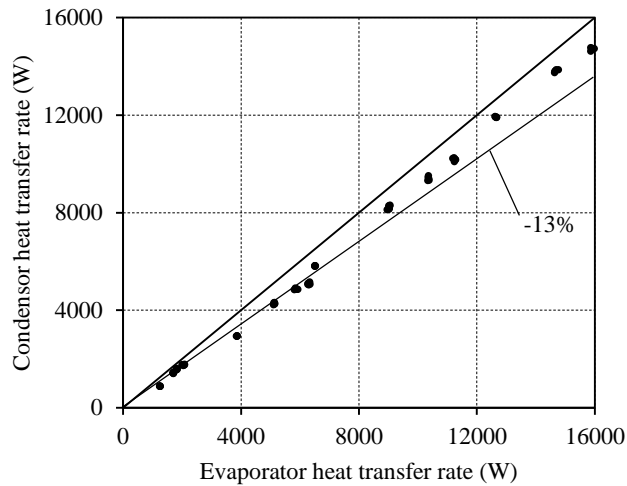
**Figure 31** Pressure loss across the HPHE

Similar to the outside heat transfer coefficients, the pressure loss is also given in terms of the air side Reynolds and Prandtl numbers. The obtained correlation is given below:

$$\Delta P_{loss,pred} = 1.2104 \times 10^{-6} Re_{air}^{1.5828} Pr_{air}^{-5.1585} \quad R^2 = 0.972 \quad (6.8)$$

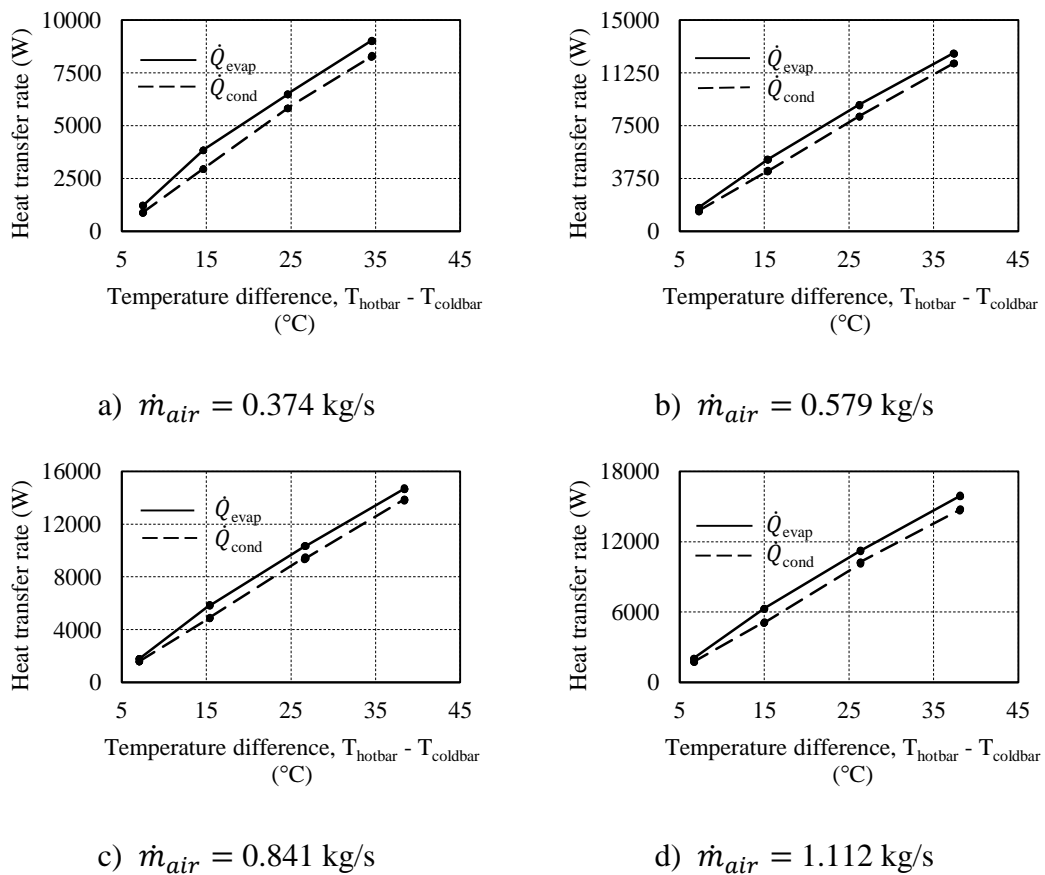
### 6.1.2 Inside heat transfer coefficients: R600a

Figure 32 illustrates that for the separated-HPHE configuration using R600a as the refrigerant, the evaporator heat transfer values are up to 13 % higher than the condenser heat transfer values. This is deemed acceptable because in a practical application, no WHRU can recover all the heat input and the values are within reason. For this set of experiments, the heat fluxes ranged from 1086 W/m<sup>2</sup> to 13825 W/m<sup>2</sup> and the maximum heat transfer rate obtained 15968 W at an average temperature difference of 38 °C.



**Figure 32** Energy balance of the separated-HPHE operating with R600a

One of the objectives of this study was also to investigate which commercially obtainable refrigerant works optimally in the temperature range considered and how their performance is influenced by the differences in temperature between the condenser and evaporator section. Figure 33 a) to d) illustrate that R600 works effectively with a relatively small temperature difference required between the evaporator and condenser sections.



**Figure 33** The thermal resistance of the separated-HPHE charged with R600a at different mass flow rates

Figure 34 illustrates the predicted inside heat transfer coefficients compared to the experimental heat transfer coefficients for the first three rows. Figure 34 a) and b) show that the 95 % of the predicted values fall within 16 % of the experimental values. For row 2, the 95 % of the predicted values fall within 20 % and 16 % for the evaporator and condenser respectively. The third rows' scatter is a slightly less accurate, with 90 % of the values falling within 30 % for the evaporator and 95 % of the values falling within 25 % for the condenser.

The comparison between the predicted inside heat transfer coefficient and the experimentally obtained heat transfer coefficient are shown in Figure 35 a) through f). For row 4, 95 % of the predicted values fall within 20 % and 22 % of the experimental values for the evaporator and condenser sections respectively. The evaporator section in row 5 has 95 % of its values inside 22 % of the reference line, while the condenser section has its values all within 10 % of the reference line. For the evaporator section in row 6, 93 % of the predicted values fall within 12 % within of the experimentally obtained values, while for the condenser section 20 % of the predicted values fall within 20 % of the experimental values. The equations obtained from the regression analysis are given as follows:

#### Evaporator

$$\text{Row 1: } 1426.3589Ku^{0.2613}Ja^{-0.1752} \quad R^2 = 0.1662 \quad (6.9)$$

$$\text{Row 2: } 4776.64Ku^{-0.5639}Ja^{0.5721} \quad R^2 = 0.2641 \quad (6.10)$$

$$\text{Row 3: } 2429.974Ku^{-0.4144}Ja^{0.1822} \quad R^2 = 0.3983 \quad (6.11)$$

$$\text{Row 4: } 2611.49Ku^{-0.3609}Ja^{0.1551} \quad R^2 = 0.5575 \quad (6.12)$$

$$\text{Row 5: } 362.505Ku^{0.8386}Ja^{-0.903} \quad R^2 = 0.5318 \quad (6.13)$$

$$\text{Row 6: } 61.2557Ku^{1.7316}Ja^{-1.6903} \quad R^2 = 0.7651 \quad (6.14)$$

#### Condenser

$$\text{Row 1: } 9.415Re^{0.9234}\left(\frac{\rho_v}{\rho_l}\right)^{1.0052} \quad R^2 = 0.9824 \quad (6.15)$$

$$\text{Row 2: } 1.4252Re^{1.0690}\left(\frac{\rho_v}{\rho_l}\right)^{1.4842} \quad R^2 = 0.9538 \quad (6.16)$$

$$\text{Row 3: } 1097.46Re^{0.7618}\left(\frac{\rho_v}{\rho_l}\right)^{-0.1254} \quad R^2 = 0.9194 \quad (6.17)$$

$$\text{Row 4: } 1001.2499Re^{0.7152}\left(\frac{\rho_v}{\rho_l}\right)^{-0.1175} \quad R^2 = 0.9172 \quad (6.18)$$

$$\text{Row 5: } 68.246Re^{1.0008}\left(\frac{\rho_v}{\rho_l}\right)^{0.4186} \quad R^2 = 0.9999 \quad (6.19)$$

$$\text{Row 6: } 14370.66Re^{0.4792}\left(\frac{\rho_v}{\rho_l}\right)^{-0.8017} \quad R^2 = 0.9625 \quad (6.20)$$

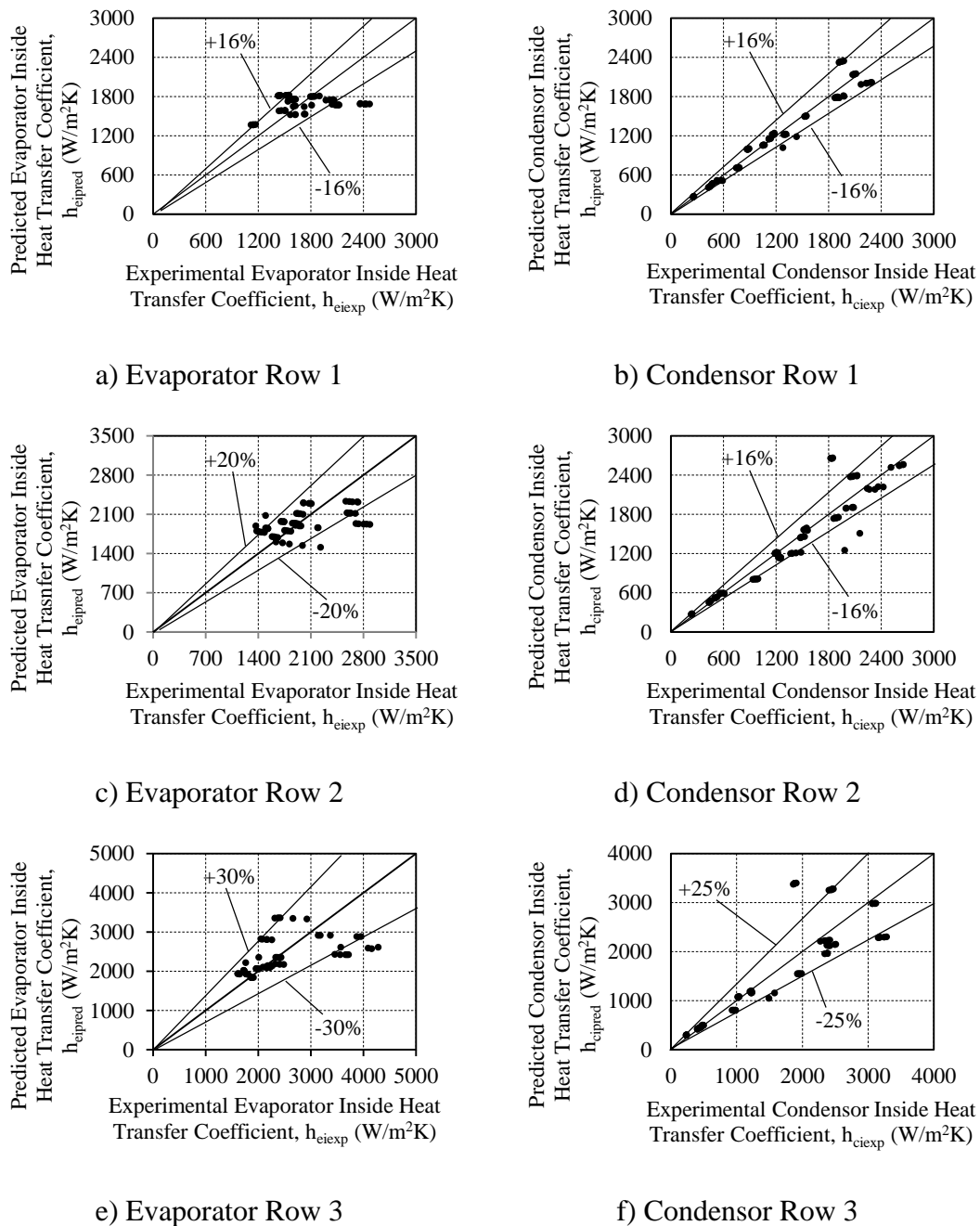


**Figure 34** Inside heat transfer coefficients for the separated-HPHE operating with R600a and charged to 50 % of the evaporator length for Row 1-3



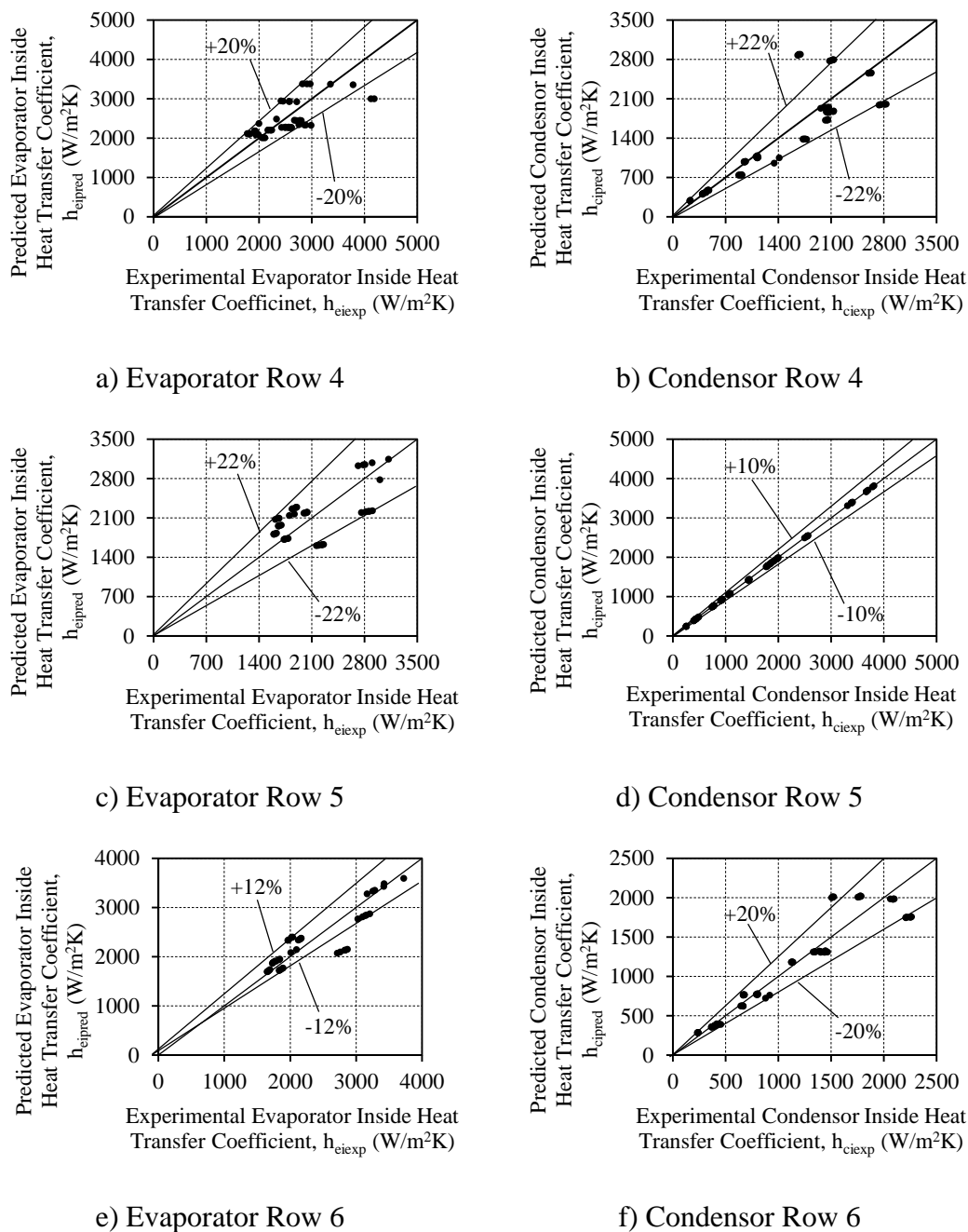
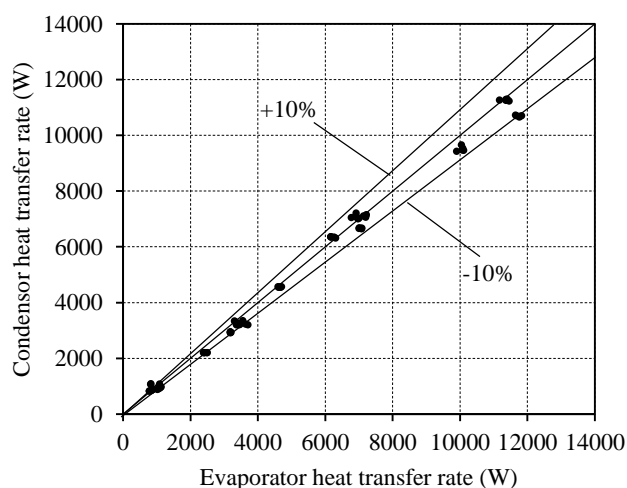


**Figure 35** Inside heat transfer coefficients for the separated-HPHE operating with R600a and charged to 50 % of the evaporator length for Row 4-6

It is observed that the inside condenser heat transfer coefficients display much more scatter than the evaporator inside heat transfer coefficient, which are mostly scattered around a constant value.

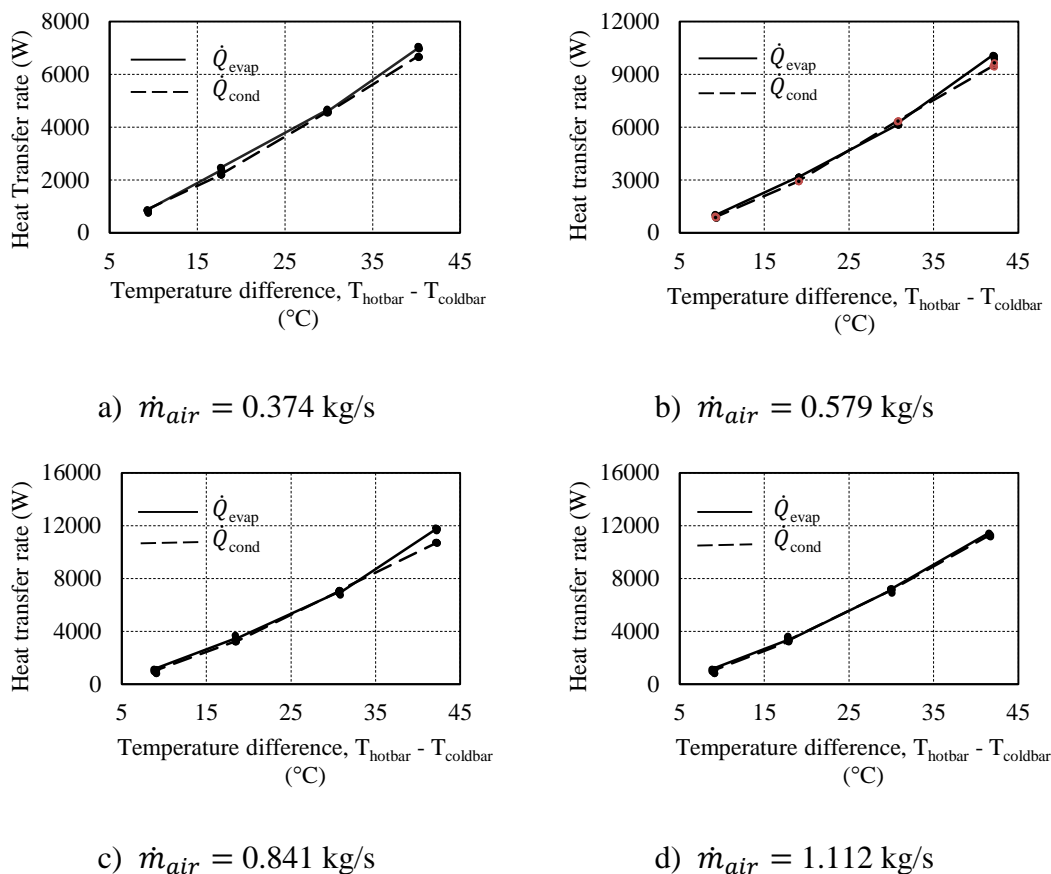
### 6.1.3 Inside heat transfer coefficients: R134a

Figure 36 displays the energy balance for the separated-HPHE with R134a as the refrigerant. The evaporator and condenser heat transfer rate values lie within 10 % of each other. This was deemed satisfactory for results to be obtained. The heat fluxes for the experiments ranged from  $704 \text{ W/m}^2$  –  $9694 \text{ W/m}^2$  and the maximum heat transfer rate was obtained as  $11763 \text{ W}$  at a temperature difference of  $40 \text{ }^\circ\text{C}$ .



**Figure 36** Energy balance of the separated-HPHE operating with R134a

The effectiveness as a function of the average evaporator and condenser temperature difference is illustrated in Figure 37 a) through d). It can be seen that R134a also works well for low temperature differences, as was the case with R600a.



**Figure 37** The effectiveness of the separated-HPHE charged with R134a at different mass flow rates

Figure 38 shows the predicted inside heat transfer coefficients compared to the experimentally obtained inside heat transfer coefficients. Figure 38 a) and b) indicate that 90 % of the predicted inside heat transfer coefficients fall within 35 % and 10 % for the evaporator and the condenser sections respectively. For both rows 2 and 3, 85 % of the predicted values fall within 16 % for the evaporator sections while for both of the condenser sections the all of the predicted values lie within 12 % of the experimental values. These are shown in Figure 38 c) through f).

Figure 39 shows the comparison between the predicted inside heat transfer coefficients and the experimentally obtained inside heat transfer coefficients. For row 4, 95 % of the predicted values fall within 16 % of the reference line value for the evaporator while all of the predicted values fall within 16 % for the condenser. For row 5, 95 % of the predicted values fall within 14 % and 16 % of the experimentally obtained values as depicted in Figure 39 c) and d). For row 6, the predicted values fall within 8 % of the experimental values for the evaporator and 92 % of the predicted values fall within 13 % of the experimentally obtained values. The correlations that were obtained are listed as follow:

Evaporator

$$\text{Row 1: } 6350.69Ku^{-1.8245}Ja^{1.9944} \quad R^2 = 0.5486 \quad (6.21)$$

$$\text{Row 2: } 509.276Ku^{0.194}Ja^{-0.268} \quad R^2 = 0.2368 \quad (6.22)$$

$$\text{Row 3: } 1085.759Ku^{0.0186}Ja^{0.0764} \quad R^2 = 0.09502 \quad (6.23)$$

$$\text{Row 4: } 479.191Ku^{0.6914}Ja^{-0.5742} \quad R^2 = 0.6541 \quad (6.24)$$

$$\text{Row 5: } 210.364Ku^{1.0891}Ja^{-1.1367} \quad R^2 = 0.6928 \quad (6.25)$$

$$\text{Row 6: } 120.069Ku^{1.4954}Ja^{-1.5067} \quad R^2 = 0.9657 \quad (6.26)$$

Condenser

$$\text{Row 1: } 1.9983Re^{0.7899}(\rho_v/\rho_l)^{1.3760} \quad R^2 = 0.9732 \quad (6.27)$$

$$\text{Row 2: } 7577.68Re^{0.0581}(\rho_v/\rho_l)^{-1.0347} \quad R^2 = 0.9789 \quad (6.28)$$

$$\text{Row 3: } 5.0257Re^{0.7546}(\rho_v/\rho_l)^{1.1263} \quad R^2 = 0.9787 \quad (6.29)$$

$$\text{Row 4: } 101.0105Re^{0.6669}(\rho_v/\rho_l)^{0.2727} \quad R^2 = 0.9718 \quad (6.30)$$

$$\text{Row 5: } 5402.1391Re^{0.606}(\rho_v/\rho_l)^{-0.95146} \quad R^2 = 0.9797 \quad (6.31)$$

$$\text{Row 6: } 118903.04Re^{0.5162}(\rho_v/\rho_l)^{-1.8732} \quad R^2 = 0.9683 \quad (6.32)$$

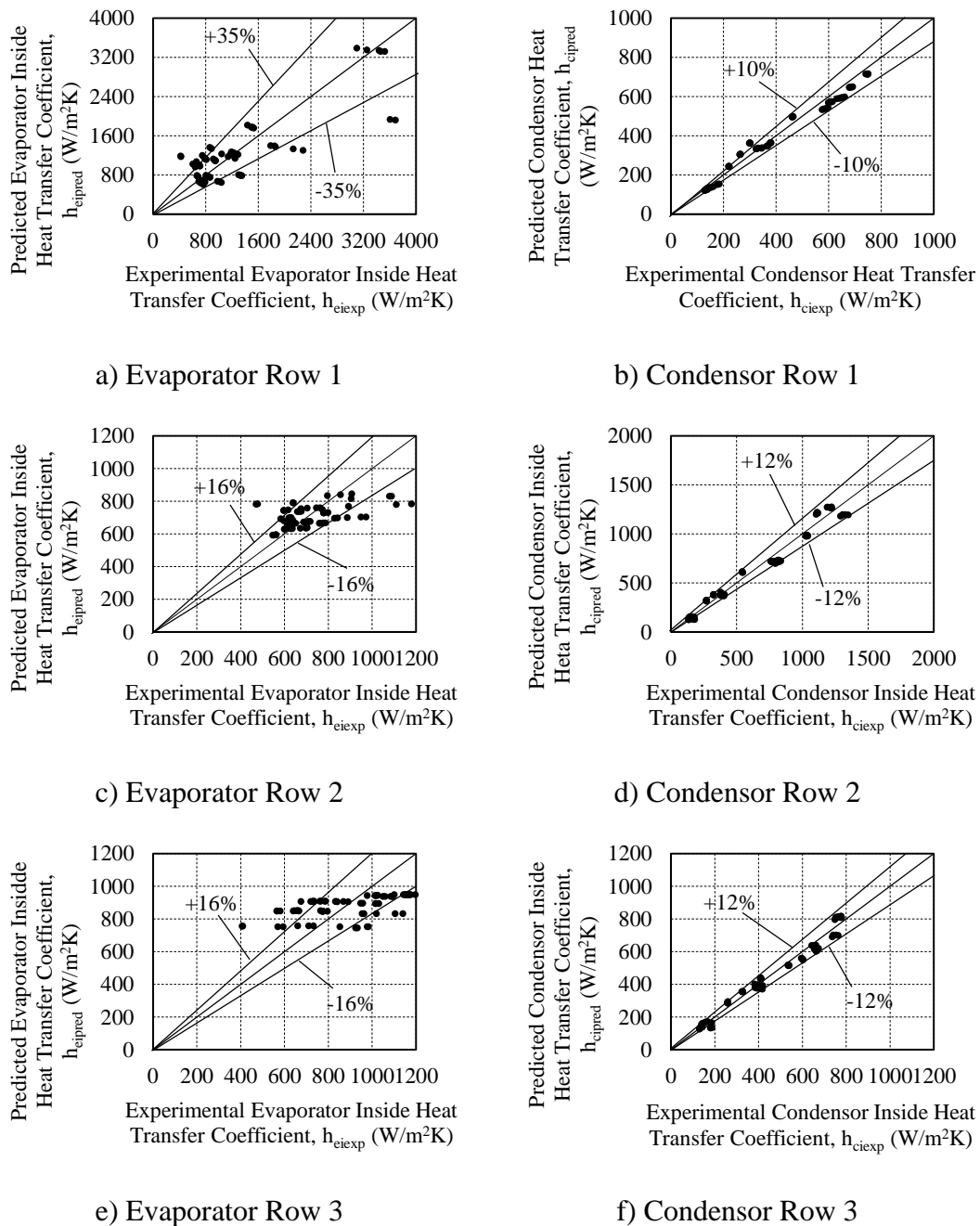
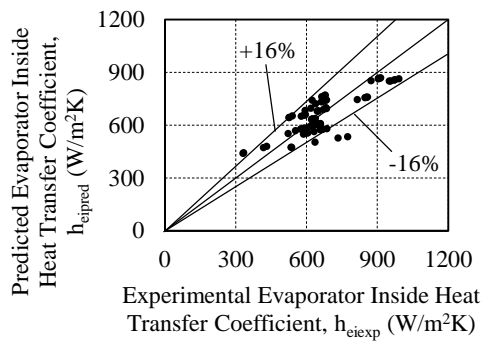
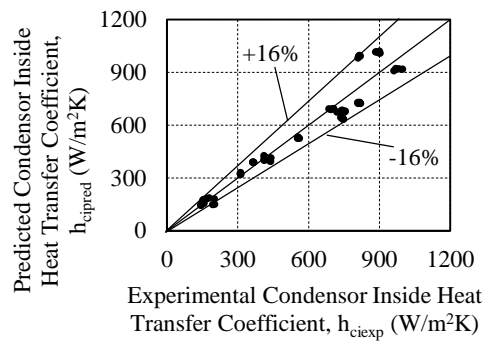


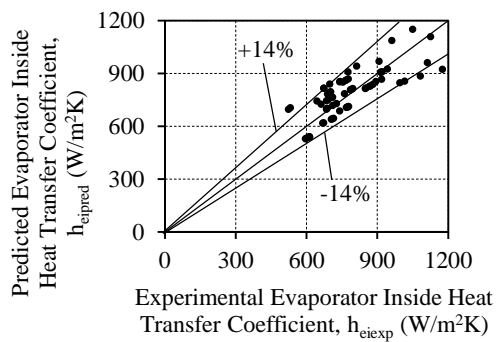
**Figure 38** Inside heat transfer coefficients for the separated-HPHE operating with R134a and charged to 50 % of the evaporator length for Row 1-3



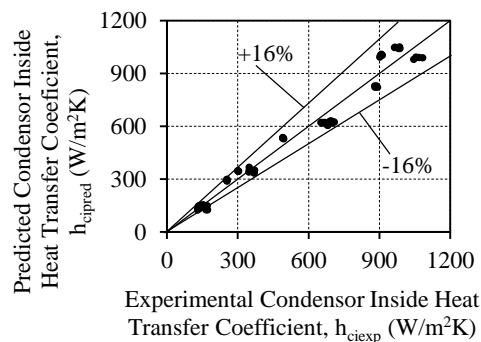
a) Evaporator Row 4



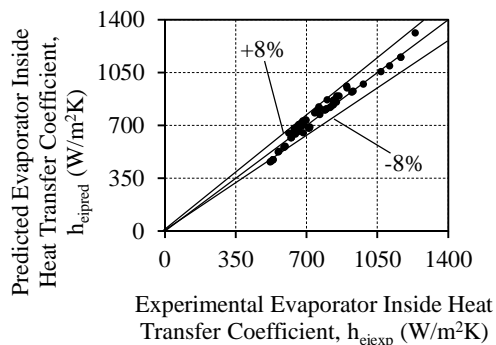
b) Condenser Row 4



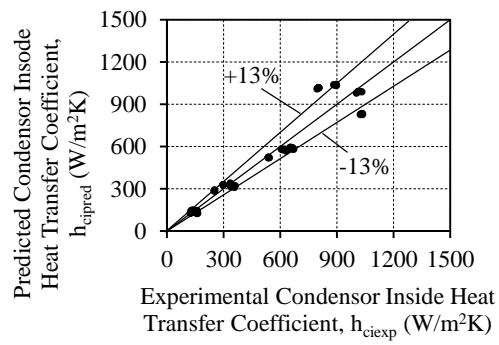
c) Evaporator Row 5



d) Condenser Row 5



e) Evaporator Row 6

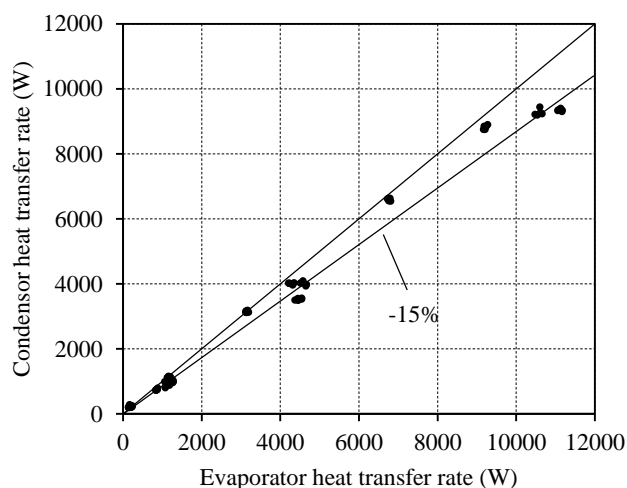


f) Condenser Row 6

**Figure 39** Inside heat transfer coefficients for the separated-HPHE operating with R134a and charged to 50 % of the evaporator length for Row 4-6

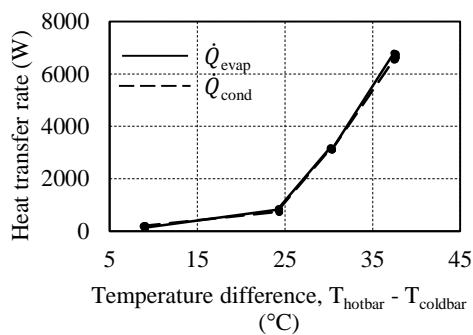
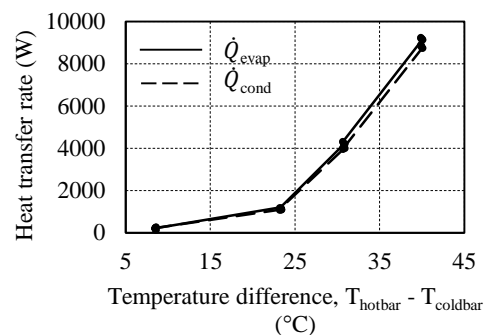
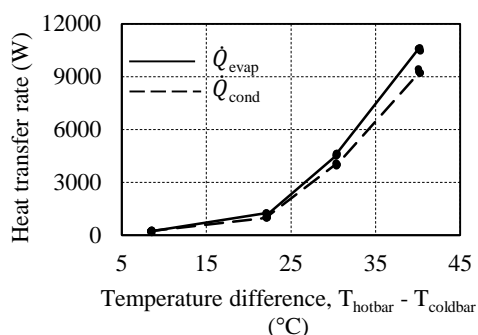
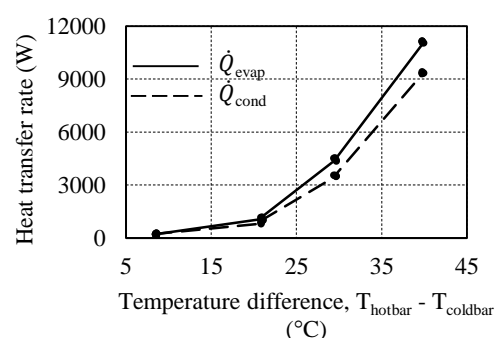
#### 6.1.4 Inside heat transfer coefficients: R123

Figure 40 shows the energy balance of the separated-HPHE using R123 as the refrigerant. The evaporator and condenser heat transfer rates fall within 15 % of each other, which is satisfactory.



**Figure 40** Energy balance of the separated-HPHE operating with R123

The effectiveness of R123 as a function of temperature difference is given in Figure 41 a) through d). Here it can be seen that R123 only starts working effectively from larger temperature differences of approximately 20 °C. However, as the temperature difference rises, the change in heat transfer capabilities increases more sharply than for both R600a and R134a. It is thus clearly more suited to higher temperature differences in this application.


 a)  $\dot{m}_{air} = 0.374 \text{ kg/s}$ 

 b)  $\dot{m}_{air} = 0.579 \text{ kg/s}$ 

 c)  $\dot{m}_{air} = 0.841 \text{ kg/s}$ 

 d)  $\dot{m}_{air} = 1.112 \text{ kg/s}$ 

**Figure 41** The effectiveness of the separated-HPHE charged with R123 at different mass flow rates

Figure 42 depicts the predicted inside heat transfer coefficient compared to the experimentally obtained inside heat transfer coefficient. It can be seen from the results that only the higher temperature data sets depict proper functioning of the heat exchanger. For the first row, 90 % of the values predicted by the correlations are within 33 % and 40 % of the experimental values for the evaporator and condenser sections respectively. Row two's predictions has slightly better accuracy, but still indicate the poor low temperature performance of R123. The evaporator section predicted values fall within 25% of the experimental values. The condenser section has a scatter of approximately 37 % around the reference line. For row 3, the predicted values are scattered about the reference line by 30 % and 40 % for the evaporator and condenser respectively.

Figure 43 depicts the inside heat transfer predicted values compared to the experimentally obtained values. Figure 43 a) and b) show that the 85 % of the predicted values for row 4 of the evaporator section are within 22 % of the reference line, while 90 % of the predicted values are within 40 % of the reference line. Row five's evaporator predicted values are more acceptable and all fall within 10 % of the reference line, while the condenser scatter about the reference line is 30 %. For row 6, most of the values fall within 20 % and 35 % of the reference line. The correlations for the inside heat transfer coefficients are listed below:

Evaporator



$$\text{Row 1: } 4999.877Ku^{0.7037}Ja^{0.5643} \quad R^2 = 0.9506 \quad (6.33)$$

$$\text{Row 2: } 65424.29Ku^{0.4551}Ja^{1.4070} \quad R^2 = 0.8117 \quad (6.34)$$

$$\text{Row 3: } 1026.09Ku^{-0.257}Ja^{1.143} \quad R^2 = 0.9634 \quad (6.35)$$

$$\text{Row 4: } 557.87Ku^{1.1467}Ja^{-0.495} \quad R^2 = 0.9643 \quad (6.36)$$

$$\text{Row 5: } 212.882Ku^{1.1798}Ja^{-0.7814} \quad R^2 = 0.9837 \quad (6.37)$$

$$\text{Row 6: } 59.79Ku^{1.2298}Ja^{-1.1679} \quad R^2 = 0.9969 \quad (6.38)$$

### Condenser

$$\text{Row 1: } 1686.29Re^{0.4599}(\rho_v/\rho_l)^{-0.4783} \quad R^2 = 0.7587 \quad (6.39)$$

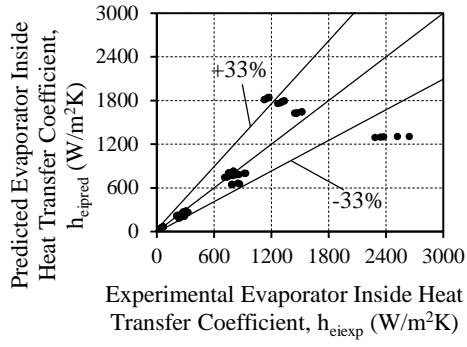
$$\text{Row 2: } 11553.34Re^{0.4096}(\rho_v/\rho_l)^{-0.8732} \quad R^2 = 0.7986 \quad (6.40)$$

$$\text{Row 3: } 19371.23Re^{0.4064}(\rho_v/\rho_l)^{-0.9597} \quad R^2 = 0.78109 \quad (6.41)$$

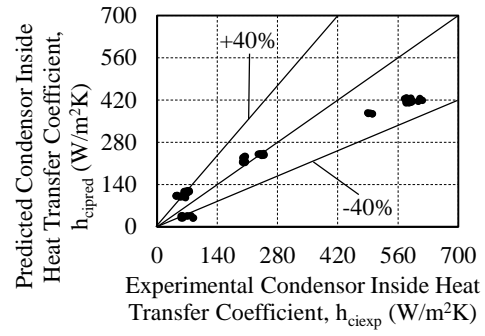
$$\text{Row 4: } 16156.89Re^{0.4333}(\rho_v/\rho_l)^{-0.9677} \quad R^2 = 0.7588 \quad (6.42)$$

$$\text{Row 5: } 56467942.58Re^{0.1712}(\rho_v/\rho_l)^{-2.4869} \quad R^2 = 0.8349 \quad (6.43)$$

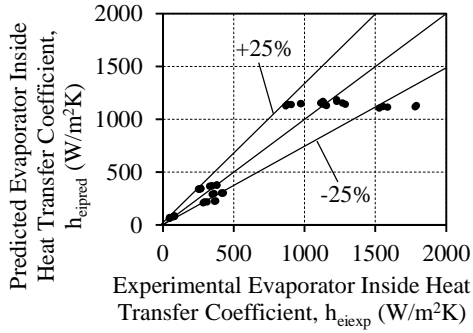
$$\text{Row 6: } 1.8785 \times 10^{17}Re^{0.9234}(\rho_v/\rho_l)^{1.0052} \quad R^2 = 0.9391 \quad (6.44)$$



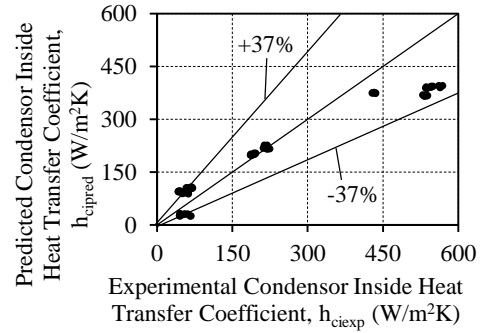
a) Evaporator Row 1



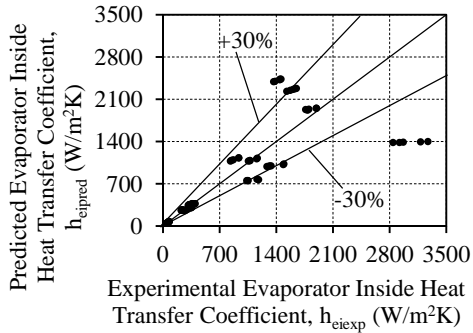
b) Condensor Row 1



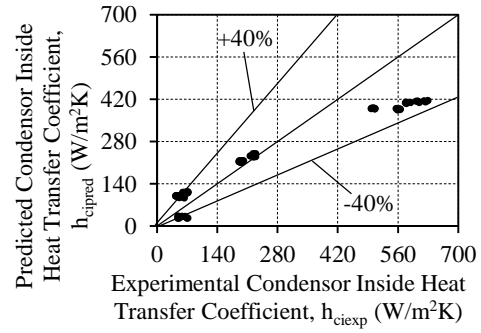
c) Evaporator Row 2



d) Condensor Row 2



e) Evaporator Row 3



f) Condensor Row 3

**Figure 42** Inside heat transfer coefficients for the separated-HPHE operating with R123 and charged to 50 % of the evaporator length for Row 1-3

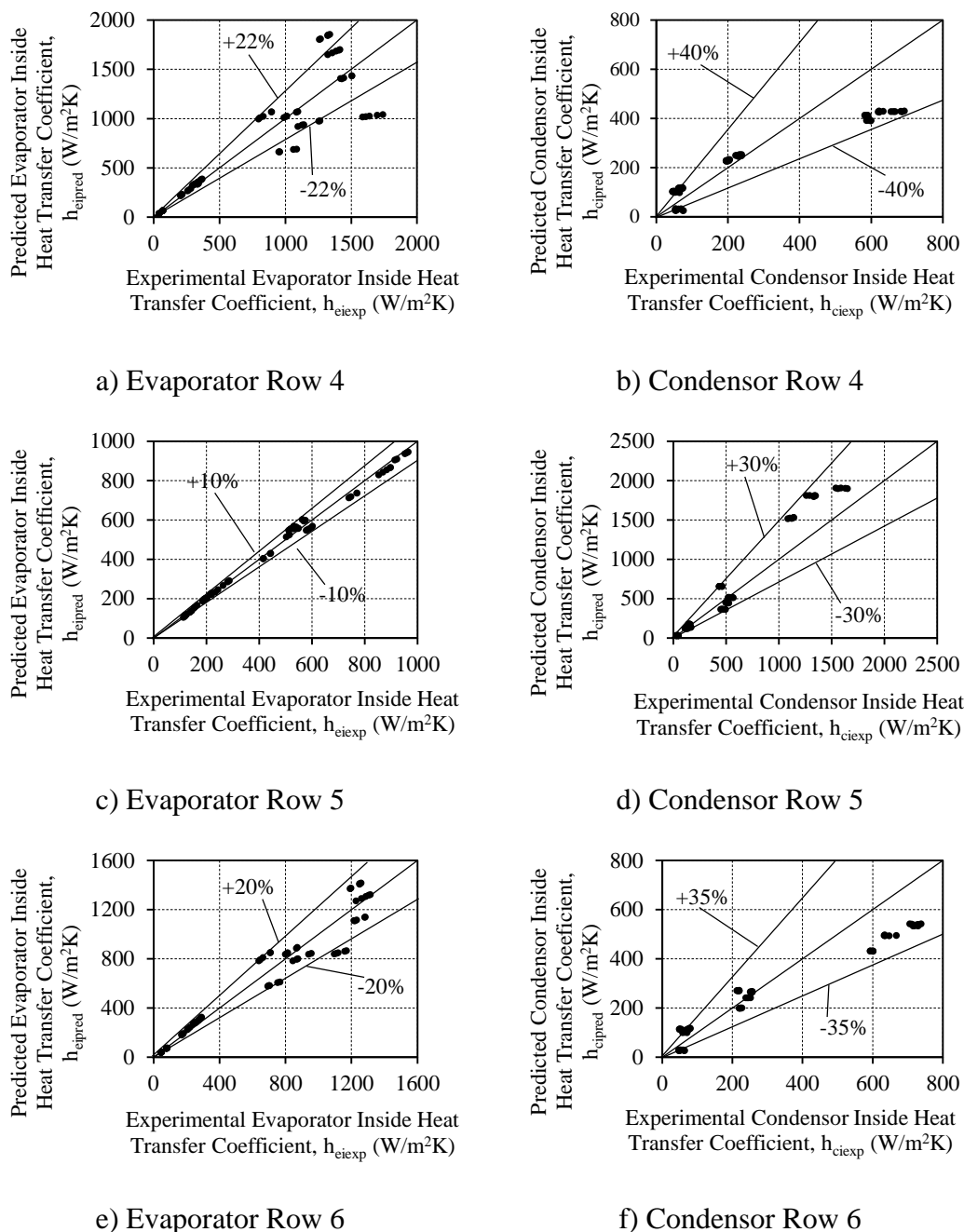


**Figure 43** Inside heat transfer coefficients for the separated-HPHE operating with R123 and charged to 50 % of the evaporator length for Row 4-6

### 6.1.5 Inside temperature distribution and comparison with numerical predictions

The inside temperature distribution of the separated-HPHE is important to establish whether the heat exchanger is working. Since the thin copper walls offer little thermal resistance, it is safe to assume the measured wall temperature is close to the working fluids' temperature. Figures 44 to 46 show the comparison between the temperatures in the riser tubes and the temperatures in the down comer tubes. It is clear from the results that the temperature in the risers is on average 6 °C higher than the down comer temperatures. It is also noted that the temperature differences have the same characteristic shape for each refrigerant, regardless of the air mass flow rate and temperature. This is indicative of

the fact that the liquid pool in the down comer tubes of each loop is at sub-cooled temperatures and the vapour in the riser is superheated. Furthermore, it indicates that the liquid first has to boil in the evaporator at a saturation temperature higher than the liquid temperature in the down comer. This is to be expected since the vapour that condenses in the condenser has to mix with the cold liquid in the down comer, cooling it to below the saturation temperature.

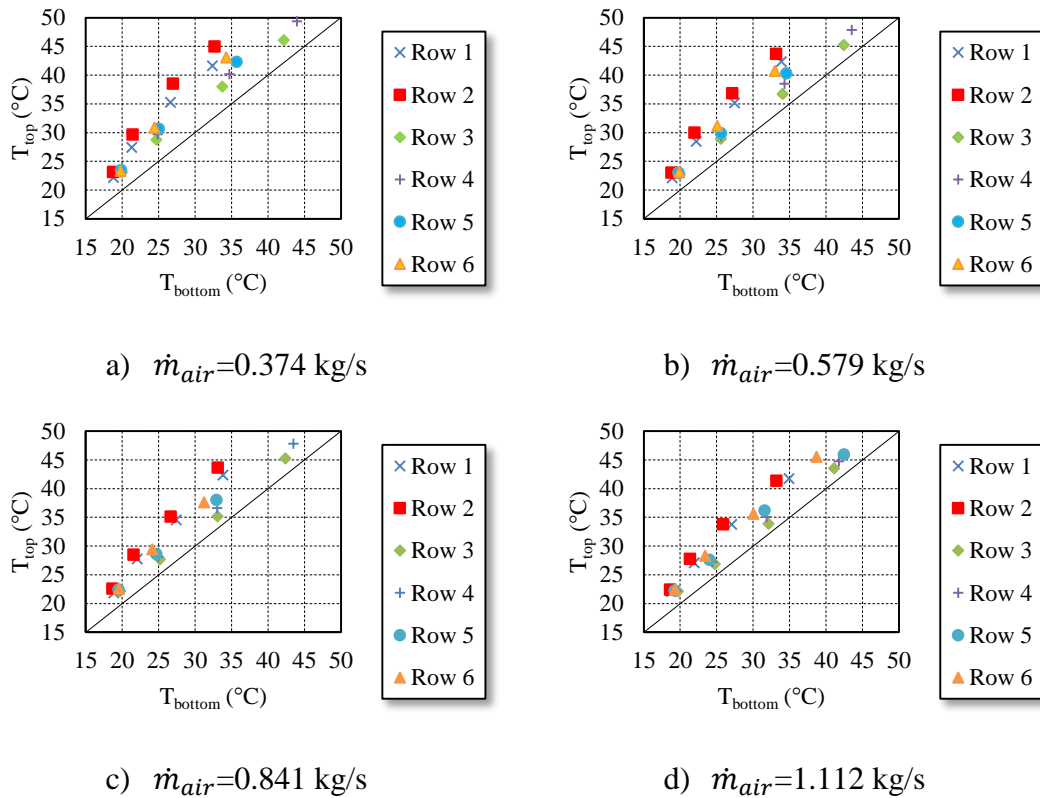


**Figure 44** Inside temperature distribution of the separated-HPHE charged with R600a for the various rows at different mass flow rates

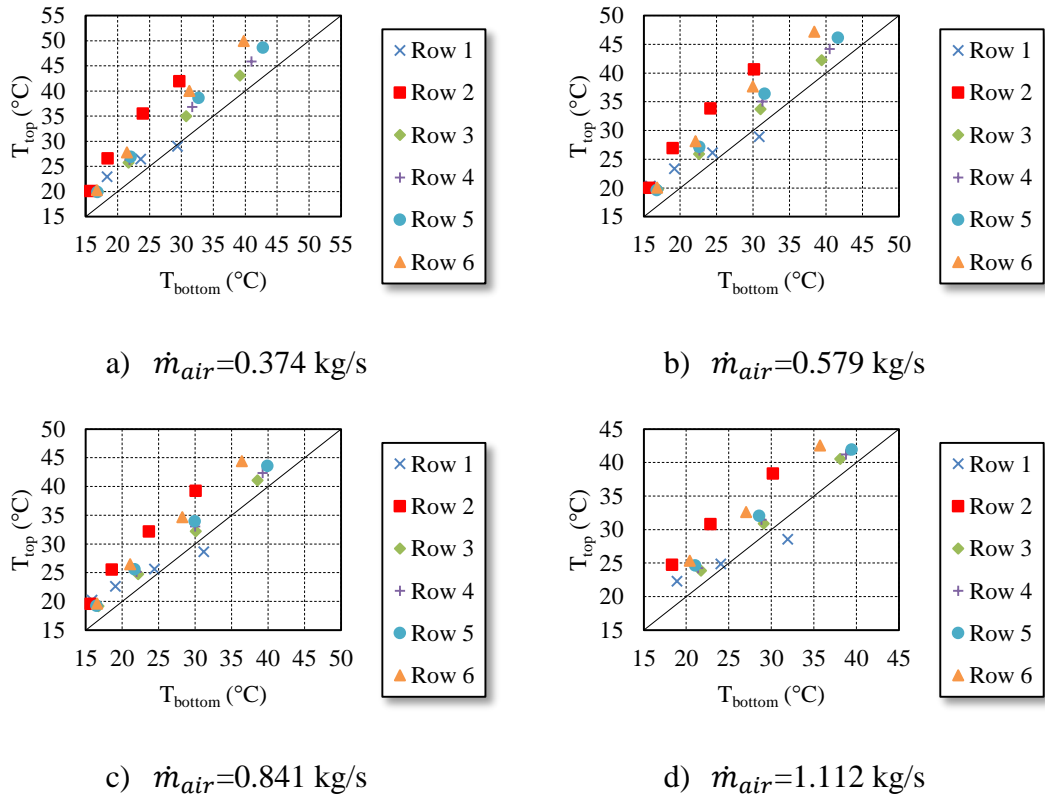


**Figure 45** Inside temperature distribution of the separated-HPHE charged with R134a for the various rows at different mass flow rates

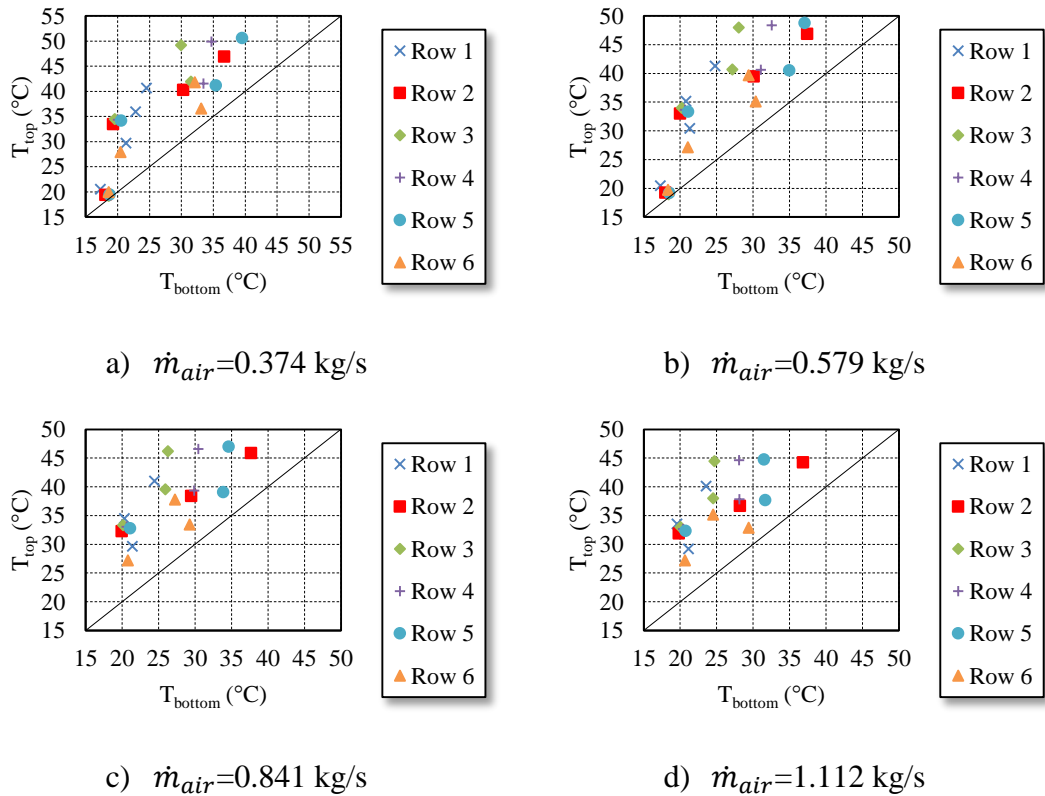


**Figure 46** Inside temperature distribution of the separated-HPHE charged with R123 for the various rows at different mass flow rates

Figure 47 to 49 illustrate the predicted performance of the heat exchanger compared to the experimental results at an air mass flow rate of 0.841 kg/s. The program predicts the heat transfer rates to within 15 % of the experimental values and thus can be used with confidence. Due to the fact that the program does not consider refrigerant flow properties in the risers, the prediction for R123 at lower temperatures is incorrect.

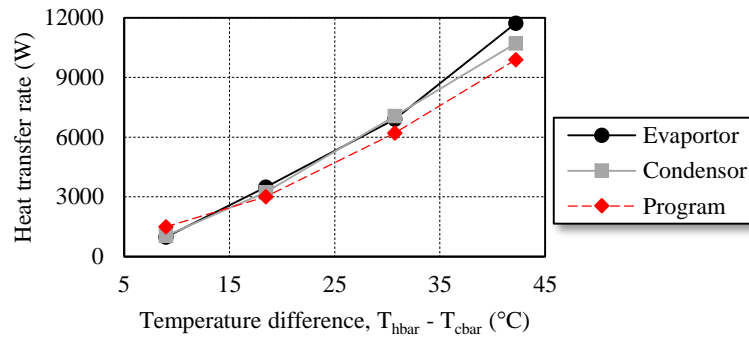


**Figure 47** Comparison between the evaporator and condenser heat transfer rates and the mathematical model of the separated-HPHE charged with R134a at an air mass flow rate of 0.841 kg/s

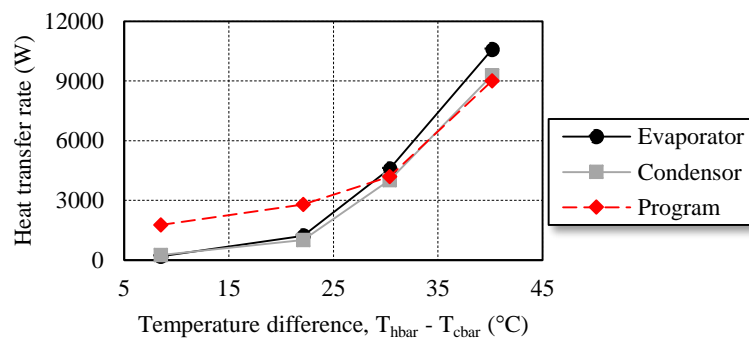


**Figure 48** Comparison between the evaporator and condenser heat transfer rates and the mathematical model of the separated-HPHE charged with R123 at an air mass flow rate of 0.841 kg/s

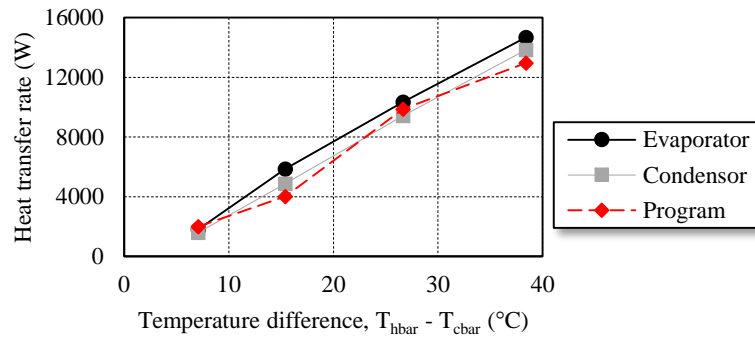


**Figure 49** Comparison between the evaporator and condenser heat transfer rates and the mathematical model of the separated-HPHE charged with R600a at an air mass flow rate of 0.841 kg/s

From Figure 47, for R600a and at a given air mass flow rate and inlet temperature of 76 °C, it can be seen that a heat recovery ( $\dot{Q}_{cond}$ ) of 13.828 kW is attainable with a heat input ( $\dot{Q}_{evap}$ ) of 14.664 kW. At the same operating conditions, a heat recovery of 9.586 kW is attainable at a heat input of 11.05 kW for R123. The heat recovery of R134a is 10.56 kW from a heat input of 11.67 kW. This yields heat exchanger efficiencies, based on these values, of

$$\eta_{R600a} = \dot{Q}_{evap} / \dot{Q}_{cond} = 94,29 \% \quad (6.45)$$

$$\eta_{R123} = \dot{Q}_{evap} / \dot{Q}_{cond} = 86.76 \% \quad (6.46)$$

$$\eta_{R134a} = \dot{Q}_{evap} / \dot{Q}_{cond} = 90.48 \% \quad (6.47)$$

Figures 50 to 55 show the comparison between the inside heat transfer coefficients obtained by using the theoretical models presented in Section 3, the multi-linear regression equations obtained in Section 6 and the experimentally obtained  $h$ -values. Considering the inside evaporator  $h$ -value, the results show that the models given by Semena, Nusselt and Imura under predict the  $h$ -values, while the model given by Shiraishi over predicts the  $h$ -values. For the condenser inside  $h$ -values, the Faghri model gives a reasonable prediction of the  $h$ -value, while the model proposed by Wang & Ma highly over predicts the  $h$ -values. The reason for the differences where applicable are attributed mainly to the fact that the researchers conducted their experiments on a single thermosyphon/s while the results for this study were obtained using the entire heat exchanger. Other factors like manifold design and riser and down comer tube diameters had no influence on the other researchers' experiments, while in this case it could be the main flow restriction preventing effective heat transfer. All things considered, the models obtained in the experiments conducted for this study do not fall within reasonable percentages of the values predicted by the various researchers. It should also be questioned whether the researchers models incorporate the working fluids considered in this study (R123, R134a, R600a).

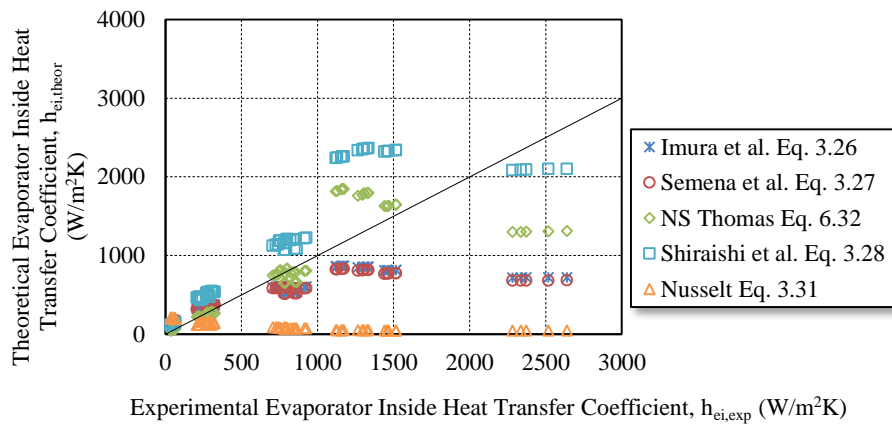


**Figure 50** Comparison between the theoretically determined inside evaporator coefficients for R123

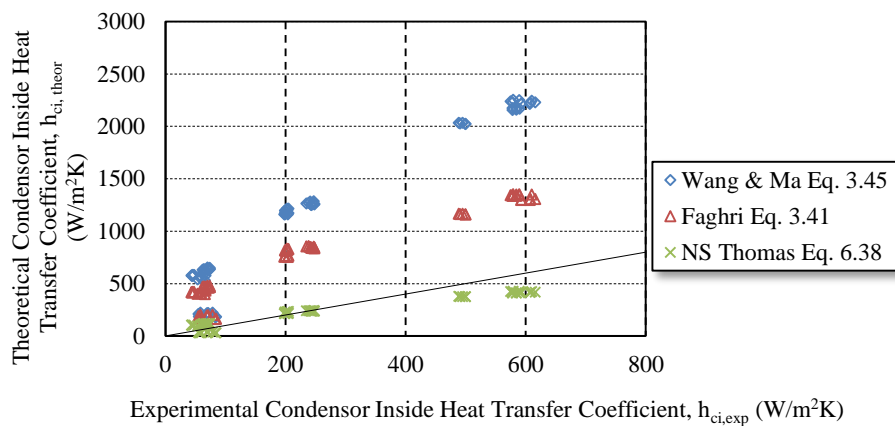


**Figure 51** Comparison of the theoretically determined inside condenser coefficients for R123

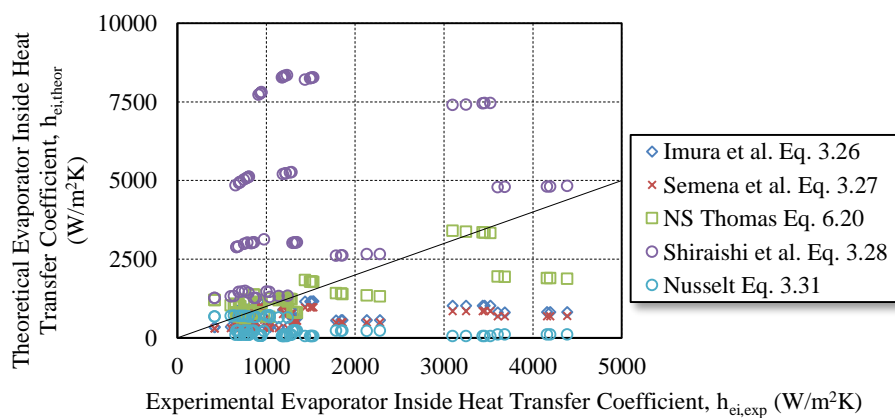


**Figure 52** Comparison between the theoretically determined inside evaporator coefficients for R134a



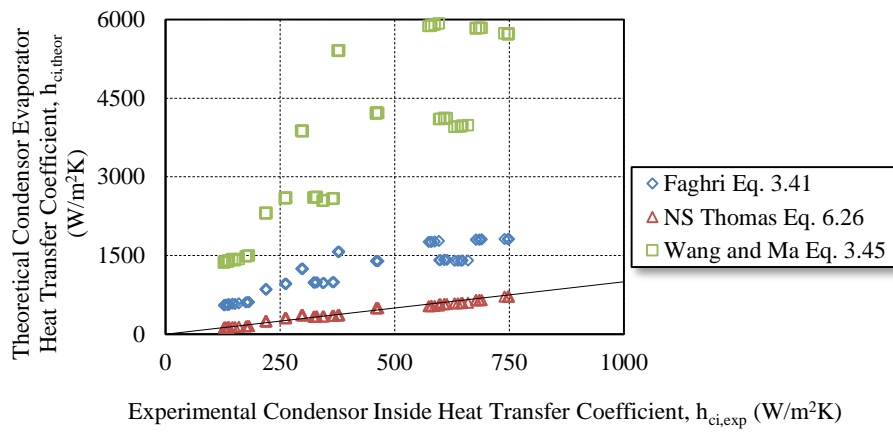


**Figure 53** Comparison of the theoretically determined inside condenser coefficients for R134a

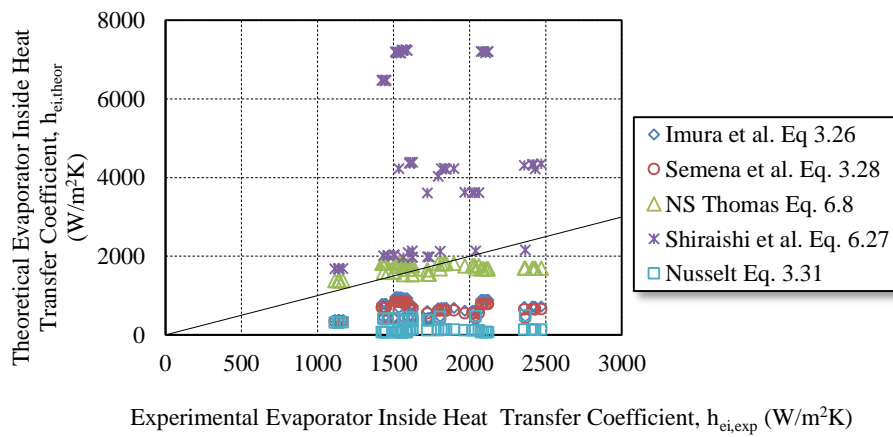


**Figure 54** Comparison between the theoretically determined inside evaporator coefficients for R600a

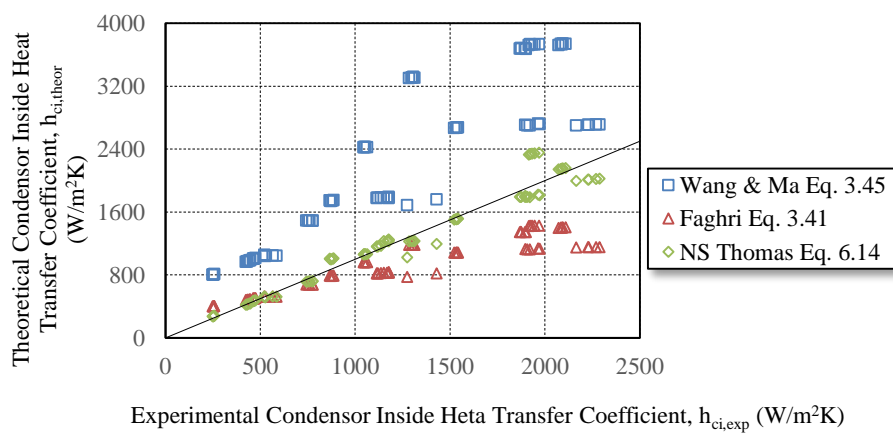


**Figure 55** Comparison of the theoretically determined inside condenser coefficients for R600a

## 7 DISCUSSION AND CONCLUSIONS

In this section the work undertaken in this study will be discussed and a final conclusion given on whether the study has reached the set objectives.

A literature study was conducted to understand the factors influencing drying, heat pipe and thermosyphon operation. For drying it was identified that factors such as material thickness and composition, drying temperature and air velocity have the largest influence on product drying time. For the heat exchanger factors such as pipe diameter, evaporator and condenser lengths, outside surface geometry and inside heat transfer characteristics are the most important for optimal design. While it was impractical and outside the scope of the thesis to investigate the influence of pipe diameter, tube lengths and outside surface geometries, because this would require empirical studies or tedious experimental setups, the inside heat transfer coefficient and thermal performance of the HPHE can be easily investigated. The design of the heat exchanger was aimed at use in the food drying industry. Thus, the primary focal point was to investigate the thermal performance of a separated-HPHRHE at temperatures encountered in the food drying industry using commonly encountered refrigerants and whether the separated-HPHRHE would yield substantial dividends if installed.

The thermal performance of the heat exchanger varies according to the temperature range and the working fluid in the heat exchanger. For this reason, three different working fluids (R600a, R134a and R123) were used and evaluated in the low temperature range.

To accurately predict the thermal performance of a separated-HPHE, the outside and inside heat transfer coefficients need to be known. The outside heat transfer coefficient is dependent on the geometry of the heat exchanger and the air duct it is situated in. The outside heat transfer properties were investigated by running cold water through a heat exchanger of similar outside geometry to those used for the separated-HPHE and passing hot air over the heat exchanger. It was assumed that the temperature profile varies linearly along the heat exchanger for the water and the air. The predicted outside heat transfer coefficients matched the experimental data well and can thus be used with confidence for a heat exchanger of a similar geometry as defined in Section 4, Table 3. Typical scatter about the reference line was in the order of 5-15 %.

The inside heat transfer coefficient of many working fluids in different pipe diameters can be modelled by existing correlations (ref. Section 2.2.1), but these correlations do not model the common refrigerants used in this study accurately enough. Additionally, the two phase flow is difficult to model due to its chaotic nature and no literature exists on the use of common refrigerants in separated-HPHE's. Thus the inside heat transfer coefficients were determined experimentally.

To evaluate the performance of the different refrigerants and develop evaporator and condenser inside heat transfer coefficients, the separated-HPHE shown in Section 5, Figure 27 was charged to a fill charge ratio of 50 % of the evaporator length with the respective working fluid in each loop. The heat flux for the experiments ranged from 700-16000 W/m<sup>2</sup>. To verify that the separated-HPHE was indeed working, the energy balances were first evaluated and these yielded values in the range of 8-13 % across the entire range of experiments and thus the measurements were deemed satisfactory for further data manipulation.

As noted in Section 6, the performance of the HPHE is greatly influenced by the working fluid. For similar temperature differences and mass flow rates, Figures 33, 37 and 41 indicate the performance of the heat exchanger. R600a and R134a work well even with relatively small temperature differences, but R123 is working very poorly the same stage. The reason for this is attributed to the density of R123 vapour in combination with its high latent heat of vaporisation. Compared to relatively small densities of R600a (0.00251 g/cm<sup>3</sup>) and R134a (0.00425 g/cm<sup>3</sup>), R123 has a rather high density of 1.4368 g/cm<sup>3</sup>. In a separated-HPHE arrangement, the evaporator and condenser are separated by a finite distance which the vapour must first travel before condensing and releasing its large latent heat of vaporisation. Additionally, the vapour must travel upward and has to contend with gravitational effects. Hence, because the gas is heavier, it requires a larger driving force (heat input) to reach the condenser section. The high latent heat required to boil the R123 also means a higher heat input is needed for proper operation. However, at higher temperature differences, it is observed that the heat recovered per unit temperature difference for R123 is higher than both R600a and R134a. This indicates that where there is a higher temperature difference, R123 should work as well as if not better than the other options considered in this study.

The separated-HPHE arrangement was also used to determine the inside heat transfer coefficients of the heat exchanger with different working fluids. The physical behaviour was modelled by equations correlating all the working fluid properties. For the evaporator inside heat transfer coefficients, the dimensionless Kutateladze and Jacob numbers were used because they involve all the properties of interest (density and latent heat of vaporisation for example). The predicted  $h$ -values were generated by using multi-linear regression techniques. With R600a as refrigerant, it was found that the  $h$ -values correlate the experimental  $h$ -values between 10-30 % as seen in Section 6.2.2. Considering the chaotic two phase flow phenomena, the poor manifold header design (which impacts on vapour flow) and the long distance the refrigerant has to transverse to reach the condenser and be effective, the  $h$ -values' error was acceptable. However, the multi-linear regression yielded low correlation coefficients ( $R^2$ ). These low correlation coefficients are as a result of the evaporator inside heat transfer coefficients staying relatively constant (see Figures 37 and 38, Section 6.2.2). A suggestion is that for better  $R^2$

values to be obtained, the  $h$ -values could possibly be formulated with a power series expansion containing more variables. The predicted condenser inside heat transfer coefficients correlate to the experimental  $h$ -values between 10-25 %. For the condenser inside heat transfer coefficients, the dimensionless numbers used are the Reynolds number and a ratio of the liquid density to the vapour density of the refrigerant (See equations 6.15 to 6.20). These correlations also yielded high  $R^2$  values, and thus can be used with confidence.

R134a exhibited similar behaviour to R600a. The predicted evaporator  $h$ -values correlate the experimental  $h$ -values between 8-35 % and have low  $R^2$  values. It is again observed that the evaporator  $h$ -values stay relatively constant (Figures 38 and 39). The condenser inside heat transfer coefficients correlate the experimental values to between 10-16 % and have high  $R^2$  values and can thus be used with confidence.

The predicted  $h$ -values were not correlated well with the experimental  $h$ -values for R123. Figure 42 and 43 indicate that the predicted evaporator  $h$ -values correlate the experimental evaporator  $h$ -values to between 10-33 %. However the  $R^2$  values are high. The predicted condenser inside heat transfer coefficient values correlated the experimental inside heat transfer coefficient values to between 30-40 % with relatively good  $R^2$  values. The primary reason for the scatter in the data is the fact that R123 is not working properly at low temperature differences, as seen in Figure 41. This would yield very low  $h$ -values. On the other end of the spectrum, the fact that when the heat exchanger is working, the heavy gas coupled with the heavy liquid blasting up and down in the evaporator could cause some scatter in the  $h$ -values. Add to this the poor manifold header design, in which the eleven tubes have to join to one tube it is easily understandable why the heat transfer coefficients are poorly predicted.

The manifold design has been discussed and identified as an area of possible improvement, but coupled to this is the small pipe diameter chosen for the heat exchanger. Especially in the evaporator, where the heat input causes very random “smash up” flow, the pipe diameter plays a role. While the geometric design of the HPHE was not an express objective of this study, its effects have to be considered for future optimisation of the system.

Comparable to the experimental results, the numerical simulation predicted similar values for achievable heat transfer rates. Thus the simulation program can be used with confidence. The values were slightly less due to the fact that the program uses empirically calculated values to find the heat transfer resistances, but the heat transfer rates are predicted to within 12 % and is deemed sufficient. The only problem occurs at the low temperature end of R123, where the program does not take into account that the R123 is not working. The theoretical correlations presented in Section 3.1 do not correspond well with the values obtained for the separated-HPHE. This is largely attributed to the fact that the researchers obtained their results by evaluating a single thermosyphon, whereas this study

utilised the entire heat exchanger. Thus, while the behaviour of the working fluid was not as carefully controlled in this study, the correlations obtained were used in the numerical program and yielded predictions within an acceptable range, as mentioned above. The insights gained from this study can thus be justified.

While the separated-HPHRHE was not installed in an actual drying application to verify the actual savings and operation, it is clear from the cost study in Appendix E that there are substantial financial savings to be realized by utilising such a heat exchanger. Even in the worst case scenario the payback period of the heat exchanger unit would not exceed 3 years.

The main objective of the thesis was met in as much as that the as-tested separated-HPHRHE was shown to work effectively (recovering up to 90 % of the of the dryer exhaust heat) for typical food industry drying temperatures of between 25 and 80 °C. Furthermore, the theoretical simulation models for the HPHRHE was validated in as much that its energy saving performance was within  $\pm 12$  % of the as-tested experimental models; and thus it was demonstrated that substantial energy cost saving could be realised using standard heat exchanger manufacturing technology, but in a novel application. Hence it is recommended that more and more use needs to be made of HPHRHE technology.

## 8 RECOMMENDATIONS FOR FUTURE WORK

This section discusses the recommendations made for future work to be conducted relating to the content of this thesis. It is intended that these recommendations merely serve as the starting point for further investigations and designs of thermosyphons and HPHE's. These are the recommendations made:

- The heat exchanger design was not an express objective of this thesis and as such there could not be optimal flow of the refrigerant in each thermosyphon loop. It is recommended that the manifold and geometric design of the heat exchanger be optimised for better refrigerant flow. Also, the effect of these various changes have to be investigated.
- It was found that if the working fluid is very dense (as is the case with R123), the distance between the evaporator and the condenser plays a vital role in the operation of a separated-HPHRHE. Thus it is recommended that the relationship between heat input and the distance between the two sections be investigated.
- Each loop in the separated-HPHRHE was filled with a charge fill ratio of 50% of the evaporator length. For effective low temperature operation this could be a limiting factor because of the amount of energy that must be added to boil off the vapour. Thus a separated-HPHRHE should be investigated with different charge fill ratios.
- While the inside heat transfer coefficients were determined to reasonable accuracy, they would be better still if a single thermosyphon was considered, as the flow would be more controllable. The single thermosyphon could then be filled with a variety of common refrigerants (R502, R417, R600a et cetera) to establish which working fluid is best suited to a specific temperature range.
- The computer program should be made user friendly for use in industry. Subject to the determination of the inside heat transfer coefficients as per Recommendation 4, the program may be used with confidence to develop a range of separated-HPHRHE's.
- A computational fluid dynamics (CFD) analysis must be done to better understand the boiling characteristics and investigate the inside heat transfer coefficients. Also to investigate the flow of the gas in the riser tube and the look into sufficient riser tube design requirements.
- For lower temperature applications, the refrigerant used should have a combination of a relatively low latent heat of vaporisation and a gaseous state that is not very dense at the application temperatures. For higher temperatures, heavier working fluids may be considered as the heat input will easily overcome the latent heat of vaporisation. The selection of refrigerants should thus be carefully coupled to these properties.

## REFERENCES

- Abou-Ziyan, H.Z., Helali, A., Fatouh, M. & Abo El-Nasr, M.M. 2001. Performance of a stationary and vibrated thermosyphon working with water and R134a, *Applied Thermal Engineering* 21: 813-830.
- ASHRAE Handbook Fundamentals. 2009. *American Society of Heating, Refrigeration and Air Conditioning Engineers*, Atlanta
- Cengel, Y.A. (2004). *Heat transfer-a practical approach*. 2<sup>nd</sup> edition. McGraw-Hill.
- Churchill, S.W. & Bernstein, M. 1977. A Correlating Equation for Forced Convection from Gases and Liquids to a Circular Cylinder in Cross Flow. *International Journal of Heat Transfer* 99: 300-306.
- DeWatwal, J. 2009. *Design of compact plate fin heat exchanger*. Bachelor's Thesis. Roukela: Indian National Institute of Technology
- Dobson, R.T. & Jeggels, Y.U. 2008. Cooling of Electronic Equipment using Bent and Closed Loop Two-phase Thermosyphons, *9<sup>th</sup> International Heat Pipe Symposium*, Kuala Lumpur, Malaysia
- Dobson, R.T. & Kritzinger, O.O. 2008. Electronic Equipment Cabinet Cooling Enhancement using a Two-phase Thermosyphon with Separated Evaporator and Condensor sections, *9<sup>th</sup> International Heat Pipe Symposium*, Kuala Lumpur, Malaysia
- Dobson, R. T. & Kröger, D. G. 2000. Thermal characterisation of an ammonia-charged two-phase closed thermosyphon. *R & D Journal* 16.2: 33-40
- Dobson, R.T. & Mafokeng, T. 2011. *Flow and heat and mass transfer in a food air drier*. Bachelor's Thesis. Stellenbosch: University of Stellenbosch
- Dobson, R.T. & Meyer, A. 2006. Thermal Performance Characterization of R134a and Butane Charged Two-Phase Closed Thermosyphons. *R & D Journal* 22.3
- Dobson, R.T. & Pakkies, S.A. 2002. Development of a heat pipe (two-phased closed thermosyphons) heat recovery heat exchanger for a spray drier. *Journal of Energy in Southern Africa* 13.4
- Dobson, R.T. 2001. *Fundamentals of Food Engineering for Food Scientists and Technologies*, Faculty of Engineering, University of Stellenbosch
- Dobson, R.T. 2006. Energy Saving using Heat Pipe Heat Recovery Heat Exchangers. *South African Energy Efficiency Convention (SAEEEC)*. Gauteng, South Africa
- Dunn, D.P. & Reay, D. 1994. *Heat pipes*, 4<sup>th</sup> Edition, Pergamon

- El-Genk, M. & Saber, H.H. 1997. Flooding limit in closed, two-phase flow thermosyphons, *International Journal of Heat & Mass Transfer* 40: 2147-2164
- Emani, M.R.S. 2012. Mathematical Modelling of Thermosyphon Heat Exchanger for Energy Saving. *The Journal of Mathematics and Computer Science* 5.4: 271-279
- Faghri, A. 1995. *Heat pipe science and technology*. Taylor & Francis
- Figliola, R.S. & Beasley, D.E. 2011. *Theory and Design for Mechanical Measurements*. 5<sup>th</sup> Edition, John Wiley, Danvers
- Hovac Ltd. 2002. *Handbook for Design, Installation and Operation*, Hovalwerk AG, Liechtenstein
- Ivanovskii, M.N., Sorokin, V.P. & Yagodkin, I.V. 1982. *The physical principles of heat pipes*. Oxford University Press, New York
- Johannsen, A. 1981. Equations and procedures for plotting psychometric charts in SI units by computer. *CSIR Report*, ME 1711, Pretoria
- Kutateladze, S.S. 1972. Elements of hydrodynamics of gas-liquid systems. *Fluid Mech. Sov. Res* 1: 29-50
- Kröger, D.G. 1998. *Air-cooled heat exchangers and cooling towers*. Department of Mechanical Engineering, University of Stellenbosch
- Lukitobudi, A.R., Akbarzadeh, A., Johnson, P.W. & Hendy, P. 1995. Design, construction and testing of a thermosyphon heat exchanger for medium temperature heat recovery in bakeries. *Heat Recovery Systems and CHP* 15.5: 481-491
- Lock, G.S.H, 1992. *The tubular thermosyphon—variations on a theme*, Oxford Science Publications
- Meyer, A. 2003. *Development of a range of air-air HPHRHE*. Master's Thesis. Stellenbosch: University of Stellenbosch
- McQuay Int. 2001, *Engineering System Solutions*, Edition 8, Minneapolis
- Mohan Jagadesh Kumar, M., Kaushik, S.C. & Garg, S.N. 2014. Thermodynamic Performance evaluation of an air to air heat-pipe-heat exchanger. *Journal of Thermal Science* 18.4: 1343-1353
- Mujumbar, A.S. 2007. *Handbook of Industrial drying*. 3<sup>rd</sup> ed, Boca Raton: CRC
- Noie-Baghban, S.H. & Majideian, G.R. 2000. Waste heat recovery using heat pipe heat exchanger (HPHE) for surgery rooms in hospitals. *Applied Thermal Engineering* Vol. 20: 1271-1282
- Nozu, S. 1969. Studies related to the heat pipe, *Trans. Soc. Mech. Engrs. Japan* 35.2: 392-401



- Nuntaphan, A., Tiansuwan, J. & Kiatsiriroat, T. 2002. Enhancement of heat transport in thermosyphons air preheater at high temperature with binary working fluid: A case study of TEG-water. *Applied Thermal Engineering* 22:251-266
- Park, Y.J., Kim, C.J. & Kang, H.K. 2002. Heat transfer characteristics of a two-phased closed thermosyphon to the fill charge ratio. *International Journal of Heat and Mass Transfer* 45: 4655-4661
- Paul Singh, R. & Heldman, D.R. 2009. *Introduction to Food Engineering*. 4<sup>th</sup> ed, Academic Press, China
- Payakaruk T, Terdtoon P, Ritthidech S. 2000. Correlations to predict heat transfer characteristics of an inclined closed two phase thermosyphon at normal operating conditions, *Applied Thermal Engineering* 20: 781-790
- Peterson, G.P. 1994. *An introduction to heat pipes – modelling, testing and applications*, John Wiley and Sons
- Pieters, W.H. 2006. Heat pipe heat exchanger technology – saves energy with bottom line benefits, *Mechanical Technology*, July: 4-5
- Pioro, L.S. & Pioro, I.L. 1997. *Industrial two-phase thermosyphons*. Begell House
- Russwurm A.E. 1980. Q-pipes add a new dimension to waste heat recovery, Part 1, *Heating, Air Conditioning & Refrigeration (Now Refrigeration and Airconditioning)*. January: 27-39
- Sauer, H.J., Howell, R.H & Coad, W.J. 2009. *Principles of Heating and Ventilation and Air Conditioning*. 6<sup>th</sup> Edition, ASHRAE
- Sharma, S.K., Mulvaney, S.J. & Rizvi, S.S.H. 2000. *Food process engineering – theory and laboratory experiments*. John Wiley
- Staton, J.C. 1998. *Heat and Mass Transfer Characteristics of Desiccant Polymers*. Master's Thesis. Blacksburg: Virginia Polytechnic and State University
- Wallis, G.B. 1969. *One dimensional two-phase flow*. McGraw-Hill, New York
- Whalley P.B. 1987. *Boiling, Condensation, and Gas-Liquid Flow*, Clarendon Press, Oxford
- Webb, R.L. 1994. *Principles of enhanced heat transfer*, John Wiley
- Wu, X.P., Johnson, P. & Akbarzadeh A, 1997. Application of heat pipe heat exchangers to humidity control in air-conditioning systems *Applied Thermal Engineering* 17.6: 561-568
- Yang, F., Yuan, X. & Lin, G. 2003. Waste heat recovery using heat pipe heat exchanger for heating automobile using exhaust gas. *Applied Thermal Engineering* 23: 367-372

Yun, J. & Krolczek, E. 2002. Operation of capillary pumped loops and loop heat pipes. *Cooling zone online magazine* 2.6

Zhang, H. & Zhuang, J, 2003. Research, development and industrial application of heat pipe technology in China. *Applied Thermal Engineering* 23: 1067-1083

## Appendix A: Sample Calculations

### A1 Heater power input

Consider the model of the current Nibblibits drier as shown in Figure 58. For the calculations only the methodology is given along with the important answers.

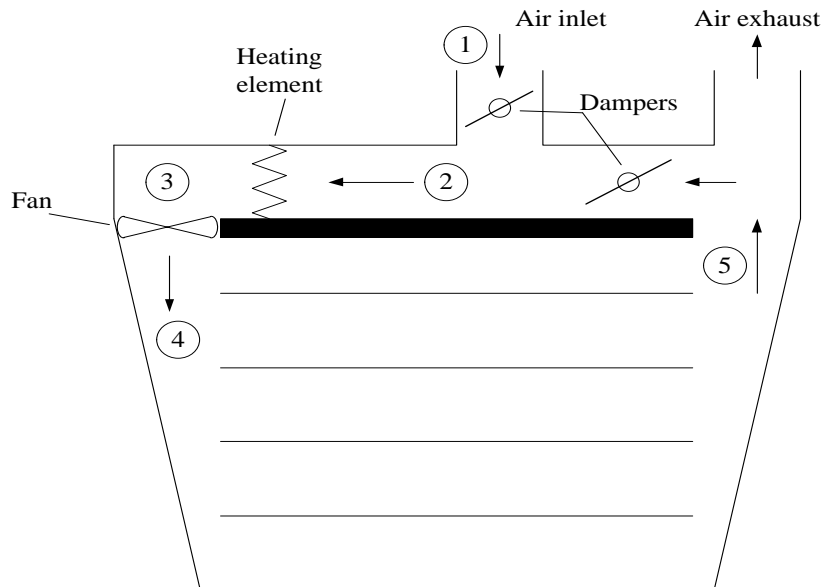


**Figure 56** Current drier design

The drier parameters are given in Table 5.

**Table 5** Drier parameters

Property	Value
$W_{fan}$	1 kW
$T_{1db} = T_{ambient}$	10 °C
$T_{1wb}$	5 °C
$T_{5db}$	70 °C (assumed)
$T_{4db}$	80 °C (desired)
$RH_{@5}$	60 %
$V_1 = V_5$	5 m/s
Altitude (above sea level)	150m

The atmospheric pressure at 150m is calculated using equation B.8 (Appendix B)

$$Baro = 101325 \times (1 - 22.55691 \times 10^{-6} \times 150)^{5.2561} = 99.54 \text{ kPa}$$

Using equation B.1 - B.6, the vapour pressure for the inlet air is found as

$$P_{vs} = 10^{3.07} = 1.1677 \text{ kPa}$$

equation B.9 can then be used to calculate the humidity at the wet bulb temperature is then

$$\omega_s = 7.4204 \times 10^{-3} \text{ kg – water/kg – dry air}$$

the humidity ratio of the air can is then calculated as

$$\omega = 0.0035 \text{ kg – water/kg – dry air}$$

the vapour pressure can be obtained as

$$P_v = 0.52515 \text{ kPa}$$

giving a relative humidity of 45 %. The enthalpy of the air is found using equation B.12

$$h = 18836 \text{ J/kgK}$$

The drier is analysed using basic air-conditioning theory. Firstly, an air mass balance is between point 1, 5 and 2 yields

$$\text{Air mass balance:} \quad \dot{m}_2 = \dot{m}_1 + \dot{m}_5 \quad (\text{A.1})$$

Similarly, a water mass balance is done around the same points, and the humidity ratio at point 2 can be found

$$\text{Water mass balance:} \quad \omega_2 = \frac{\dot{m}_1}{\dot{m}_2} \omega_1 + \frac{\dot{m}_5}{\dot{m}_2} \omega_5 \quad (\text{A.2})$$

Lastly, an energy balance is used around the same points to obtain the enthalpy of the air at point 2

$$\text{Energy balance:} \quad h_2 = \frac{\dot{m}_1}{\dot{m}_2} h_1 + \frac{\dot{m}_5}{\dot{m}_2} h_5 \quad (\text{A.3})$$

The mass flowrate, humidity ratio and energy state of the air at each point is determined in the same way as described above. Between points 2 and 3 the air is heated by an electrical heater and does not mix with any air. Thus:

$$\dot{m}_3 = \dot{m}_2 \quad (\text{A.4})$$

$$\omega_3 = \omega_2 \quad (\text{A.5})$$

and

$$h_3 = h_2 + \frac{\dot{Q}_{heater}}{\dot{m}_2} \quad (\text{A.6})$$

Similarly, between points 3 and 4, the only input is energy addition in the form of the fan work, thus:

$$\dot{m}_4 = \dot{m}_3 \quad (\text{A.7})$$

$$\omega_4 = \omega_3 \quad (\text{A.8})$$

$$h_4 = h_3 + \frac{\dot{W}_{fan}}{\dot{m}_3} \quad (\text{A.9})$$

The temperature of the air at point 4 is found using equation B.14, from this the amount of heat transferred to the product surface and the mass flowrate of moisture from the product surface can be obtained using equations 3.112 through to 3.123. The mass flowrate, humidity ratio and the energy state of the air at point 5 can be given by:

$$\dot{m}_4 = \dot{m}_3 \quad (\text{A.10})$$

$$\omega_5 = \omega_4 + \frac{\dot{m}_{evap}}{\dot{m}_4} \quad (\text{A.11})$$

$$h_5 = h_4 + \frac{\dot{m}_{evap}}{\dot{m}_4} h_{fg} \quad (\text{A.12})$$

Thus the state of the air at each point can be established. To obtain a temperature of more than 80 °C at point 4 a heater size of 37 kW is needed for this case. This is in agreement with the CFW heater design size of 36 kW.

The proposed drier design is shown in Figure 59.

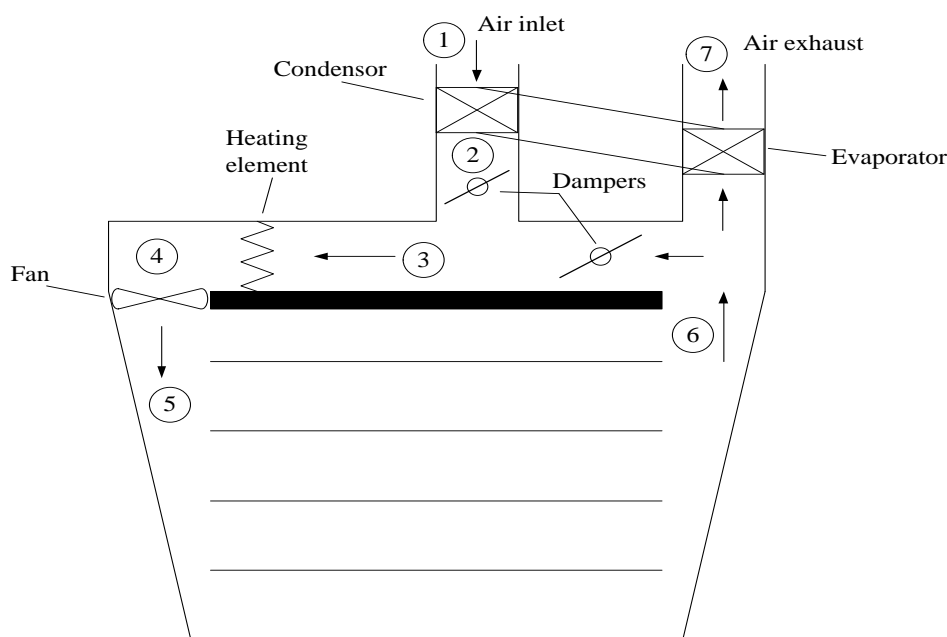


**Figure 57** Proposed drier design

Similar to the analysis done for the current drier, air, water and energy balances are done between different points. The only difference in the analysis is the inclusion of the heat exchanger. Thus, between points 1 and 2

$$\dot{m}_1 = \dot{m}_2 \quad (\text{A.13})$$

$$\omega_3 = \omega_2 \quad (\text{A.14})$$

$$h_2 = h_1 + \frac{\dot{Q}_{hp}}{\dot{m}_1} \quad (\text{A.15})$$

Then, between points 2, 6 and 3

$$\dot{m}_3 = \dot{m}_2 + \dot{m}_6 \quad (\text{A.16})$$

$$\omega_3 = \frac{\dot{m}_2}{\dot{m}_3} \omega_2 + \frac{\dot{m}_6}{\dot{m}_3} \omega_6 \quad (\text{A.17})$$

$$h_3 = \frac{\dot{m}_2}{\dot{m}_3} h_2 + \frac{\dot{m}_6}{\dot{m}_3} h_6 \quad (\text{A.18})$$

Between points 3 and 4

$$\dot{m}_4 = \dot{m}_3 \quad (\text{A.19})$$

$$\omega_4 = \omega_3 \quad (\text{A.20})$$

$$h_4 = h_3 + \frac{\dot{Q}_{heater}}{\dot{m}_3} \quad (\text{A.21})$$

Points 4 and 5

$$\dot{m}_5 = \dot{m}_4 \quad (\text{A.22})$$

$$\omega_5 = \omega_4 \quad (\text{A.23})$$

$$h_5 = h_4 + \frac{\dot{W}_{fan}}{\dot{m}_4} \quad (\text{A.24})$$

Again the temperature at the dryer inlet can be found using Eq. B.14. Between points 5 and 6

$$\dot{m}_6 = \dot{m}_5 \quad (\text{A.25})$$

$$\omega_6 = \omega_5 + \frac{\dot{m}_{evap}}{\dot{m}_5} \quad (\text{A.26})$$

$$h_6 = h_5 + \frac{\dot{m}_{evap}}{\dot{m}_5} h_{fg} \quad (\text{A.27})$$

For the drier with the HPHRHE, a heater capacity of **27 kW** is needed

## A.2 Drying time estimation

Consider a sample of a product with dimensions and mass as shown in Figure 24 along with the drying process variables

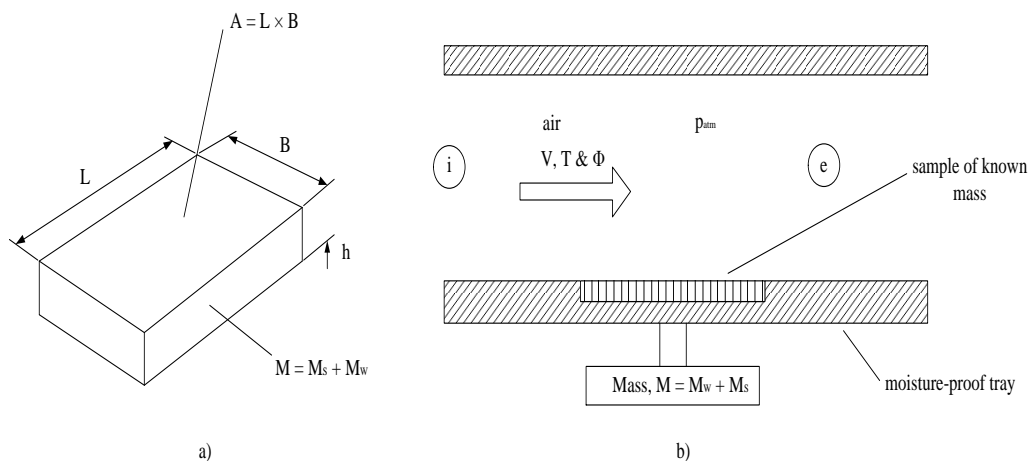


**Figure 58** a) Sample of product, b) Process variables

The values for the respective symbols in the figure are given in tabular form below.

**Table 6** Values of variables in Figure 65

Variable	Value (unit)
T	80 °C
V	5 m/s
B	0.05 m
L	0.1 m
h	0.05 m
Φ	60 %

For now, it is assumed that the product will undergo a constant rate and falling rate drying period as per Figure 14 and that the product has an initial density of 100 kg/m<sup>3</sup>. Using equation 3.115, the moisture flowing from the product in the constant rate drying period is

$$\dot{m}_w = \frac{h(L \times B)}{h_{fg}} (T_\infty - T_s) = 4.824 \times 10^{-6} \text{ kg - water/kg - solids.s}$$

The initial moisture content of the product is 30 % while the critical moisture content is 22 %. From this, equation 3.124 gives the time duration of the constant rate period

$$t_{0 \rightarrow cr} = \frac{X_0 - X_{cr}}{\dot{m}_w} = 5.5 \text{ hours}$$

The falling rate drying period time prediction requires the diffusivity of water in the product to be known. This must be done experimentally, but for now an approximation may be made. Knowing the drying rate just before the falling rate drying period begins, the diffusivity – using Fick's law – can be calculated as

$$\frac{dX}{dt} = (X - X_e) \times \frac{1}{h^2} \times D \quad (\text{A.28})$$

which gives the diffusivity as

$$D = 3.998 \times 10^{-8} \text{ m}^2/\text{s}$$

Knowing the respective moisture content values and the diffusivity, the time to reach the equilibrium moisture content from the critical moisture content can be calculated, using equation 3.126 as

$$t_{cr \rightarrow e} = 1830.8 \text{ s} = 0.51 \text{ hours}$$

the total drying time is then simply the sum of the constant-rate and falling-rate periods

$$t_{tot} = t_{0 \rightarrow cr} + t_{cr \rightarrow e} \cong 6.15 \text{ hours}$$

which corresponds well with the approximate drying time given by Mr S Drees of 6.5 hours.

### A.3 Calculation of outside heat transfer coefficients

The data for calculation of the row-by-row outside heat transfer properties is given in Table 7.

**Table 7** Data for calculation of outside heat transfer coefficients

Property	Value
$T_{air,in}$	37.172 °C
$T_{air,out}$	33.752 °C
$T_i$	15.83 °C
$\dot{m}_{air}$	0.984 kg/s
$\dot{m}_w$	0.610 kg/s
$d_{po}$	0.0158 m
$d_{pi}$	0.0148 m
$L_{evap}$	0.35 m
$N_p$	11

The average temperature and specific heat of the air flowing through the row of thermosyphons is

$$\bar{T}_{air} = (T_{air,in} + T_{air,out})/2 = \frac{(37.172+33.752)}{2} = 35.452 \text{ °C}$$

$$c_{p@T_{air}=35.452^\circ C} = 1007.313 \text{ J/kgK}$$

thus the heat lost by the air is

$$\begin{aligned} \dot{Q}_{HE} &= \dot{m}_{air} c_{p@T_{air}} \Delta T_{air} = 0.984 \times 1007.313 \times (37.172 - 33.752) \\ &= 3389.8 \text{ W} \end{aligned}$$



The heat lost by the air is exactly the same as the heat transferred through the pipe wall to the water, thus

$$\dot{Q}_{HE} = \frac{\bar{T}_{air} - T_i}{\Sigma R} \quad (A.29)$$

and hence

$$\Sigma R = \frac{(35.452 - 15.83)}{3389.8} = 0.005789 \text{ m}^2\text{K/W}$$

The density and dynamic viscosity of the water flowing inside the thermosyphon tubes is

$$\rho_{w@15.83^\circ\text{C}} = 998.88 \text{ m}^3/\text{kg}$$

$$\mu_{w@15.83^\circ\text{C}} = 0.00111 \text{ m}^2/\text{s}$$

The flow area of the pipes is

$$A_{pi} = \frac{\pi d_{pi}^2}{4} = \pi \times 0.0148^2 / 4 = 0.00017 \text{ m}^2$$

And hence the velocity and the corresponding Reynolds number of the water flowing through the pipes is

$$V_w = \frac{\dot{m}_w}{\rho_{w@15.83^\circ\text{C}} A_{pi}} = \frac{0.61}{998.88 \times 0.00017} = 3.592 \text{ m/s}$$

$$Re_w = \frac{\rho_w V_w d_{pi}}{\mu_w} = \frac{998.88 \times 3.592 \times 0.0148}{0.00111} = 47843.13$$

With a thermal conductivity, Prandtl and Nusselt number of

$$k_{w@15.83^\circ\text{C}} = 0.5967 \text{ W/mK}$$

$$Pr_w = 7.804$$

$$Nu_w = 0.0243 Re_w^{0.8} Pr_w^{0.4} = 0.0243 \times 47843.13^{0.8} \times 7.804^{0.4} = 306.47$$

The inside heat transfer coefficient can thus be found as

$$h_i = \frac{Nu_w k_w}{d_{pi}} = \frac{306.47 \times 0.5967}{0.0148} = 12356.12 \text{ W/m}^2\text{K}$$

And calculating the respective inside and outside heat transfer areas

$$A_{Li} = \pi d_i L_{evap} = \pi \times 0.0148 \times 0.35 = 0.0163 \text{ m}^2$$

$$A_{Lo} = \pi d_o L_{evap} = \pi \times 0.0158 \times 0.35 = 0.0174 \text{ m}^2$$

The inside thermal resistance is

$$R_i = \frac{1}{h_i A_L N_p} = \frac{1}{12356.12 \times 0.0163 \times 11} = 0.0004513 \text{ m}^2 \text{K/W}$$

Using equation 3.51, the thermal resistance across the thermosyphon walls is calculated as

$$R_{wall} = \frac{\ln(d_{po}/d_{pi})}{2\pi k_{pipe} L_{evap} N_p} = \frac{\ln(0.0158/0.0148)}{2\pi \times 386 \times 0.35 \times 11} = 0.0000072 \text{ m}^2 \text{K/W}$$

Manipulating equation 3.8

$$R_o = \sum R - R_i - R_{wall} = 0.00578 - 0.00045 - 0.0000072 = 0.0053 \text{ m}^2 \text{K/W}$$

Thus, the outside heat transfer coefficient for the row of pipes is

$$h_o = (R_o A_{Lo})^{-1} = (0.0174 \times 11 \times 0.0053)^{-1} = 985.78 \text{ W/m}^2 \text{K}$$

#### A.4 Calculation of inside heat transfer coefficients

The inside heat transfer coefficients were calculated in a similar fashion to the outside heat transfer coefficients. The data used for this sample calculation is given in Table 8

**Table 8** Data values for the calculation of the inside heat transfer coefficient

Property	Value
T <sub>hi</sub>	72.052 °C
T <sub>ho</sub>	69.59 °C
T <sub>i</sub>	48.11 °C
$\dot{m}_{air}$	0.7804 kg/s
T <sub>ci</sub>	27.036 °C
T <sub>co</sub>	29.312 °C

The average temperatures across the evaporator and condenser sections are calculated using equations 3.5 and 3.6

$$\bar{T}_{hbar} = (T_{hi} + T_{ho})/2 = (72.052 + 69.59)/2 = 70.82 \text{ °C}$$

$$\bar{T}_{cbar} = (T_{ci} + T_{co})/2 = (27.036 + 29.312)/2 = 28.17 \text{ °C}$$

Dobson (2002) gives the following equations for the heat transfer coefficients needed to evaluate equations 3.8 and 3.9

$$h_{ei} = \left( A_{ei} \left( \left( \frac{\bar{T}_{hbar} - T_i}{\dot{Q}_e} \right) - \frac{1}{h_{eo} A_{eo}} - \frac{\ln(d_o/d_i)}{2\pi k_{cop} L_e} \right) \right)^{-1} \quad (\text{A.30})$$

$$h_{ci} = \left( A_{ci} \left( \left( \frac{T_i - \bar{T}_{cbar}}{Q_c} \right) - \frac{1}{h_{co} A_{co}} - \frac{\ln\left(\frac{d_o}{d_i}\right)}{2\pi k_{cop} L_c} \right) \right)^{-1} \quad (A.31)$$

Where, using equation 3.49

$$A_{eo/co} = \pi N_p d_o L_e = \pi \times 11 \times 0.0158 \times 0.35 = 0.192 \text{ m}^2$$

$$A_{ei/ci} = \pi N_p d_i L_e = \pi \times 11 \times 0.0148 \times 0.35 = 0.179 \text{ m}^2$$

The heat transfer to the thermosyphon loop is given by equation A.32

$$\dot{Q} = \dot{m}_{air} c_{pair@T_{bar}} \Delta T \quad (A.32)$$

using the values given in Table 9

$$\dot{Q}_e = 0.7804 \times 1008.36 \times (72.052 - 69.59) = 1937.41 \text{ W}$$

$$\dot{Q}_c = 0.7804 \times 1006.88 \times (29.31 - 27.04) = 1760.90 \text{ W}$$

the properties of the hot and cold air are calculated using equations B.15 – B.20 and the thermal conductivity of the copper tubes are found from the metal properties section in Appendix B. The outside heat transfer coefficients are found using equation 6.2 and 6.7.

$$d_h = \frac{4A_{duct}}{p_{duct}} = \frac{4 \times 0.35 \times 0.419}{2 \times (0.35 + 0.419)} = 0.381 \text{ m}$$

and the velocity of the air can be determined by

$$V_{air} = \dot{m}_{air} / \rho_{air} A_{duct} \quad (A.33)$$

using equation A.4, the velocities for the respective air streams are calculated as

$$V_c = 0.572 / (1.184 \times 0.146) = 3.29 \text{ m/s}$$

$$V_e = 0.572 / (1.072 \times 0.146) = 3.65 \text{ m/s}$$

the Reynolds number for each air stream can now be calculated as

$$Re_c = \frac{\rho_c V_c d_h}{\mu_c} = \frac{1.184 \times 3.29 \times 0.381}{1.837 \times 10^{-5}} = 80791.08$$

$$Re_e = \frac{\rho_e V_e d_h}{\mu_e} = \frac{1.072 \times 3.65 \times 0.381}{1.978 \times 10^{-5}} = 75367.88$$

The outside heat transfer coefficient for the hot and cold streams can now be calculated as

$$h_{co} = 0.00112 \times 80791.08^{0.9355} \times 0.709^{-7.5615} = 598.942 \text{ W/m}^2\text{K}$$

$$h_{eo} = 0.0364 \times 75367.88^{0.1443} \times 0.701^{-26.603} = 2340.141 \text{ W/m}^2\text{K}$$

Substituting all these values into equations A.30 and A.31

$$h_{ei} = \left( 0.179 \times \left( \left( \frac{70.82 - 48.11}{1937.41} \right) - \frac{1}{2340.141 \times 0.192} - \frac{\ln\left(\frac{0.0158}{0.0148}\right)}{2\pi \times 386 \times 0.35} \right) \right)^{-1}$$
$$= 1175.91 \text{ W/m}^2\text{K}$$

$$h_{ci} = \left( 0.179 \times \left( \left( \frac{48.11 - 28.174}{1760.90} \right) - \frac{1}{598.942 \times 0.192} - \frac{\ln\left(\frac{0.0158}{0.0148}\right)}{2\pi \times 386 \times 0.35} \right) \right)^{-1}$$
$$= 690.48 \text{ W/m}^2\text{K}$$

## Appendix B: Material Properties

The properties of air need to be calculated at various stages in the drier. All equations are obtained from Johannesen (1981) unless otherwise stated. Firstly, it is necessary to find the saturated water vapour pressure,  $P_{vs}$ . Kroger (1998) presents an easy method to obtain this

$$P_{vs} = 10^z \quad (\text{B.1})$$

where the exponent,  $z$ , is equal to

$$z = y + z + x + 2.786118312 \quad (\text{B.2})$$

and where the placeholders are

$$y = 10.79586 \times \left(1 - (273.16/T_{wb})\right) \quad (\text{B.3})$$

$$x = 4.2873 \times (10^{-4}) \times 10^{\left(4.76955 \times \left(1 - \left(\frac{273.16}{T_{wb}}\right)\right) - 1\right)} \quad (\text{B.4})$$

$$z = 1.50474 \times (10^{-4}) \times \left(1 - \left(10^{\left(-8.29692 \times \left(\frac{T_{wb}}{273.16}\right) - 1\right)}\right)\right) \quad (\text{B.5})$$

$$b = 5.02808 \times \log_{10}(273.16/T_{wb}) \quad (\text{B.6})$$

It is then required to find the humidity ratio at the wet bulb temperature

$$\omega_s = \frac{0.62198 \times f \times P_{vs@T_{wb}}}{\text{Baro} - f \times P_{vs@T_{wb}}} \quad (\text{B.7})$$

where Baro is the atmospheric pressure and is given as

$$\text{Baro} = 101325 \times \left(1 - 22.55691 \times 10^{-6} \times \text{altit}\right)^{5.2561} \quad (\text{B.8})$$

$f$  is a correction factor with a value of 1.005. The humidity ratio of the air can then be calculated

$$\omega = \frac{(2501.6 - 2.3263 \times T_{wb}) \times \omega_s - 1.00416 \times (T_{db} - T_{wb})}{2501.6 + 1.8577 T_{db} - 4.184 T_{wb}} \quad (\text{B.9})$$

The vapour pressure is then calculated from

$$P_v = \frac{\text{Baro} \times \omega}{f \times (0.62198 + \omega)} \quad (\text{B.10})$$

The relative humidity,  $\phi$  is then calculated from

$$\phi = \frac{P_v}{P_{vs}} \quad (\text{B.11})$$

The enthalpy,  $h$  can now be calculated

$$h = 1.00416 T_{db} + \omega(2501.6 + 1.8577 T_{db}) \quad (\text{B.12})$$

And the specific volume – and thus the density – is given by

$$v = \frac{287.052 \times (T_{db} + 273.15)}{Baro} \times (1 + 1.6078\omega) \quad (\text{B.13})$$

Equation B.12 can be rearranged to obtain the temperature of the air knowing the state of the air

$$T_{db} = \frac{h - 2501.6\omega}{1.00416 + 1.8577\omega} \quad (\text{B.14})$$

For heat transfer calculations the following properties of air and water are calculated using Kroger (1998).

$$\rho_{air} = p_{air} / (287.08T) \quad (\text{B.15})$$

$$c_{p_{air}} = 1.045356 \times 10^{-3} - 3.161783 \times 10^{-1}T + 7.083814 \times 10^{-4}T^2 - 2.705209 \times 10^{-7}T^3 \quad (\text{B.16})$$

$$\rho_w = (1.49343 \times 10^{-3} - 3.7164 \times 10^{-6}T + 7.09782 \times 10^{-9}T^2 - 1.90321 \times 10^{-20}T^6)^{-1} \quad (\text{B.17})$$

$$c_{p_w} = 8.15599 \times 10^3 - 2.80627 \times 10T + 5.11283 \times 10^{-2}T^2 - 2.17582 \times 10^{-13}T^6 \quad (\text{B.18})$$

$$\mu_w = 2.414 \times 10^{-5} \times 10^{247.8/(T-140)} \quad (\text{B.19})$$

$$k_w = -6.14255 \times 10^{-1} + 6.9962 \times 10^{-3}T - 1.01075 \times 10^{-5}T^2 + 4.74737 \times 10^{-12}T^4 \quad (\text{B.20})$$

### Refrigerant properties

All the refrigerant properties were obtained from ASHRAE (2009).

### Metal properties

Stainless steel

$$\varepsilon_{ss} = 0.015\text{m}$$

$$k_{ss} = 37 \text{ W/mK}$$

Copper

$$k_{cop} = 386 \text{ W/mK}$$

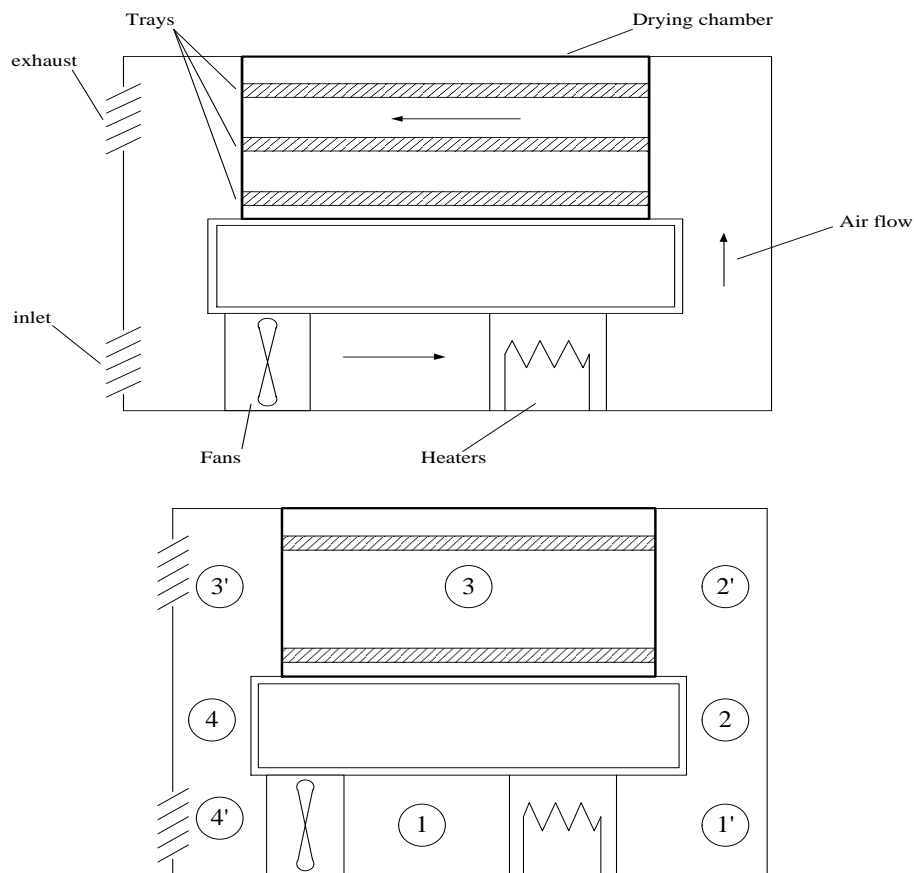
Aluminium

$$k_{alum} = 240 \text{ W/mK}$$

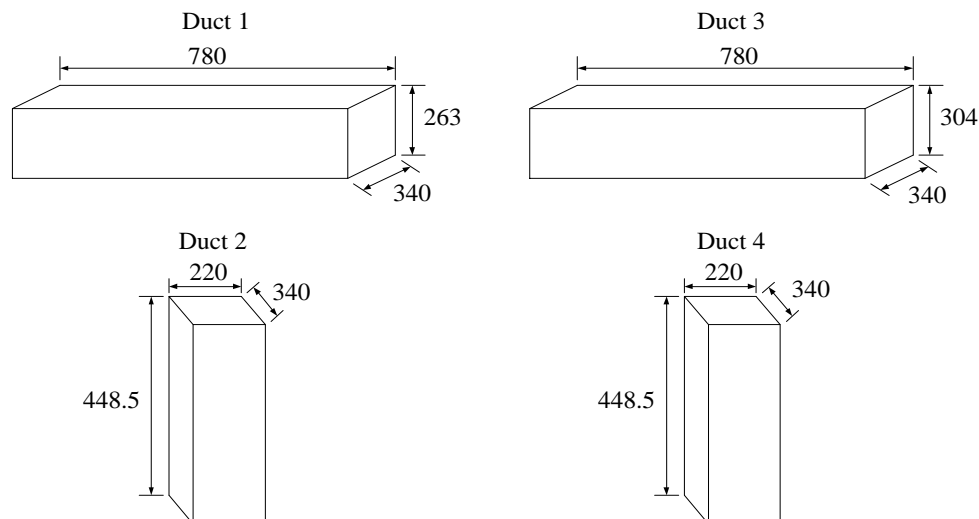
### Appendix C: Drier System Characteristics and Heat exchanger experimental setup

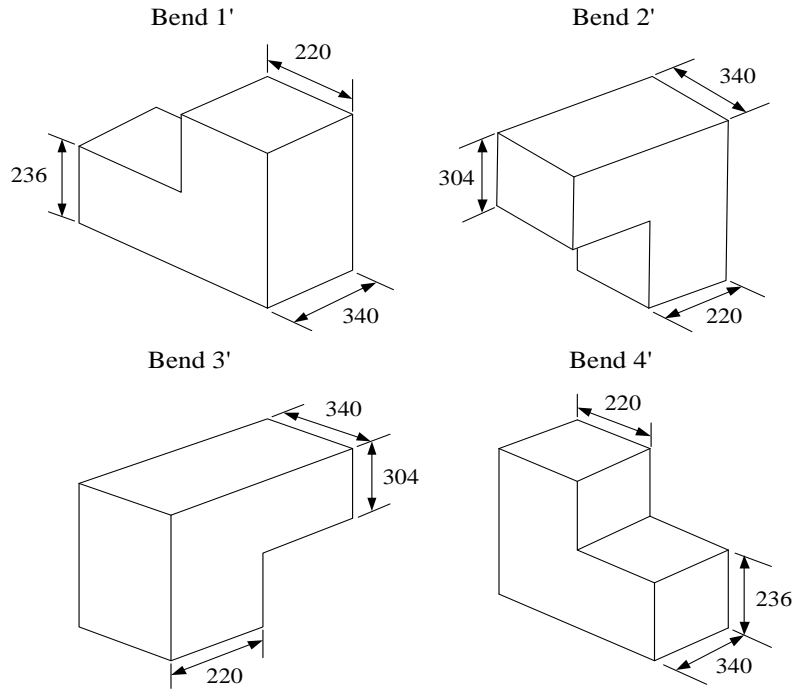
Mass transfer correlations to obtain the drying rate curves of the various materials were done using the test dryer at the University of Stellenbosch. The test drier was designed by Mafokeng and Dobson (2011). A schematic of the drier is shown in Figure 25.

The test drier can be modelled as having four ducts and four bends, as depicted in Figure 66. The figure also depicts where the ducts (unprimed) and bends (primed) are in the test dryer.



**Figure 59** Air flow and Various positions of ducts and bends in the test drier



**Figure 60** Duct dimensions (as positioned in figure 60)

**Figure 61** Bend dimensions

For non-circular ducts, the hydraulic diameter can be written as,

$$d_h = 1.3 \frac{(W \times H)^{0.625}}{(W + H)^{0.25}} \quad (\text{C.1})$$

the Reynolds number of the flow in the duct can then be found using equation 3.122

using Kroger (1998), the friction factor for flows at various Reynolds numbers can then be obtained

$$f = 64 / Re_d \quad \text{if } Re_d < 2000 \quad (\text{C.2})$$

$$f = 8 \left[ \left( \frac{8}{Re_d} \right)^{12} + \frac{1}{(a_1 + a_2)^{1.5}} \right]^{0.0833} \quad \text{if } 2000 < Re_d < 4000 \quad (\text{C.3})$$

$$f = 0.3086 \left[ \log_{10} \left\{ \frac{6.9}{Re_d} + \left( \frac{\varepsilon/d_h}{3.75} \right)^{1.11} \right\} \right]^{-2} \quad \text{if } Re_d > 4000 \quad (\text{C.4})$$

The bends were modelled using correlations given by Sauer et al. (2009). The following relations hold

$$C' = f \left( H_0/W_0, W_1/W_0 \right) \quad (\text{C.5})$$

and

$$K_{Re} = 3.5769 Re_d^{-0.106} \quad (\text{C.6})$$

The static pressure loss in the drier can then be given as a combination of the bend and duct losses



$$\Delta P = \left( f \frac{L_{duct}}{d_h} + C' K_{Re} \right) \frac{\rho V^2}{2} \quad (C.7)$$

The pressure loss can now be evaluated at different velocities and the various results are plotted in Figure 64.

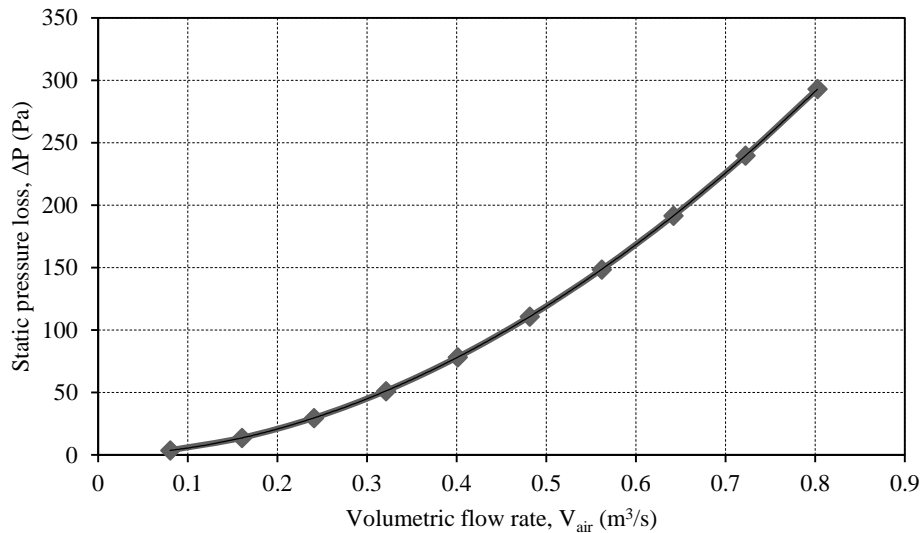


**Figure 62** Drier system characteristic curve

A characteristic curve is then fitted to the data points in Figure 64 and given as

$$\Delta P = 445.32V^{1.9032} \quad (C.8)$$

The windtunnel setup for the determination of the outside heat transfer coefficient is shown in figure 65

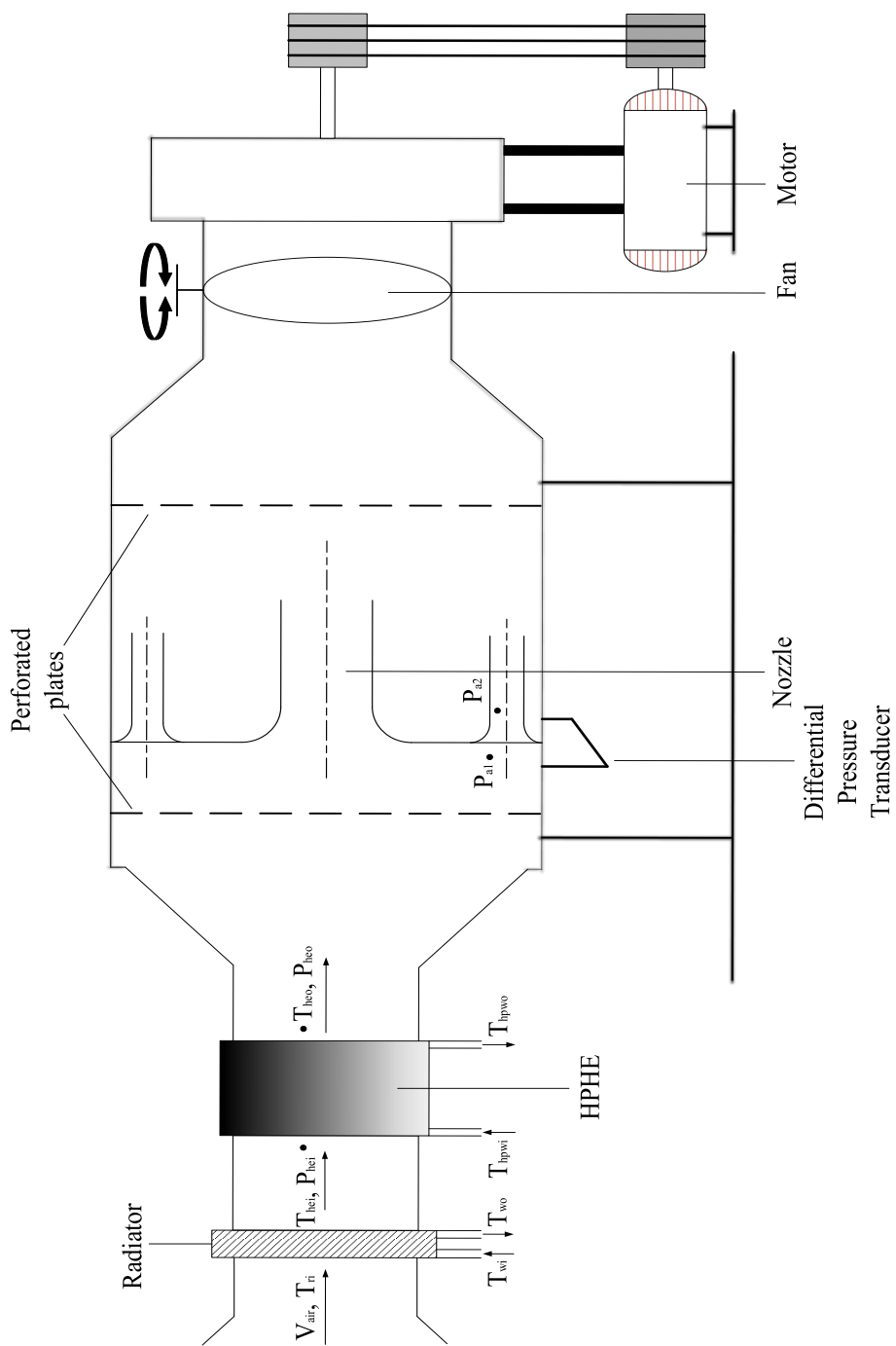


**Figure 63** Schematic of the wind tunnel setup for the determination of the outside heat transfer coefficients

The windtunnel setup for the separated-HPHRHE test is illustrated in figure 66.

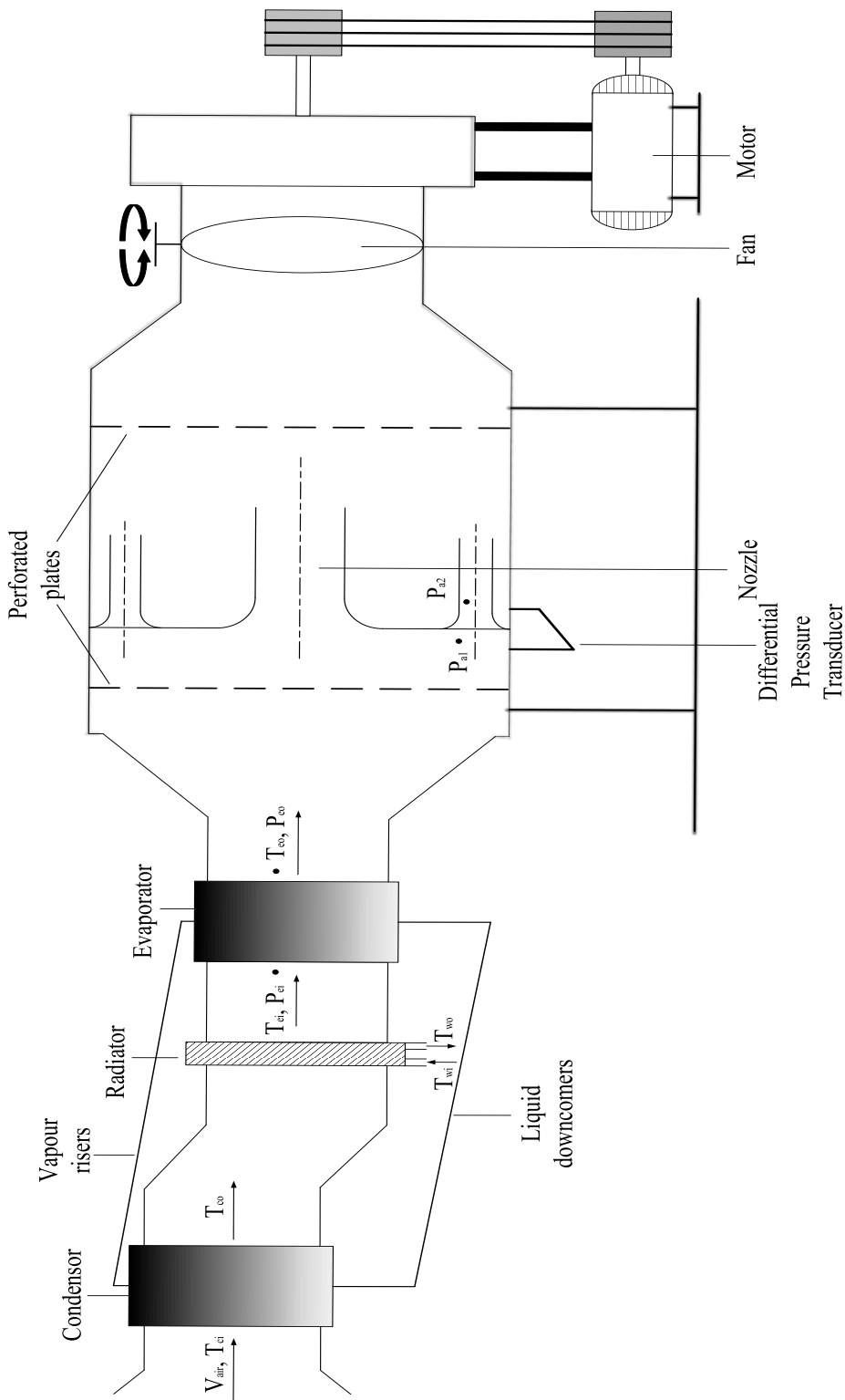
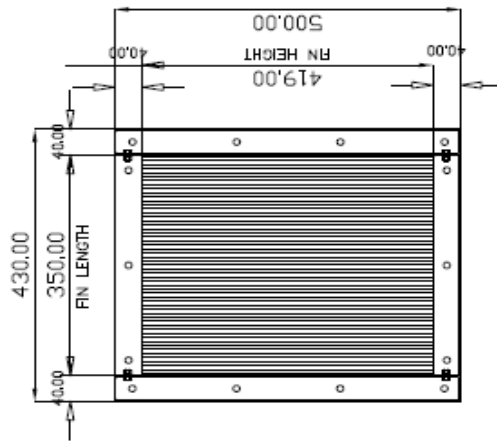


**Figure 64** Schematic of the wind tunnel setup for the determination of inside heat transfer coefficients

#### Appendix D: HPHE manufacturing details

The separated-HPHRHE consisted of two ColCab 5EN 1006-419 x 350 CU/AL/GALV Evaporator coils which were joined by  $\frac{3}{4}$  inch copper risers and  $\frac{5}{8}$  inch copper downcomers at the manifolds. The evaporator coils are shown in Figures 67 and 68



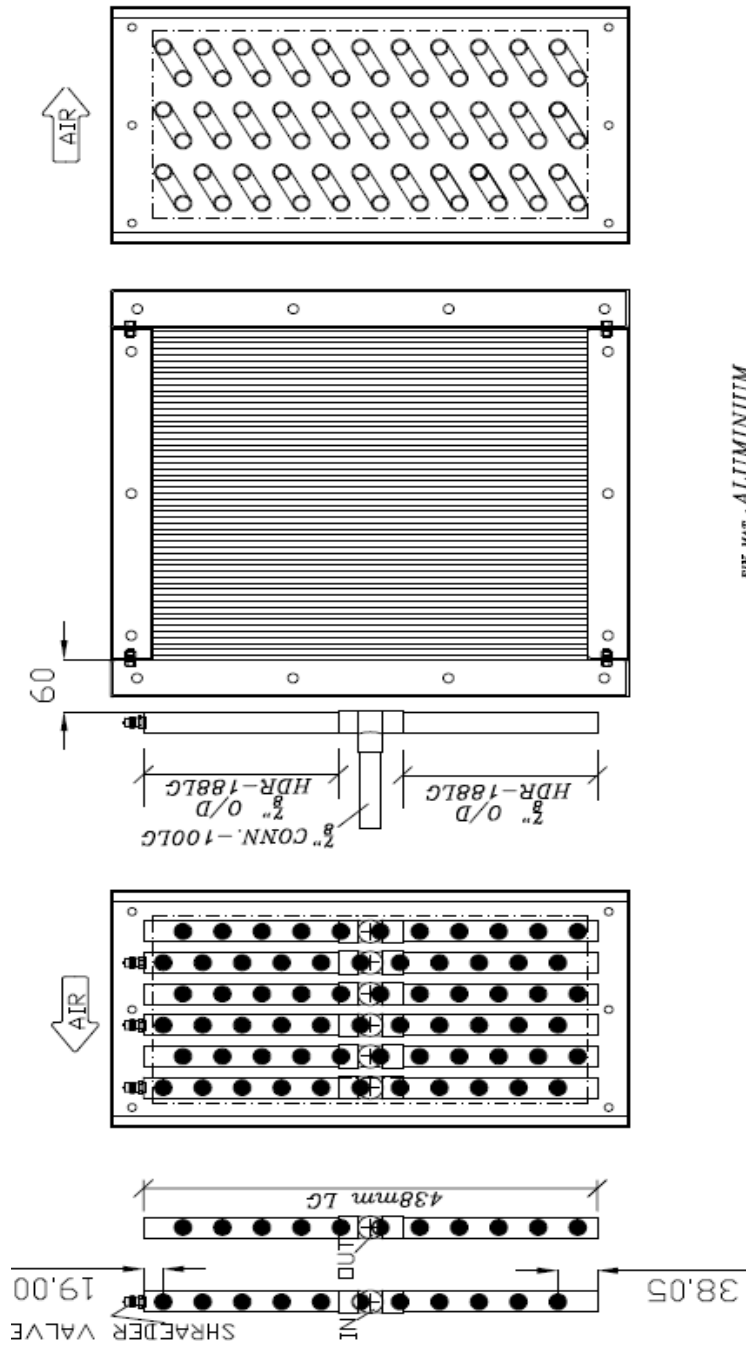
NOTES

- FIN LENGTH : 350mm
- FIN HEIGHT : 419mm(11-TUBES)
- FIN DEPTH : 198mm(6RD)
- FIN SPACING: 10FPI (2.54mm)

STELLENBOSCH UNIVERSITY

APPROVED BY	APP. DATE	REVISION	REV. BY	REV. DATE	REV. No.
DO NOT SCALE. IF IN DOUBT, PLEASE ASK. DIMENSIONS IN mm UNLESS OTHERWISE STATED			TITLE 5EN 1006-419 x 350		
<h1>COLCOIL</h1>			MATERIAL	CU/ALM/GALV	CODE
		SCALE	DRAWN BY : CLARENCE	DATE	20-11-2014
		SCALE_ON_PAPER	SHEET SHEET OF	DRWG NO	22751-02

Figure 65 Evaporator coil and flange design



FIN MAT : ALUMINIUM

CASING MAT : GALVANISE STEEL-40mm

QTY : 1-OFF

- 2 OFF - 15,88 odd X 0,39 CU. AC TUBE - 1148 mm LG
- 2 OFF - 15,88 odd X 0,39 CU. AC TUBE - 1097 mm LG
- 14 OFF - 15,88 odd X 0,39 CU. HAIRPINS - 1097 mm LG
- 2 OFF - 1 1/2" CU RETURN BENDS
- 14 OFF - 2 1/2" CU RETURN BENDS

SCALE:	N.T.S	PROJECT:	STUDENT PROJECT
DATE:	26/01/2015	DESCRIPTION:	5ACC 1006 - 419 x 350cu.abu.gatu. CONDENSER LH
DRAWN BY:	HAROLD	CLIENT:	STELLENBOSCH UNIVERSITY
CHECKED BY:		REF NO.:	PROJECT-CONDENSER
		JOB NO.:	22751-01
		DWG NO.:	166302



Figure 66 Evaporator coil manifold positions and dimensions

## Appendix E: Installation Cost analysis

While the separated-HPHRHE was not installed in an actual application, a theoretical cost study of the NibbliBits drier was undertaken to ascertain the potential savings of installing the HPHE used in this study. R134a was used in this instance because it is the cheapest and most common of the three refrigerants. It is assumed the heat exchanger will be cleaned once a year by on-site personnel and operated at the conditions stipulated in Appendix A1. The results are shown below.

**Table 9** HPHE savings potential

<b>Initial cost of separated-HPHRHE</b>	<b>Retrofit</b>	<b>New installation</b>
ColCab HPHE (2 off) [Rands]	9490	9490
15m $\frac{3}{4}$ -inch riser tubes @ R52/m	780	780
15m $\frac{5}{8}$ -inch riser tubes @ R45/m	680	680
Brazing, charging with R134a	2872	2872
Inlet/exhaust modifications to accommodate HE	4000	-
Schreader valves @ R15 each	180	180
Labour [R]	1500	1500
<b>Total initial costs [Rands]</b>	<b>19502</b>	<b>15502</b>
<b>Running costs/year</b>		
Maintenance [R]	2000	2000
<b>Total running costs [R]</b>	<b>2000</b>	<b>2000</b>
<b>Total Initial Cost</b>	<b>21502</b>	<b>17502</b>
Energy use without HPHRHE (Appendix A1) [kW]	36	36
Operating shifts	250	250
Hours per shift [h]	18	18
Energy usage per shift [kWh]	648	648
kWh reading per hour [kWh]	36	36
Energy cost [R/kWh]	0.15	0.15
<b>Total energy [R/year]</b>	<b>25650</b>	<b>25650</b>
Energy use with HPHRHE installed [kW]	27	27
Operating shifts	250	250
Hours per shift [h]	18	18
Energy usage per shift [kWh]	486	486

kWh reading per hour [kWh]	27	27
Energy cost [R/kWh]	0.15	0.15
Total energy [R/year]	18225	18225
HPHRHE Saving/Year – Running Costs [R/year]	5425	5425
Payback Period [Years]	3.96	3.22

## Appendix F: Drying Test results

The results for the drying characteristics of the sponge, potatoes and rusks are shown in Figure 67 to 69. The sponge dries the fastest as expected. The drying times decrease for increasing air flow rates and temperatures. However, at higher temperatures, the air flow rate has a less pronounced effect. Figure 68 shows the drying curves for the potatoes. As noted for the sponge, higher temperatures and air flow rates cause faster drying times. The effects of the temperature and air flow rate have a similar effect on the drying time throughout the range of experiments. The rusks were only dried at higher temperatures due to the very long drying time (>15 hours) at lower temperatures. It is observed that the difference in the air mass flow rate did not have a significant effect on the drying times.

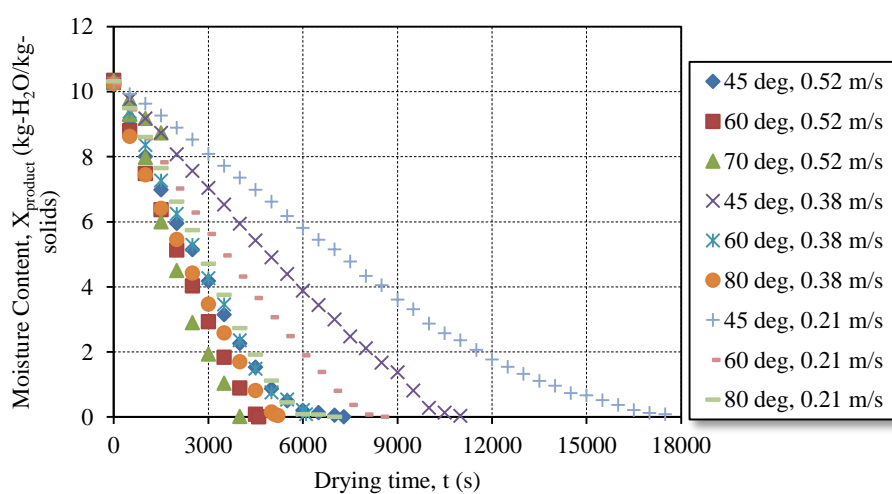


**Figure 67** Porous material (sponge) drying test results

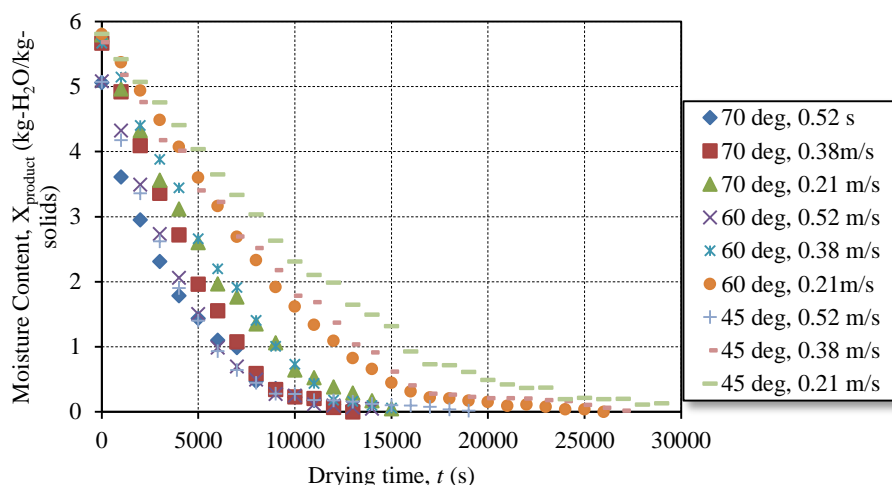


**Figure 68** Cellular material (potatoes) drying test results

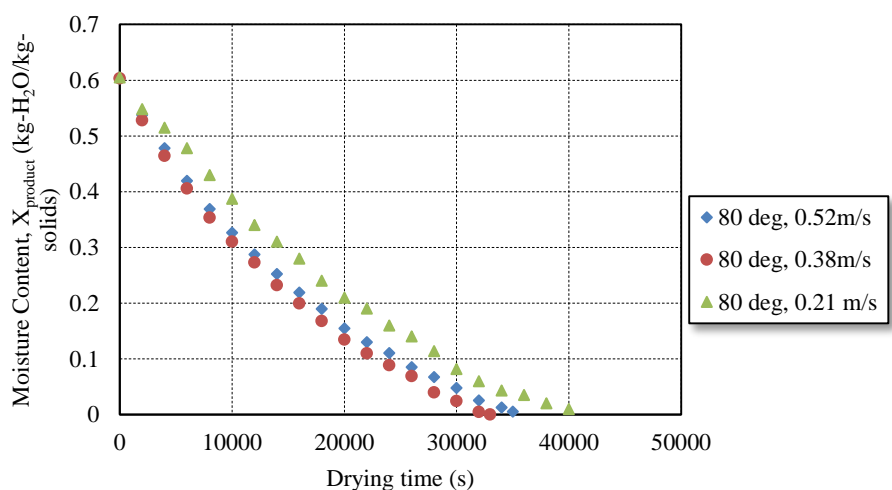


**Figure 69** Granular material (rusks) drying test results

Most manufacturers make materials of certain dimensions and thicknesses and thus in certain cases material thickness cannot be varied. Thus the influence of material composition, drying temperature and air speed at a relatively constant air humidity were investigated.

Three types of materials were considered for investigation of their drying characteristics: a porous-type of material (sponge), a cellular-type of material (potato) and a granular-type of material (rusks). The material mass was measured continuously and from this data drying curves were established for each material. For the sponge it was observed that at lower temperatures, the air speed over the material plays an important role in the drying rate. At higher temperatures, the air speed has less of a pronounced effect on the drying rate. This is expected when considering equations 3.117 and 3.118, the density decreases exponentially as the temperature rises so the  $h$ -value will increase at a slower rate the higher the temperature goes. As the temperature and velocity increase the larger  $h$ -value causes a larger driving force for heat transfer which in turn causes faster evaporation and because of the porous nature of the sponge (which provides little fluid flow resistance), the sponge will dry faster.



A similar trend continues for the drying of cellular materials. However, the temperature plays an equally important role as the air speed in this case. The main difference of the potato drying characteristic to that of the sponge is the much longer time required for the potatoes (consider 18000s against 30000s for similar conditions of 45 °C and 0.21 m/s). This is expected, since the cellular composition of the potatoes hinders water movement within the material as noted in Section 2.5. The rusks were not dried at low temperatures because of a test run that took in excess of 15 hours and as such drying at these low temperatures would not be feasible in a practical application. As indicated in Figure 69, the rusks drying time were not significantly influenced by wind speed, only slightly better drying times were obtained for faster air velocities. The drying times are even longer than for cellular materials. This is due to the fact that the rougher edges and irregular shaped grains of molecules cause an even higher flow resistance than the cells in the potatoes.

The form of the drying curve is also of interest. It is noted that the sponge essentially dries at a constant rate and only very close to bone dry conditions, the drying rate changes. This is expected since the conditions needed for constant rate drying, i.e. a surface supplied with an excess of moisture, can be easily maintained by the minor flow losses in the pores of the sponge. The potatoes exhibit the assumed constant-falling rate drying profile. It is also noted that the decrease is exponential in the falling rate section, as is predicted by the theory presented in Section 3.4. The rusks on the other hand exhibit only falling drying rate behaviour. This is attributed to the fact that the flow losses are so great in granular materials.